DAMAGE IDENTIFICATION IN BRIDGES COMBINING DEEP LEARNING AND COMPUTATIONAL MECHANICS

Ana Fdez-Navamuel del Olmo

Supervised by *David Pardo* and *David Garcia-Sanchez*

September 2022

eman ta zabal zazu

Universidad
del País Vasco

Euskal Herriko
Unibertsitatea

DAMAGE IDENTIFICATION IN BRIDGES COMBINING DEEP LEARNING AND COMPUTATIONAL MECHANICS

Ana Fdez-Navamuel del Olmo

Supervised by *David Pardo* and *David Garcia-Sanchez*

September 2022

This disseration has been possible thanks to the support received from: the European Union's Horizon 2020 research and innovation program under the grant agreement No 769373 (FORESEE project) and the Marie Sklodowska-Curie grant agreement No 777778 (MATHROCKS); the Base Funding - UIDB/04708/2020 of the CONSTRUCT - Instituto de I&D em Estruturas e Construções - funded by national funds through the FCT/MCTES (PIDDAC); the European Regional Development Fund (ERDF) through the Interreg V-A Spain-France-Andorra program POCTEFA 2014-2020 Project PIXIL (EFA362/19); the Spanish Ministry of Science and Innovation with references PID2019-108111RB-I00 (FEDER/AEI) and the "BCAM Severo Ochoa" accreditation of excellence (SEV-2017-0718); and the Basque Government through the BERC 2018-2021 program, the four Elkartek projects 3KIA (KK-2020/00049), EXPERTIA (KK-2021/00048), MATHEO (KK-2019-00085), and SIGZE (KK-2021/00095); the grant "Artificial Intelligence in BCAM number EXP. 2019/00432", and the Consolidated Research Group MATHMODE (IT1294-19) given by the Department of Education.

Acknowledgements

I would like to thank my supervisor David Pardo for appearing unexpectedly, for letting me into the world of mathematics and showing me that there is always a solution; for being always available and supportive; for his rigidity compensated by an enormous heart; for the long discussions trying to make me understand... but mostly, for his big contribution to make me enjoy and love what I do.

I would also like to acknowledge my co-supervisor, David Garcia, for bringing me the opportunity of doing the thesis, for his support, and especially for his positive mind at every moment.

I would like to thank Filipe Magalhães for kindly sharing his knowledge and time during my stays in Porto, and for the close collaboration till today, being a key piece to enrich the research of this thesis.

My workmates at Tecnalia also deserve mention for their support during these years. Especially Diego Zamora, for the long hours in front of the computer trying to find solutions, for his persistency, and also for the funny disconnection coffees; and Aratz Garcia, for guiding me in the first years when I most needed it. Another special mention to Fran Barroso, for his constant interest and encouragement, and our conversations about the weekend basket match.

I would like to mention my mates at BCAM and UPV/EHU (particularly Jon Ander Rivera and Carlos Uriarte that started at the same time and shared the dayly worries) for their help and support in the problems, and for the good moments in between. I am especially grateful to Javier Omella, for being always willing to help with patience and contagious passion. This mention is to be shared with his wife, Irene, since they became my host family in Bilbao.

I would like to acknowledge professor Javier Torres for showing me that we must always dare.

I would also like to express my gratitude to all the friends (the old and the new ones) that have accompanied me throughout these years, always with a word of support; and particularly to my basketball team, for being my scape road three

times per week.

Finally, I am very grateful to my family, especially parents and sisters (Henar and Eva), for their unconditional support and patience, and for being always ready to listen and encourage me to keep on.

Abstract

Civil infrastructures, such as bridges, are critical assets for society and the economy. Many of them have already reached their expected life and withstand loadings that exceed the design specifications. Besides, bridges suffer from various degradation mechanisms, including aging, corrosion, earthquakes, and, nowadays, the undeniable effect of climate change. This context has motivated an increasing interest in early detecting damage to prevent costly actions and dangerous failures. Structural Health Monitoring (SHM) consists of implementing effective strategies to continuously assess the health condition of structures using monitoring data collected by sensors.

This dissertation focuses on the SHM problem of damage detection and identification. It is an ill-posed inverse problem that aims at inferring the health state of a structure from measurements of its response. The measurements include large amounts of noisy data affected by environmental and operational conditions, acquired with sensors of different nature. Solving such a multidisciplinary problem encompasses the use of applied mathematics, computational mechanics, and data science. In this dissertation, we exploit the potential of Deep Neural Networks in approximating complex inverse problems and employ computational parametrizations and the Finite Element Method to enrich the training phase by including damage scenarios.

We explore two different approaches to the problem. In the first approach, we develop an outlier detection strategy to detect departures from the baseline condition. We only employ long-term monitoring data measured at the bridge during normal (healthy) operation. Starting from Principal Component Analysis (PCA) as a statistical data reconstruction technique, we design a specific Deep Autoencoder network that enhances PCA by adding residual connections to include nonlinear transformations. This architecture gains partial explainability by evaluating the contribution of nonlinearties over affine transformations in the reconstruction process. We also investigate the method performance when using local or global variables and evaluate the potential of combining both data sources in the damage detection task.

In the second approach, we reach a higher level of damage identification by estimating its severity and location. The goal is to provide a suitable methodology for real full-scale applications that requires reasonable computational resources. We employ a calibrated computational parametrization to solve multiple Finite

Element simulations under different damage scenarios. These synthetic scenarios enrich the training dataset of a Deep Neural Network that maps the response of the bridge with its health condition in terms of damage location and severity. Finally, we incorporate the effect of environmental and operational variability in the parametrization by applying a clustering algorithm to find representative samples among the entire dataset. We assume these samples cover most of the variability present in the data and consider them as starting points to generate synthetic training data.

We apply the proposed methods to three main case study bridges with available monitoring data: the Beltran bridge in Mexico, and the Infante Dom Henrique bridge in Porto, and the Z24 bridge in Switzerland. Both structures resulted critical to validate and test the ability of the proposed methods and to demonstrate their applicability in the full-scale.

Resumen

Las infraestructuras civiles, como los puentes, son bienes críticos para la sociedad y la economía actuales. Muchas de estas estructuras ha alcanzado ya su vida útil y actualmente se encuentra sometida a excesos de carga muy por encima de las especificaciones de diseño. Además de esta sobrecarga, los puentes se ven expuestos a diversos mecanismos de degradación, como el envejecimiento de materiales y componentes, la corrosión, la ocurrencia de terremotos y, hoy en día, un fenómeno tan innegable como es el cambio climático. La monitorización de la salud estructural (SHM) consiste en implementar estrategias efectivas para evaluar de manera continua la condición de salud de las estructuras mediante datos procedentes de la monitorización.

Esta tesis aborda el problema de SHM de identificación y detección de daño estructural. Se trata de un problema inverso que pretende inferir el estado de salud de la estructura a partir de la medición de ciertas variables respuesta. Las mediciones incluyen grandes cantidades de datos ruidosos, afectados también por las condiciones operativas y ambientales en que trabaja la estructura, y se miden a través de sensores de diferente tipo implantados en la estructura (acelerómetros, galgas extensiométricas, termómetros, etc.). Resolver un problema multidisciplinar como este requiere la aplicación de matemáticas, mecánica computacional, y ciencia de datos. En esta tesis, explotamos el potencial de las técnicas de Deep Learning (DL), particularmente las redes neuronales profundas, para aproximar problemas inversos complejos. Además, empleamos modelos computacionales y el método de Elementos Finitos (FE) para simular escenarios de daño y enriquecer la fase de entrenamiento de las redes neuronales y lograr diagnósticos más detallados.

Exploramos dos enfoques diferentes al problema de identifiación de daño. En el primer método, desarrollamos una estrategia de detección de anomalías capaz de detectar salidas de una condición asumida como referencia o base. Empleamos datos procedentes de monitorización a largo plazo medidos en el estado normal de funcionamiento de la estructura. Partiendo de la técnica de Análisis de Componentes Principales (PCA) como herramienta estadística de compresión y reconstrucción de datos, diseñamos una red neuronal profunda conocida como autoencoder residual capaz de mejorar los resultados del PCA mediante la incorporación de transformaciones no lineales en las conexiones residuales. Esta arquitectura proprociona una explicabilidad parcial al método, ya que permite evaluar la contribución de las no linealidades sobre las transformaciones lineales en el proceso de reconstrucción. También investigamos el funcionamiento del método para distintas variables de entrada. Comparamos la capacidad de detección cuando se usan (a) solo variables locales, (b) solo variables globales, y (c) la combinación de ambas.

En el segundo enfoque, buscamos alcanzar un nivel más alto en la identificación de daño mediante la estimación de su severidad y localización. El objetivo es proporcionar una metodología adecuada para aplicaciones a escala completa que requiera una cantidad asumible de recursos computacionales. Empleamos una parametrización computacional calibrada para representar la estructura real y generar múltiples simulaciones FE en diferentes estados de daño clasificados por localización y severidad del daño. Estos escenarios sintéticos se emplean para enriquecer los datos de entrenamiento de una red neuronal profunda que establece la relación entre la respuesta estructural medida a través de las propiedades dinámicas (frecuencias y modos de vibración) y la condición de salud estructural en forma de localización y severidad del daño. Finalmente, incorporamos el efecto de la variación ambiental y operativa en la base de datos sintética aplicando un algoritmo de agrupación de datos que identifica mediciones representativas. A partir de estas mediciones, se realiza el proceso de calibración de la parametrización FE y se generan escenarios de daño sintético. Asumimos que estas muestras representativas cubren la mayor parte de la variabilidad presente en los datos y por tanto permiten generalizar mejor los diagnósticos.

Los métodos propuestos se aplican principlamente a datos procedentes de tres casos de estudio reales: el puente Beltrán en Méjico, el puente Infante Dom Henrique en Oporto, y el puente Z24 en Suiza. Estos datos han sido críticos para poder desarrollar y validar la capacidad de funcionamiento de los métodos desarrollados en esta tesis, así como para demostrar su aplicabilidad en casos a escala real.

Contents

Acronyms

SHM	Structural Health Monitoring
PCA	Principal Component Analysis
EOCs	Environmental and Operational Conditions
OMA	Operational Modal Analysis
ML	Machine Learning
DL	Deep Learning
NNs	Neural Networks
DNNs	Deep Neural Networks
CNNs	Convolutional Neural Networks
RNNs	Residual Neural Networks
FE	Finite Element
FEMU	Finite Element Model Updating
ROC	Receiver Operating Curves
FPR	False Positive Rate
TPR	True Positive Rate
SD	Standard Deviation

List of Figures

List of Tables

1 Introduction

1.1 Motivation

Civil infrastructures are critical assets for society and economy. Bridges suffer from various degradation mechanisms, including aging, material deterioration, or extreme loads [27, 48]. Another hazard that currently threatens bridges is climate change [58]: temperatures suffer fast and extreme variations; floodings, earthquakes, and tsunamis occur more often, and the water level is increasing in many parts of the world. This situation has turned bridges into vulnerable assets and imposes priority on ensuring their integrity and safe performance.

One key challenge in this context is the early identification of damage [50]. Visual inspections are the first attempt to evaluate the state of structures, but they provide subjective diagnostics [22]. These practices are laborious, time-consuming, risky, and their implementation often requires service shutdown [8, 92]. Besides, they detect only eye-accessible defects, such as cracks or spalling. The inefficacy and limitations of visual inspections have promoted the emergence of Structural Health Monitoring (SHM) [92]. SHM aims at solving the inverse problem of damage identification by measuring the response of the structure through instrumentation devices. The application of SHM practices contributes to detecting damages at an early stage, allowing to timely take corrective actions and prevent catastrophic failures [22]. This enables transit from traditional pre-scheduled maintenance plans to condition-adaptive strategies, which are more efficient in both economic and safety terms.

In recent decades, several civil engineering structures have been instrumented for long periods with health assessment interests [83, 103, 29, 23, 91, 71, 39, 86]. There has also been a huge effort in developing SHM techniques using non-destructive testing practices [75], computer vision [38], or Artificial Intelligence methods [131]. Despite the improvements accomplished, SHM is still far from being a consolidated practice in the real world, with most works applied to lab-scale pilots or parameterized models under controlled environments. Various challenges prevent its robust implementation in full-scale operating systems, including the uniqueness of each civil engineering structure, the uncertain and varying operational environment, the lack of empirical data regarding damage scenarios, and the costly adaptation to large complex structural systems.

The vulnerability of currently operating civil infrastructures expresses the need for reliable and effective SHM practices that overcome the existing challenges. The recent technological advances in instrumentation, computation, and data science, settle an unprecedented context for active research in the field. These circumstances motivate the present thesis, which intends to contribute to developing and applying novel SHM practices to in-service structures.

1.2 Related work and literature review

1.2.1 Damage Identification and SHM

Let us denote the bridge response by $\mathbf{u}_B$. At its simplest level, a bridge behaves as a simply supported beam with additional boundary conditions, governed by the following partial differential equation:

$$W\frac{\partial^2\mathbf{u}_B(x,t)}{\partial t^2} + C\frac{\partial \mathbf{u}_B(x,t)}{\partial t} + K\mathbf{u}_B(x,t) = \mathbf{q}(x,t), \tag{1.1}$$

where W, C, and K are the inner properties of the structure and stand for its mass, damping, and stiffness, respectively. The external load is represented by $\mathbf{q}(x,t)$, and variables x and t indicate position and time. For simplicity in notation, from now on we ommit the location and time depedence, (x,t).

According to [41], damage can be defined as any change to the physical properties of a system that results in an adverse performance of that system. Damage mainly affects the stiffness properties (K), causing a rigidity reduction that reflects on the bridge response, $\mathbf{u}_B$. Let $\mathcal{F}$ be the forward operator that relates the bridge response $\mathbf{u}_B$ with its properties and conditions:

$$\mathbf{u}_B = \mathcal{F}(W, C, K, BCs, \mathbf{q}), \tag{1.2}$$

In practice, we obtain the response $\mathbf{u}_B$ through monitoring campaigns $\mathcal{M}$ that provide measured observations $\mathbf{m} = \mathbf{u}_B + \boldsymbol{\epsilon}$, where $\boldsymbol{\epsilon}$ contains the measurement error. We denote $\mathcal{G}$ to the operator that yields the damage state D_B as:

$$D_B = \mathcal{G}(W, C, K, BCs, \mathbf{q}). \tag{1.3}$$

The true value of the properties affected by damage is unknown and unmeasurable. Thus, solving Equation 1.3 becomes unfeasible. It turns damage identification into an inverse problem, where we intend to infer the condition D_B of a structure using measurable observations $\mathbf{m}$ of its response [50]. Figure 1.1 illustrates the problem in a block diagram. The red-colored arrow denotes the inverse operation ($\mathcal{I}$) of damage identification.

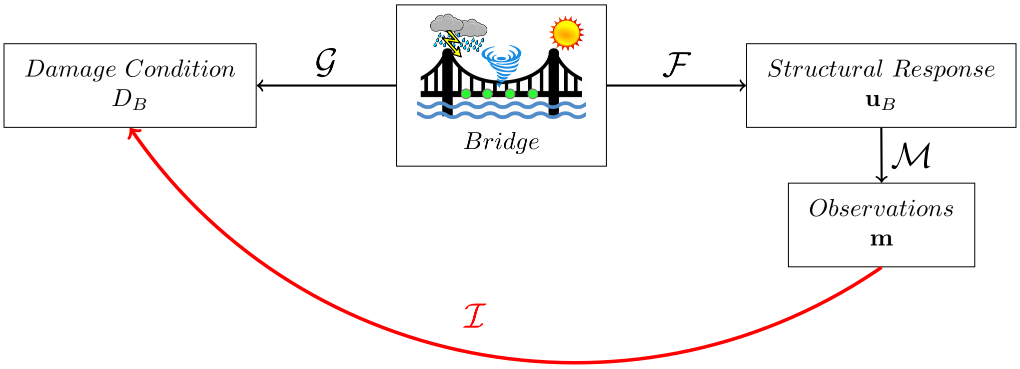

Figure 1.1: The inverse problem of damage identification as a block diagram

According to Rytter [114], the identification of damage (i.e., the information included in D_B) has various levels in terms of the depth of the attained knowledge. These levels are:

- Level I: detection (qualitative notification of the presence of damage)
- Level II: localization (estimate the probable location)
- Level III: quantification (estimate the severity of the damage)
- Level IV: prognosis (consequences of the given damage)

Achieving each level depends on the data availability and the complexity of the SHM approach [41]. There are four main steps in the implementation of an SHM strategy, namely, (i) operational evaluation, (ii) data acquisition and cleansing, (iii) feature extraction, and (iv) statistical model development [41]. This dissertation focuses on step (iv), although it includes aspects related to the others.

1.2.2 Measurements in SHM

In large civil engineering structures, raw monitoring data may come from very different sensor types and contain numerous sources of uncertainty. Deciding what to measure is critical when implementing SHM for damage identification. The measured observations $\mathbf{m} = \mathbf{u}_B + \boldsymbol{\epsilon}$ must be sensitive to the presence of damage for the SHM strategy to be effective. In operating bridges, many phenomena exist that make the structural response fluctuate over time regardless of the health condition. These are Environmental and Operational Conditions

(EOCs), including temperature, humidity, or traffic level. The bridge response contains two affecting terms, i.e., $\mathbf{u}_B = f(\mathbf{u}_{Dam}, \mathbf{u}_{EOC})$, where $\mathbf{u}_{Dam}$ accounts for the effect of damage and $\mathbf{u}_{EOC}$ refers to the effect of varying EOCs. The ideal measurement would be highly sensitive to damage but poorly affected by EOCs.

Vibration-based SHM is a widely extended practice that employs the dynamic response of the structure as the damage-sensitive feature [9, 80, 5]. In this context, raw vibration measurements (e.g., acceleration signals) are often processed through Operational Modal Analysis (OMA) [20] techniques to produce the modal properties of the structure, mainly eigenfrequencies and eigenmodes [92]. Avci et al. [12] reviewed the extensive literature on different data-driven approaches to detect structural damage using vibration monitoring data.

While post-processing measurements to estimate eigenfrequencies is well established (see e.g., [67, 139, 135, 21]), approximating eigenmodes (a.k.a., mode shapes) presents additional difficulties. Only a few OMA techniques address this challenge [88, 67], yet the accuracy of higher-order modes can be deficient. For this reason, some vibration-based approaches employ only eigenfrequencies as damage-sensitive features. For example, Comanducci et al. [31] investigate various data-driven algorithms (dynamic regression, linear and local PCA, and cointegration). They use time histories of eigenfrequencies measured in the Infante Dom Henrique bridge. Magalhães et al. [87] also employed Infante Dom Henrique as the target structure to investigate the potential of eigenfrequencies in damage detection. However, eigenfrequencies are global variables, and their ability to provide information regarding damage location is limited [126]. It implies that they yield only a level I diagnostic in the Rytter scale [114].

Recent developments in sensing technology and computational resources have aroused a growing interest in exploiting raw time-domain measurements [131]. These include vibration (acceleration) signals and quasi-static changing responses, such as displacements, rotations, or strains. [22]. These signals have demonstrated detection capabilities, mainly when damage occurs nearby the sensor emplacement (local variables). For example, Teng et al. [132] applies one-dimensional CNNs to raw short-term acceleration signals. They validate the method in a laboratory environment using a truss bridge and a frame structure. Azim and Gül [13] employed strain measurements to detect damages in truss railway bridges. They validated the method using a Finite Element (FE) model to simulate stiffness reductions, achieving successful detection, location, and relative quantification of damage.

But local variables lose sensitivity when the damage occurs far from their location. This fact restricts the detectable damages to the instrumented region, and very dense sensor arrays are required to cover the whole structural system. In this sense, including global variables (eigenfrequencies) seems promising to solve the detection problem. Only the work presented by Alten et al.[4] was found to study the detection ability of eigenfrequencies, strains, and rotations separately in a post-tensioned reinforced concrete bridge. Combining both data sources (i.e., local and global) in full-scale bridges remains unexplored in the existing literature and arises one of the contributions of this thesis.

1.2.3 Model-based damage identification

There are two broad approaches to solve the damage identification problem: model-based and data-driven. Model-based approaches account for the physics that govern the structural behavior [50]. These techniques require strong physical knowledge and modeling skills [12]. Model-based methods estimate the structural properties of a numerical approximation to minimize the discrepancy between its response and that of the real structure [130]. This technique has been extensively applied in the civil engineering field and is broadly known as Finite Element Model Updating (FEMU) [51].

There are two main scopes of FEMU in SHM: calibration, and damage identification. Calibration is the process of updating the values of the structural properties to attain a reliable baseline parametrization. The goal is to reduce uncertainties and unknowns in the model given some experimental input. Hence, the variation interval within this approach is small. Some cases of FEMU for calibration can be found in [30, 112, 117]. For example, [112] solves a calibration problem by updating the parameters of a bowstring-arch railway bridge using a genetic algorithm. They feed the updating process with the response obtained during an ambient vibration test (eigenfrequencies, eigenmodes and damping coefficients).

On the other hand, FEMU can also be applied to evaluate an unknown bridge condition and identify damage by enforcing the model to reproduce a measured response. In this diagnostic phase, since the real damage condition is unknown, a much wider interval of variation is assumed for the parameters, yielding to computationally expensive procedures [61]. Some authors, such as Liu et al. [82] and Tran-Ngoc et al. [136], apply FEMU for damage identification in full-scale structural systems. Work [6] employs a genetic algorithm-based FEMU to a railway bridge with successful location and quantification of damage.

The main limitation of model-based approaches is the huge computational effort required to provide a diagnostic. FEMU can be very time-consuming when a large number of parameters with a wide variation interval is involved [89]. This often prevents its application as a real-time assessment method.

1.2.4 Data-driven damage identification

As opposed to model-based, data-driven methods rely exclusively on measurements [119]. The core idea is to characterize the reference behavior of the structure by measuring some features of its response during long-term operation [37, 40]. Traditional data-driven methods employ statistical pattern recognition [63] and control charts of directly measured variables [76].

1.2.4.1 Data compression techniques

As previously introduced, any measurement contains three main terms:

$$\mathbf{m} = \mathbf{u}_{Dam} + \mathbf{u}_{EOC} + \boldsymbol{\epsilon} \tag{1.4}$$

One of the most challenging issues in data-driven SHM is tackling the effect of environmental and operational variability introduced by $\mathbf{u}_{EOC}$ [111, 107, 125, 8]. These phenomena affect the system and may conceal the damage detection ability of the algorithms [128, 92]. Numerous statistical methods have been developed to address this problem, such as autoregressive models [12] or Principal Component Analysis (PCA) [102, 32, 31, 92].

PCA is an statistical data compression tool widely employed in SHM [134, 16, 129, 53]. It applies a linear transformation of the data into the orthogonal subspace formed by the most relevant eigenvectors of the data covariance matrix [104]. This method allows isolating environmental and operational variability by projecting the data onto the most relevant principal components (eigenvectors) [94]. There exist numerous applications of PCA in damage detection [31, 129, 53, 54]. For example, Mujica et al. [94] use the residual between a sample and its corresponding projection onto the model of principal components as a novelty indicator for structural condition assessment. In our work [53], we propose an outlier detection method to assess the behavior against horizontal loads of a bridge in Mexico. The goal is to detect malfunctions in the sliding bearings that allow the relative displacement between the deck and the piers. We apply PCA to compress monitoring data from four longitudinal displacement sensors and calculate a single-value damage indicator for outlier detection. Analogously, work [13] proposes a PCA-based damage detection strategy for truss railway bridges using strain time-history responses. They validate the method numerically using an analytical model with induced aritifical damage.

Since PCA performs data compression via a linear mapping, it may lose important (irrecoverable) information [115]. Some nonlinear approaches have emerged to overcome this problem, such as Kernel PCA [95, 56]. But adequately selecting the nonlinear function for Kernel PCA is often a challenging task that may prevent obtaining successful results.

1.2.4.2 Machine Learning techniques

With the irruption of Artificial Intelligence, more complex data-driven techniques have emerged, where an important branch is Machine Learning (ML) [116]. Neural Networks (NNs) are the most common form of Machine Learning technique [25]. Compared to traditional data-driven approaches, NNs have the potential to effectively approximate complex nonlinear functions. According to the universal approximation theorem, a single-layered network can approximate any function when enough hidden units are available [70]. But employing a single layer may be a suboptimal way of addressing highly complex problems. During decades, there has been a huge evolution in the configuration and training of Deep Learning (DL) methods, particularly Deep Neural Networks (DNNs) [59, 64].

DNNs have demonstrated to be powerful techniques in SHM applications [14, 34, 124, 127, 46, 132, 142, 93]. Some works, such as [131, 14, 116], provide insightful reviews on the evolution of Artificial Intelligence based methods in the field of SHM. In this context, the goal of the DNN is to approximate the mathematical relationship between the response of the structure and its health condition, represented by function $\mathcal{I}$ in Figure 1.1. We often refer to this approximation as $\mathcal{I}_{\boldsymbol{\theta}}$, where $\boldsymbol{\theta}$ include all the involved parameters of the DNN. Since DNNs undergo a training phase to learn this function, the computational effort concentrates during training, yielding practically real-time predictions [14]. This is an important advantage over model updating techniques. For example, Mehrjoo et al. [90] propose a feedforward NN-based SHM method for damage detection in truss bridge structures. The NN estimates damage severity at the joints using eigenfrequencies and eigenmodes as input data.

CNNs are very poweful due to their ability to extract high-level representations features from data [116]. They have been extensively applied in image processing problems such object classification and recently progressed in the field of SHM. For example, work [15] employs a CNN trained with acceleration time histories and compressed histograms to detect and localize damage in large scale structures. Abdeljaber et al. [2] employ one-dimensional Convolutional Neural Networks (CNN) to detect and locate damage at the different joints of a steel frame in a laboratory environment. An independent CNN is designed and trained for each of the joints. Other works, such as [140] or [143], employ CNNs to find out cracks from images of the target structure.

Autoencoders

Autoencoders are a specific Deep Neural Network type based on the same idea of data compression as PCA but including nonlinearities [115]. An autoencoder reconstructs the input data by following two steps: encoding and decoding [17].

The encoding step compresses the data onto a lower-dimensional representation (dimensionality reduction), and the decoding step reconstructs the original measurements from the lower-dimensional features [68]. During training, the autoencoder learns to reconstruct data from the healthy condition of the structure, which includes environmental and operational variability [124]. The reconstruction error measures the discrepancy between a measurement and its reconstruction. When we obtain new measurements that belong to a similar (undamaged) condition, we expect the autoencoder will adequately reconstruct them with a small error value. It is assumed that the variability induced by damage affects the data differently than environmental and operational phenomena [111]. Thus, we expect that the autoencoder yields a high reconstruction error with the appearance of damage that sufficiently affects the measurements [26, 96].

Recently, autoencoders have been employed for outlier detection in several areas [49]. Several works exist in the literature employing reconstruction error in SHM applications [49, 28, 96, 7]. For example, Chen et al. [28] apply autoencoder ensembles for outlier detection to various benchmark datasets and compare its effectiveness to other traditional techniques. Oh et al. [97] employ an autoencoder network to detect abnormal operation sounds of a complex machine using audio spectrograms. Li et al. [79] propose a hybrid autoencoder for anomaly detection in meteorological measurements to handle spatio-temporal data. All these works employ basic autoencoder architectures and dismiss the transition process to outperform linear data compression approaches.

1.2.5 Combined model and data-based damage identification

One clear advantage of data-driven approaches over model-based is their ability to provide almost real-time diagnostics once trained. Besides, they skip the need to create accurate FE models. But the main challenge for their implementation in the civil engineering field is the lack of real experimental data regarding possible damage scenarios. This restricts their application to unsupervised learning alert systems that detect departures from the pre-characterized healthy condition [37]. Achieving more insightful diagnostics requires the incorporation of synthetic damage scenarios from FE simulations. This enlarges the learning domain of data-driven algorithms and allows to reach levels II and III of damage identification (location and quantificaition) in Rytter scale [114].

Some hybrid approaches that incorporate numerical simulations as an additional source of information have been recently investigated [100, 45, 93, 144, 121, 120]. Figueredo et al. [45] address an unsupervised learning problem by feeding the data-driven algorithm with synthetic data from healthy conditions under different simulated environments. In the supervised field, Pathirage et al. [100] apply autoencoders to identify damage in a small-scale frame structure.

They employ the stiffness reductions caused by damage at each element of the system directly as the output variables to be predicted. Zhang et al. [144] propose a physics-guided neural network approach to localize damage in structures. They design a loss function that accounts for the discrepancy between the prediction given by the data-driven algorithm and the result of model updating to enhance the diagnostic. Mousavi et al. [93] propose a hybrid technique to detect damage in a laboratory beam structure using a Deep CNNs. They train the NN using frequency data from the healthy experimental response and numerical simulations to include damaged scenarios. Authors use the undamaged response to update the parameters of the numerical model before running damage simulations. Seventekidis et al. [122] also employ a CNN classifier to detect structural damage in an experimental benchmark beam. The training phase includes simulated responses from a computational model that is initially updated for the healthy state, including different load conditions and damaged states. Analogously, in [120], authors propose a CNN-based classification approach to identify damage in a pin-joint composite truss structure using synthetic data from FE models. Despite the successful results obtained within these works, all of them remain in a laboratory implementation and their practicality on the full scale has not been demonstrated yet.

1.3 Contributions of the Dissertation

This dissertation intends to contribute to the transition from research to the real practice of SHM damage detection methods for full-scale operating bridge structures. We address the implementation of Deep Learning techniques from a mathematical understanding found in traditional data compression techniques such as PCA to provide comprehensible solutions. We contribute to this applicability through various developments, some of them already included in recent publications [53, 43, 44].

In work [53], we provide an unsupervised SHM approach based on PCA to monitor the global behavior of the sliding bearings in the Beltran viaduct, in Mexico. We first demonstrate the existence of strong linear correlations in the relative displacements measured at the deck-pier connections of the bridge during nine months of monitoring. We then employ linear PCA to compress the measurements and design a robust performance indicator for outlier detection that is only weakly affected by temperature variations. This work delivers a fully applicable SHM practice for operating bridges that satisfy the assumption of linearly correlated measurements.

Work [43] proposes a DL-based enhancement of PCA for outlier detection to assess the structural condition of two operating bridges. We investigate the limitations of linear PCA by first replicating its compression and reconstruction ability with an autoencoder NN architecture. We then incorporate deep residual connections to account for nonlinear relationships in a partialy explainable way. By fixing the weights obtained after training the linear autoencoder, we realize the enhancement provided by including nonlinear relationships. The blockwise configuration of the autoencoder enables the activation or deactivation of the residual connections. This work provides an enhanced outlier detection methodology for full-scale bridges that adapts to both linear and nonlinear variability environments.

We provide a comparative study regarding the use of global and local monitoring variables, as well as their combination. We apply the deep residual autoencoder architecture developed in [43] to long-term monitoring data including (a) global variables (eigenfrequencies), (b) local variables (inclinations and strains), and (c) the combination of both. We first investigate the contribution of each variable type in the detection of damage, demonstrating that combining both sources of data contributes to extend the detectable damage locations and reduce the minimium sensitivity level. We subsequently analyze the potential of local variables to determine the location of damage when it occurs nearby a particular sensor emplacement. This work reveals the benefits of deploying complementary monitoring systems to achieve robust and insightful damage detection assessment for large bridge structures under service.

Work [44] addresses the inverse problem of damage identification throughout a supervised learning approach. We overcome the lack of real damage scenarios using FE simulations that recreate stiffness reductions at different bridge parts and obtain the dynamic response in the form of eigenfrequencies and eigenmodes. Computational mechanics provide the basis to understand and simulate the behavior of the bridge structures. We define the relationship between the FE parametrized damage and two identification labels: location and severity. We then train a DNN that maps the dynamic response of the bridge to its health condition according to the damage description labels. This work provides a higher level diagnostic compared to the unsupervised approaches addresed in [53, 43] since it estimates the location and severity level of the damage.

Finally, we also explore the challenging task of including the effect of varying environmental and operational conditions in the combined methodology proposed in [44]. This last research provides a novel methodology based on Gaussian Mixture models to classify experimental data and select significant points to build the synthetic database for training.

1.4 Outline of the thesis

The remainder of this thesis is structured as follows: Chapter 2 addresses the development of the deep enhanced PCA technique proposed in [43] and its application to two full-scale operating bridges. It includes the analysis of combining local and global variables to improve the diagnostic. Chapter 3 is devoted to the implementation of the supervised learning damage identification method developed in [44]. Chapter 4 addresses the challenge of accounting for varying EOCs in the synthetic database of the combined model-based and data-driven approach. Chapter 5 summarizes the main conclusions and remaining challenges to be addressed as future research. Finally, Chapter 6 includes the main achievements of this dissertation including the scientific contributions, the published works in journals, and the conferences and workshops developed within the framework of the thesis.

2 Deep Learning enhanced PCA

2.1 Introduction

This chapter addresses the problem of damage detection in bridge structures using an unsupervised learning approach. As introduced in Chapter 1, one of the key challenges of this approach is the effect of changing EOCs on the monitoring data.

PCA is one of the most extensively employed practices to tackle this issue, since it only requires long-term monitoring data from the bridge response [134, 16, 60]. The main limitation of PCA is that it performs well in linearly correlated (and weakly nonlinear) spaces but worsens with more complex relationships. In the field of civil engineering, monitoring data may come from very different types of sensors affected by several phenomena, yielding a highly nonlinear data space. This restricts the use of PCA for our particular purpose.

With an autoencoder NN, we can easily overcome the limitation of PCA since it incorporates nonlinear transformations. However, the standard autoencoder architecture lacks explainability in terms of separating the contribution of nonlinear operations over simple linear transformations. We develop a particular autoencoder architecture that uses residual connections to obtain a partially explainable NN [10]. Explainability is a key advantage of our proposed architecture as it enables to work with simple linear transformations when possible and incorporate nonlinearities if required. Imposing specific constraints during training, we can also attain specific solutions such as PCA in the linear approach. The architecture also allows understanding the enhancement process with respect to traditional PCA.

We apply the designed residual autoencoder to assess the structural behavior of operating bridges. While most bridge SHM works focus on the dynamic properties and acceleration signals [87, 31, 106, 24, 81, 42], here we exploit other measurable time series from long-term monitoring campaigns. The input variables are measurements from different sensors and constitute the target output to be predicted by the autoencoder. We use the reconstruction error as a single-value novelty indicator for outlier detection. We apply this methodology to two real structures under service. The first one employs the same dataset as Garcia-Sanchez et al. [53] for the Beltran bridge in Mexico. The second case study includes multivariate sensor data from a continuous monitoring campaign of five years of service life of bridge Infante Dom Henrique in Porto, Portugal.

2.2 Principal Component Analysis (PCA)

PCA is one of the most widely used data compression techniques for outlier detection [60]. Its main application in SHM is removing the effect of environmental and operational variability. As opposed to other techniques (e.g., autoregressive models), PCA avoids measuring environmental/operational variables since they are considered embedded variables [141].

PCA applies an affine transformation to project the original multivariate dataset into a lower-dimensional vector subspace defined by the directions that contain most of the variance present in the data [137]. Let $M \in \mathbb{M}^{n \times v}$ be a set of n rescaled measurements from v variables (sensors). We express the compression into a k-dimensional space as a linear mapping:

$$Z = TM, \tag{2.1}$$

where matrix $T \in \mathbb{R}^{k \times v}$ is the transformation matrix, with $k < v$. We calculate matrix T by applying Singular Value Decomposition (SVD) [138] to the covariance matrix C of the original dataset:

$$\mathcal{C} = MM^T = W \Lambda W^T. \tag{2.2}$$

Here, $W \in \mathbb{R}^{v \times v}$ is an orthogonal matrix ($WW^T = I$) containing the eigenvectors of $\mathcal{C}$ (Principal Components or PCs) columnwise , and Λ is a diagonal matrix with the eigenvalues of $\mathcal{C}$. The transformation matrix T is formed by the first k columns of W. Hence, the latent representation Z contains the data features compressed into the k-dimensional space. We can apply the inverse operation as:

$$\hat{M} = T^T Z = T^T T M. \tag{2.3}$$

This operation remaps the data back into the original space with minimal reconstruction error: $E = M - \hat{M}$. Figure 2.1 shows an example of PCA projection from a three-dimensional original data space to a two-dimensional one.

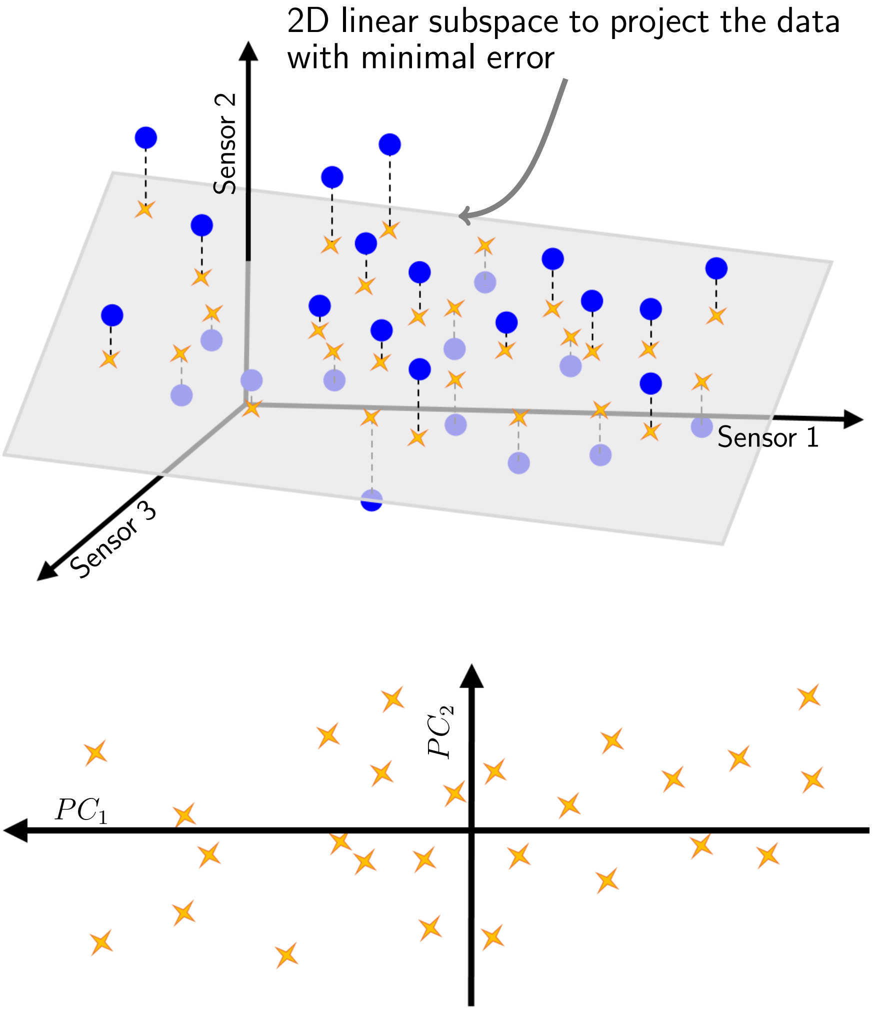

Figure 2.1: Example of PCA projection from a 3D to a 2D space

2.3 Autoencoders

Autoencoders are a specific DNN type based on the same idea of data compression and reconstruction as PCA, but including nonlinearities [115]. An autoencoder contains two parts: an encoder and a decoder [17].

For a certain measurement $\mathbf{m} = (m_1, m_2, ..., m_v)^T$ in the original dataset $M \in \mathbb{M}^{n \times v}$, the encoder $\mathcal{F}_E : \mathbb{R}^v \to \mathbb{R}^k$ compresses the data onto a k-dimensional representation $\mathbf{z} = \mathcal{F}_E(\mathbf{m}; \boldsymbol{\theta}_E)$, with $\boldsymbol{\theta}_E$ being the encoder NN parameters. The decoder $\mathcal{F}_D : \mathbb{R}^k \to \mathbb{R}^v$ reconstructs the original measurements from the lower-dimensional features $\hat{\mathbf{m}} = \mathcal{F}_D(\mathbf{z}; \boldsymbol{\theta}_D)$, where $\boldsymbol{\theta}_D$ contains the decoder parameters [68]. As with any NN, the encoder and the decoder apply a composition of a series of affine transformations followed by element-wise nonlinear activation functions throughout l_E and l_D layers, respectively. We express both terms as:

$$\mathcal{F}_E(\mathbf{m}; \boldsymbol{\theta}_E) = N \circ A_E^{l_E} \circ N \circ A_E^{l_E - 1} \circ ... \circ N \circ A_E^1 \ . \tag{2.4}$$

$$\mathcal{F}_D(\mathbf{z}; \boldsymbol{\theta}_D) = N \circ A_D^{l_D} \circ N \circ A_D^{l_D - 1} \circ ... \circ N \circ A_D^1 \ . \tag{2.5}$$

Here, N is a nonlinear activation function (e.g. ReLu); $A_i^j = W_i^j \mathbf{x} + \mathbf{b}_i^j$ indicates an affine transformation with weights W_i^j, bias $\mathbf{b}_i^j$ and input data $\mathbf{x}$; and symbol $\circ$ indicates composition operation. Figure 2.2 shows the standard autoencoder architecture.

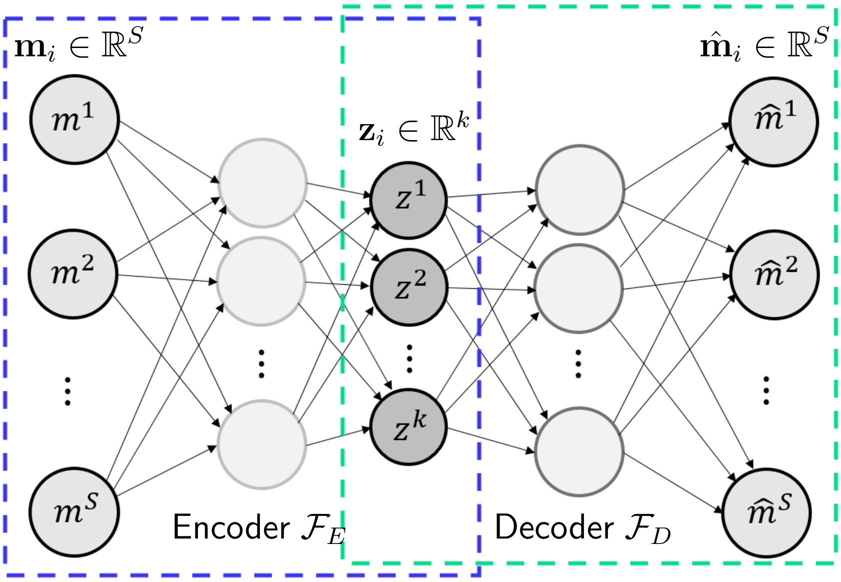

Figure 2.2: Standard architecture of an Autoencoder

Autoencoders introduce nonlinear functions into the reconstruction process. Determining the enhancement of this approach over linear transformations requires first replicating PCA results in terms of reconstruction. But given its NN topology as an alternate composition of affine and nonlinear functions, the standard autoencoder architecture is unable to map the vector subspace of affine transformations that include PCA. This prevents evaluating the contribution of nonlinearities over the linear approach, yielding a non-explainable NN. Besides, it is unclear if the selected architecture (number of layers and neurons) will outperform PCA.

2.4 Residual Autoencoder Architecture

We design a novel deep autoencoder architecture that is explainable. Figure 2.3 shows the block-wise topology of the network. The black-colored blocks contain the standard encoder and decoder architectures with the composition of affine and nonlinear transformations. By adding parallel connections (blue-colored blocks), we skip the nonlinear operations involved in $\mathcal{F}_b$ and $\mathcal{F}_d$. This approach allows to map the subspace of affine transformations and reproduce PCA. The following equations describe the operations at each block:

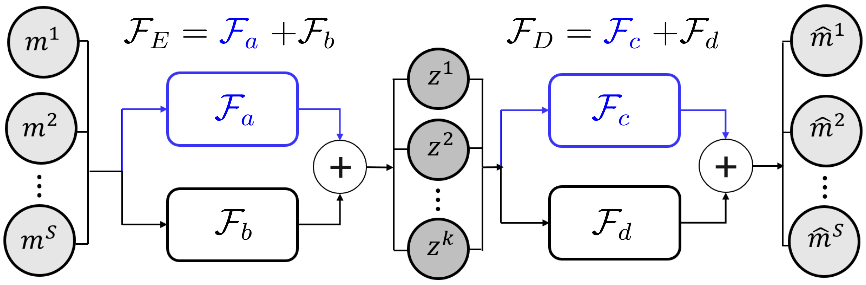

Figure 2.3: Proposed deep residual autoencoder architecture

$$\mathcal{F}_a(\mathbf{m}; \boldsymbol{\theta}_a) = W_a \mathbf{m} + \mathbf{b}_a. \tag{2.6}$$

$$\mathcal{F}_c(\mathbf{z}; \boldsymbol{\theta}_c) = W_c \mathbf{z} + \mathbf{b}_c. \tag{2.7}$$

$$\mathcal{F}_b(\mathbf{m}; \boldsymbol{\theta}_b) = N \circ A_b^{l_b} \circ N \circ A_b^{l_b - 1} \circ \ldots \circ N \circ A_b^1. \tag{2.8}$$

$$\mathcal{F}_d(\mathbf{z}; \boldsymbol{\theta}_d) = N \circ A_d^{l_d} \circ N \circ A_d^{l_d - 1} \circ \ldots \circ N \circ A_d^1. \tag{2.9}$$

We can interpret this parallel architecture as a Residual Neural Network (RNN) [66], where the NNs in the blocks $\mathcal{F}_b$ and $\mathcal{F}_d$ represent the residual terms, and the blue blocks ($\mathcal{F}_a$ and $\mathcal{F}_c$) refer to the skip connections. Our skip connections are affine transformations instead of identity mappings, which are more general and can reproduce PCA.

This architecture endows the autoencoder with partial explainability since we can separate the contribution of linear and nonlinear transformations. When we deactivate the residual terms, the autoencoder applies two consecutive affine transformations ($\mathcal{F}_a$ and $\mathcal{F}_c$), analogous to PCA. As a result, the autoencoder will attain same or better-quality results than PCA transformations in terms of data reconstruction, under assumption of optimal network training.

Contrary to traditional PCA (and other statistical techniques), NNs require a training phase to obtain the optimal parameter values that solve the approximation of interest. The objective of the autoencoder is to recover the original measurements from their lower-dimensional representation. The reconstruction error $\rho(\mathbf{m})$ measures the misfit between an original data point $\mathbf{m}$ and its corresponding reconstruction $\hat{\mathbf{m}}$ using the squared l_2 norm:

$$\rho(\mathbf{m}) = \|\mathbf{m} - (\mathcal{F}_D \circ \mathcal{F}_E)_{\boldsymbol{\theta}}(\mathbf{m})\|_2^2, \tag{2.10}$$

where $\boldsymbol{\theta} = \{\boldsymbol{\theta}_a, \boldsymbol{\theta}_b, \boldsymbol{\theta}_c, \boldsymbol{\theta}_d\}$ contains the weight and bias parameters of the four modules that build the complete autoencoder, and $\circ$ stands for the composition operator.

Training the model consists of finding the parameter set $\boldsymbol{\theta}^*$ that minimizes a loss function $\mathcal{L}_{\boldsymbol{\theta}}$ based on the reconstruction error for the training dataset $\mathbf{M}$:

$$\mathcal{L}_{\boldsymbol{\theta}*} := \arg\min_{\boldsymbol{\theta}} \|\mathbf{M} - (\mathcal{F}_D \circ \mathcal{F}_E)_{\boldsymbol{\theta}}(\mathbf{M})\|_2^2 \tag{2.11}$$

Here, we perform a two-step training to evaluate the enhancement of adding nonlinear terms to the linear autoencoder that approximates PCA.

2.4.1 Training step 1

During the first step, we deactivate the nonlinear blocks of the architecture ($\mathcal{F}_b$ and $\mathcal{F}_d$) and train only for the linear blocks ($\mathcal{F}_a$ and $\mathcal{F}_c$). This yields the final linear autoencoder, with parameters $\boldsymbol{\theta}_a^*$ and $\boldsymbol{\theta}_c^*$. Figure 2.4 represents the architecture of the linear autoencoder, where the nonlinear terms are deactivated.

PCA is a particular solution to this linear problem that satisfies particular restrictions [72]. By definition, principal components are orthonormal and produce uncorrelated $\mathbf{z}$ features [72]. To attain the exact solution of PCA (i.e., transformation matrix T in equation 2.1), we can impose these constraints on the

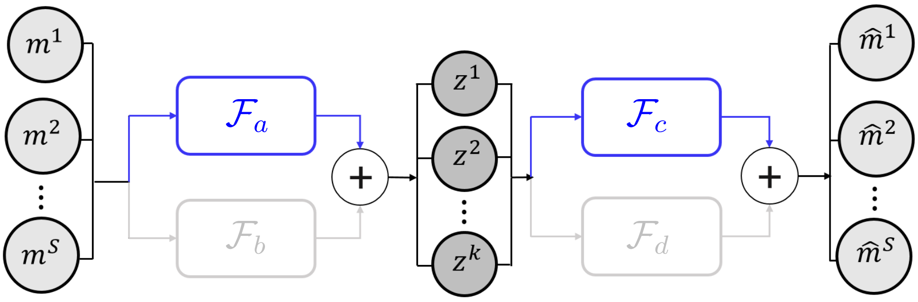

$$\mathcal{L}_{\boldsymbol{\theta}^*}^{Step\ 1} := \arg\min_{\boldsymbol{\theta}} \|\mathbf{M} - (\mathcal{F}_a \circ \mathcal{F}_c)_{\boldsymbol{\theta}}(\mathbf{M})\|_2^2$$

Figure 2.4: Step 1: train the linear autoencoder

weight matrix W_a as well as $W_c = W_a^T$ during the training phase. In such a case, $\mathbf{b}_a \in \mathbb{R}^v$ and $\mathbf{b}_c \in \mathbb{R}^k$ are null vectors, and the weight matrices $W_a \in \mathbb{R}^{v\times k}$ and $W_c \in \mathbb{R}^{k\times v}$ contain the first k eigenvectors of the covariance matrix $\mathcal{C}$ columnwise and row-wise, respectively. Focusing on data reconstruction, we can employ a linear autoencoder that replicates PCA or any other solution that captures the same level of information. If we impose no constraints, the linear autoencoder obtains a different but valid solution in terms of data reconstruction.

2.4.2 Training step 2

In the second step, we activate the nonlinear connections to build the residual autoencoder. Instead of retraining the linear blocks, we freeze the parameter values obtained during step 1 and train only the residual ones. With this approach, we continue the training from the linear solution, allowing to measure the enhancement of the residual terms. Figure 2.5 shows the second training step, where $\mathcal{F}_a^*$ and $\mathcal{F}_c^*$ stand for the linear blocks optimized during step 1.

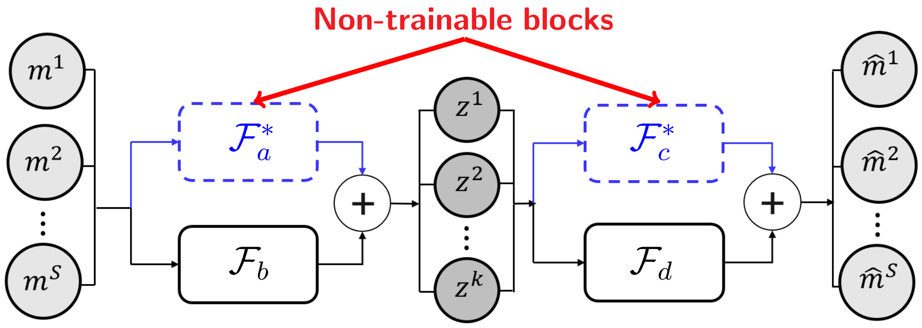

$$\mathcal{L}_{\boldsymbol{\theta}^*}^{Step\ 2} := \arg\min_{\boldsymbol{\theta}} \|\mathbf{M} - (\mathcal{F}_D \circ \mathcal{F}_E)_{\boldsymbol{\theta}}(\mathbf{M})\|_2^2$$

Figure 2.5: Step 2: train the residual autoencoder

2.5 Unsupervised SHM strategy: outlier detection

The final goal of the methodology is to detect abnormal behavior of bridges from experimental measurements acquired during monitoring. We train the residual autoencoder with measurements from the undamaged (healthy) condition. The reconstruction error is expected to be small for unseen measurements that correspond to this state. But if we evaluate new data coming from a different scenario (namely, a damaged one), the autoencoder will poorly reconstruct them.

We employ the reconstruction error ρ as the damage-sensitive indicator. The threshold value α for outlier detection is the 99 percentile of the training dataset. For a new measurement $\mathbf{m}_{new} \in \mathbb{R}^v$ acquired within a future monitoring campaign, we obtain the reconstruction error and compare it against the threshold value. Algorithm 1 describes this procedure.

Algorithm 1: Reconstruction error-based outlier detection

```
Input: $\mathbf{m}_{new} \in \mathbb{R}^v$, $\mathcal{F}_E$, $\mathcal{F}_D$, $\boldsymbol{\theta}^*$, $\alpha$
Output: $\rho$
Compute the reconstruction error: $\rho = \|\mathbf{m}_{new} - (\mathcal{F}_D \circ \mathcal{F}_E)_{\boldsymbol{\theta}*}(\mathbf{m}_{new})\|_2^2$
if $\rho > \alpha$ then
    $\mathbf{m}_{new}$ is abnormal, indicate outlier
else
    $\mathbf{m}_{new}$ is healthy
```

2.6 Results using quasi-static data

Here we present results obtained with data from monitoring systems recording local variables (quasi-static measurements such as displacements or inclinations) instead of dynamic response in the frequency domain.

2.6.1 Beltran bridge in Mexico

We apply the proposed method to assess the global behavior of an asymmetric prestressed concrete viaduct in Mexico: the Beltran bridge. The bridge contains four sliding bearings at the deck-pier contacts to allow for relative displacements and limit the horizontal loads reaching the piers. But if these devices lose their sliding properties, large displacements and subsequent cracking can occur at the pier caps. Garcia-Sanchez et al. [53] provide further details. Figure 2.6 shows the profile of the bridge.

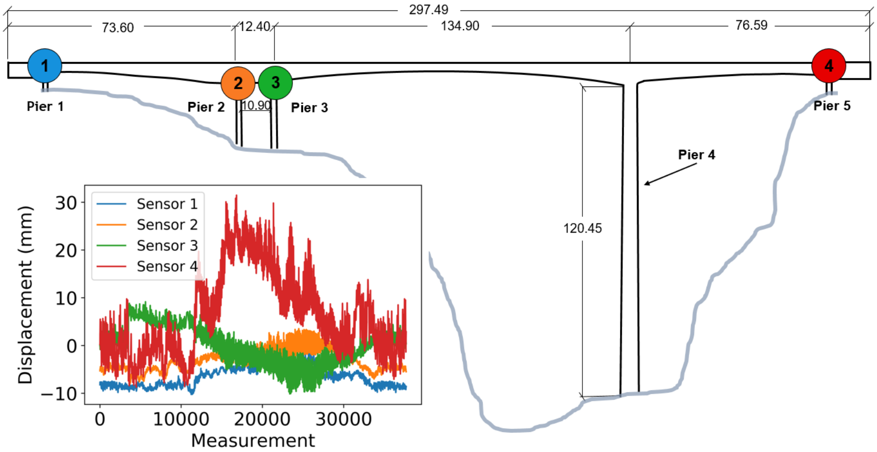

Figure 2.6: Beltran bridge profile with sensor location

The monitoring campaign used fiber optic sensors and was active from August 2012 to August 2013. Due to occasional shutdowns of the system, the effective monitoring time was of approximately nine months. We employ time series from four longitudinal displacement sensors (see Figure 2.6). The data was acquired at a sampling frequency of 200 Hz, and the mean value was calculated and stored every ten minutes for each sensor. This sub-sampling considerably reduces the storage space while permitting the analysis of long-term variations. After this pre-processing step, we have four sensor signals ($v = 4$) with 37,692 measurements each. We employ the first 90% of the data randomly split into 85% for training and 15% for validation. We use the final 10% for testing purposes. We

Table 2.1: Comparison of PCA and constrained linear autoencoder

PCA		**Constrained approach**		**Unconstrained approach**			
PC1	PC2	$\mathbf{w}_a^1$	$\mathbf{w}_a^2$	$\mathbf{w}_a^1$	$\mathbf{w}_a^2$	$\mathbf{w}_c^1$	$\mathbf{w}_c^2$
0.5365	0.1071	0.5362	0.1077	-0.6544	0.4597	-0.2502	0.2914
0.4957	-0.5296	0.4954	-0.5308	-1.0375	-0.1796	-0.4716	-0.2116
-0.5078	0.3025	-0.5084	0.3016	0.8989	-0.0449	0.3907	0.0359
0.4567	0.7852	0.4750	0.7846	-0.0789	1.0556	0.0450	0.7865
Captured: 90.41%		Captured: 90.41%		Captured: 90.41%			

adapt the architecture described in section 2 to fit the four-dimensional input. The nonlinear connections are symmetric and contain three layers each. This architecture provides adequate results. We first train for the linear autoencoder (training step 1) for a two-dimensional compression. We design the linear autoencoder to replicate PCA by imposing the constraints that hold for the principal components. Table 2.1 compares the transformation matrices of traditional PCA (PC1 and PC2 stand for the first two principal components of the training data covariance matrix), the designed linear autoencoder with the constraints, and an unconstrained approach with null bias terms. We observe that the three configurations capture the same level of information. In subsequent steps in this work, we employ the constrained linear autoencoder that replicates PCA results.

After solving the linear autoencoder, we incorporate the nonlinear connections ($\mathcal{F}_b$ and $\mathcal{F}_d$) to build the nonlinear autoencoder. According to the two-step training, we fix the previously obtained weight matrices and only train the nonlinear modules. Figure 2.7 shows the evolution of the loss functions for the training and the validation datasets for the two training steps. The number of epochs indicates the repetitions over the training dataset to minimize the loss function. We observe in figure 2.7a that the first training step (linear autoencoder) converges after just 50 epochs with a loss function value of 0.0946 for the training dataset. Figure 2.7b shows the effect of adding the nonlinear connections to the linear autoencoder (training step 2). The loss function decays to a value of 0.0171 after 300 epochs. When the output dimension of the encoder is equal to two, the amount of information captured during training raises from 90.41% to 98.05% when we add the deep nonlinear connections. This means that the nonlinear terms contribute to reduce the reconstruction error from 9.59% to 1.95% ($\approx$ 80%

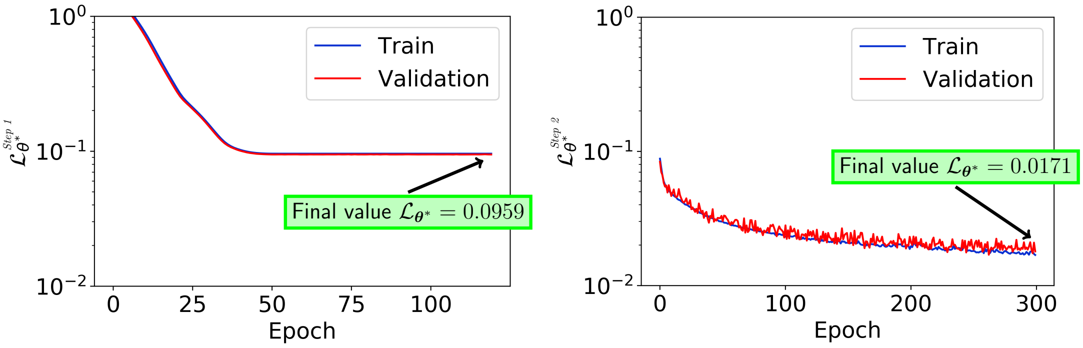

(a) Loss evolution during training: step 1 (b) Loss evolution during training: step 2

Figure 2.7: Loss function evolution for the Beltran bridge dataset

error reduction). When the output dimension of the encoder is reduced to one, the level of captured information is below 90% for both architectures. This makes impractical the outlier detection task.

For comparison, we implemented a kernel PCA and tried different kernel functions (radial basis (rbf) and cosine functions) [69]. For the rbf function, we attained a 42.99% of information captured, and a 76.77% was attained for the cosine function. Since the real distribution of the data is unknown, it is nontrivial to find a kernel function that outperforms the linear solution.

We analyze the reconstruction ability of the two configurations via the crossplots (ground truth vs predictions) of the sensor signals. Here, the ground truth are the measurements of each sensor, and the predictions are the reconstructed variables. The square of the correlation coefficient r^2 provides a numerical measure of the correlation between ground truth and prediction for each sensor (see Table 2.2). Figure 2.8 compares the crossplot corresponding to sensor 1 for the linear and the nonlinear models. We observe a superior performance for the complete model with nonlinearities.

We finally determine the threshold value α as the 96th percentile (p-96) over the training reconstruction errors. We select a percentile vallue that ensures a rate of false positives below 5% as well as delivers adequate equilibrium between false positves and negatives. Figure 2.9 shows the histograms for the linear and nonlinear autoencoder training reconstruction errors, and the corresponding threshold values.

2.6.1.1 Testing results

We now test the ability of both autoencoder configurations in the detection of outliers. We use the testing dataset that contains the final 10% of the data. We

Table 2.2: r^2 metric for the sensors in Beltran bridge

Sensor ID	Sensor type	Linear model	Residual model
1	Displacement	0.891	0.978
2	Displacement	0.908	0.981
3	Displacement	0.842	0.981
4	Displacement	0.975	0.988

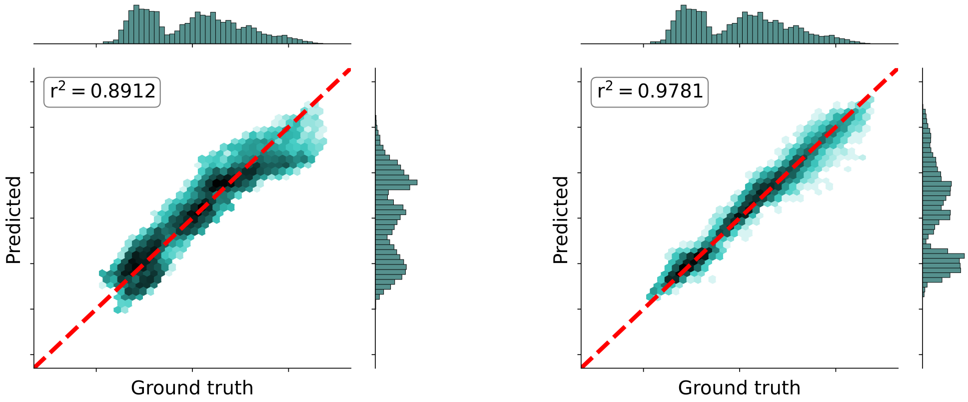

(a) Linear auteoencoder

(b) Residual autoencoder

Figure 2.8: Beltran bridge training crossplots for sensor 1

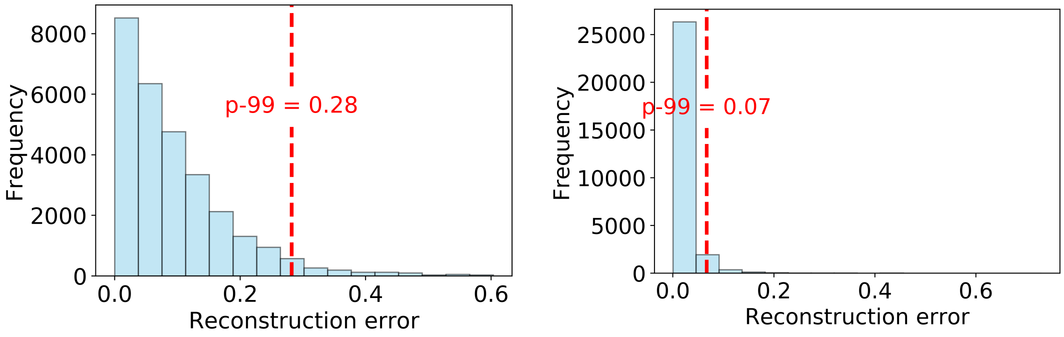

(a) Linear autoencoder

(b) Nonlinear autoencoder

Figure 2.9: Beltran bridge reconstruction error training histograms

simulate damage by reducing the displacement measurements at one of the sensors to represent a loss of sliding properties at that bearing. We do so by applying a reduction factor to the measurements of sensor 1. Figure 2.10 shows the location of the damage in the bridge. We consider three different damage levels: 50%, 30% and 20%. For each level of damage, we duplicate the test data set and apply the reduction factor to the second half of the measurements [53]. Figure 2.11 compares the control charts for the three damage levels. The shadowed regions in Figure 2.11 cover the part of the testing affected by damage.

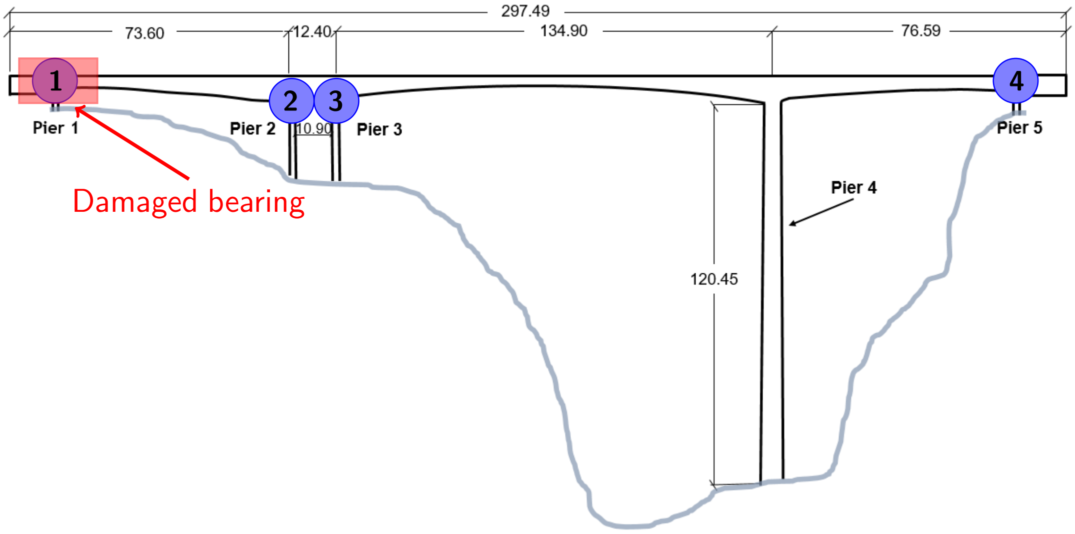

Figure 2.10: Location of the testing damage at Beltran bridge

Table 2.3 gathers the fraction (%) of false positves (FP) and false negatives (FN) for each case. The presence of false positives occurs probably due to the short length of the monitoring period (less than a year). The training phase covers a limited range of environmental variations and the testing dataset includes data from a healthy scenario that corresponds to an unseen month of the year. We believe we can overcome this with longer monitoring campaigns. We also observe that the linear autoencoder needs stronger damages to be able to detect it. While the deep nonlinear autoencoder still detects a damage of 30% with less than 3% of false negatives, the linear autoencoder considerably fails for that scenario. For a damage severity of 20% affecting the bearing, the nonlinear autoencoder increases the rate of FN but still detects it.

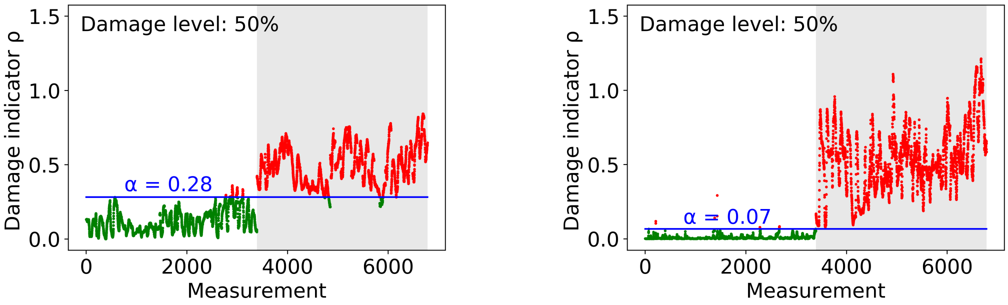

(a) Linear auteoencoder (b) Residual autoencoder

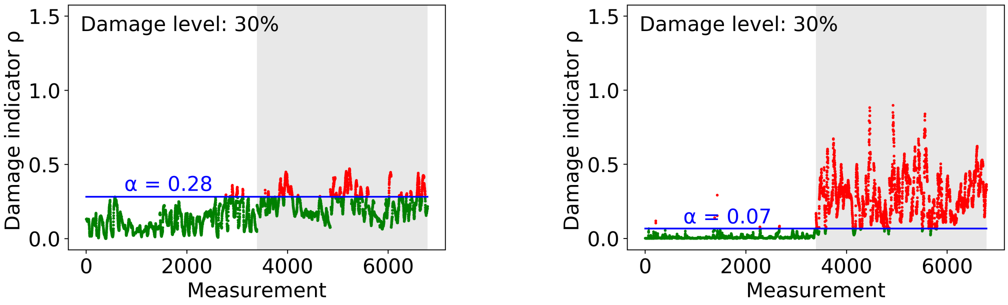

(c) Linear auteoencoder (d) Residual autoencoder

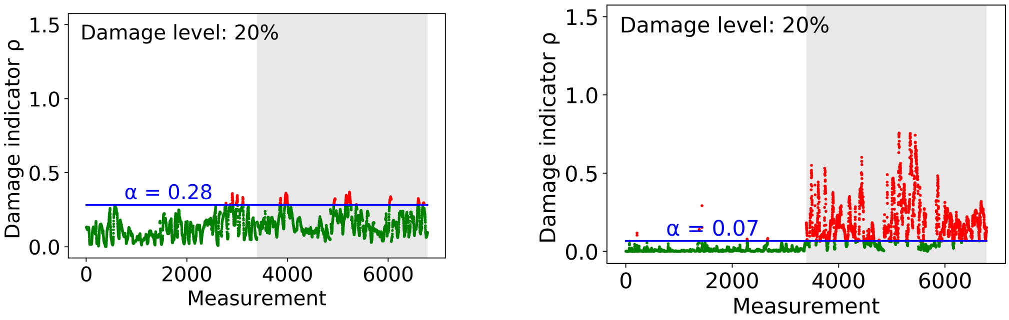

(e) Linear auteoencoder (f) Residual autoencoder

Figure 2.11: Beltran bridge testing control charts

2.6.2 Infante Dom Henrique bridge in Porto

The Infant Dom Henrique bridge was opened to road traffic in 2002 between the cities of Vila Nova de Gaia and Porto. It consists of a rigid prestressed reinforced concrete box-beam deck supported over a 1.50 m thick reinforced concrete arch. This is a unique structure that achieved a world record due to the shape of its arch span of 280 m to cross river Douro. More detailed information regarding its structural aspects can be found in Fonseca et al. [33]. Given the particularities of the bridge, a monitoring system was installed to control construction and assem-

Table 2.3: Outlier detection results for Beltran bridge.

Architecture type	**Damage level(%)**	**FP(%)**	**FN(%)**
Linear	50	2.30	3.15
Residual	50	1.26	0.00
Linear	30	2.30	73.93
Residual	30	1.26	2.89
Linear	20	0.12	91.80
Residual	20	1.26	15.63

bly operations, being afterwards also used to assess the long-term behavior. It employs several sensors located at the main sections of the bridge, registering one data point per hour. There are three types of sensors: strain gauges, clinometers, and thermometers. Magalhães et al. [3] provide further information regarding sensor properties and location, as well as monitoring aspects.

Although the monitoring campaign covered more than ten years of service life of the bridge, there occurred some shutdowns of the system that prevented the records to be continuous. For this reason, in this work we employ five years of monitoring, which are practically free from failures. For the particular purpose of this work, we consider 16 sensors located at six sections that are relevant for the structural behavior. The selected sensors were free from important shutdowns and included eight clinometers and eight strain gauges. Figure 2.12 shows the profile of the bridge and indicates the location of the sensors. Sections S_1, S_2, S_5 and S_6 contain two inclinometers each, but at section S_6 we discard one of the sensors due to low signal quality. Figure 2.13 shows the evolution of the seven selected

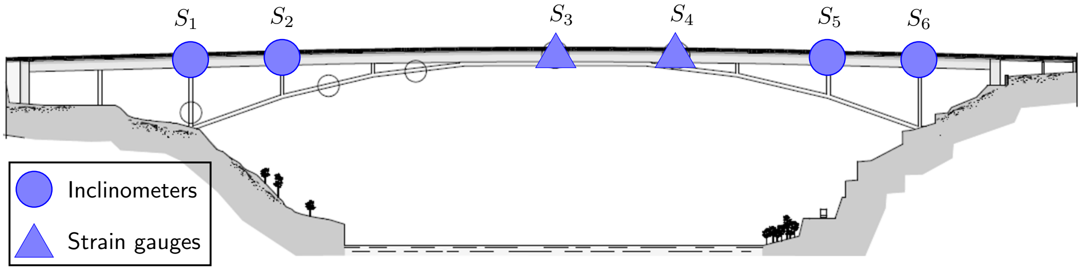

Figure 2.12: Infante D. Henrique bridge profile with sensor location

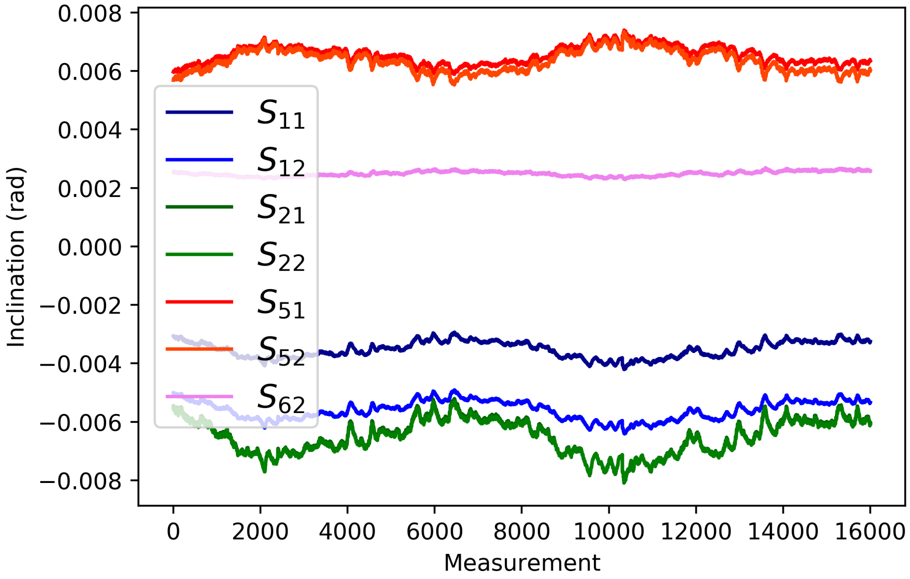

Figure 2.13: Evolution of the seven inclinometers between 2007 and 2010

inclination signals over the frist three years of the monitoring period. Sections S_3 and S_4 include four strain gauges, but in section three one is discarded due to low signal quality. Figure 2.14 shows the evolution of the selected stress time-series during three years of the monitoring period. We denote each sensor as $S_{i,j}$, with i indicating the instrumented section where it is located and j being the sensor number. More details regarding the exact location of the sensors can be found in Fonseca et al. [3]. We remove null values and obtain a total of 14 sensor signals with 34,641 measurements each. We use the first 90% of these data with a random split into 80% training and 20% validation.

We adapt the autoencoder architecture for a 14-dimensional input. In this case, the nonlinear connections are also symmetric and consist of six layers each. This number of layers provides adequate results and the architecture has not been further optimized. We solve the first training step (only $\mathcal{F}_a$ and $\mathcal{F}_c$ are active) for a two-dimensional compression. We design the linear autoencoder to approximate PCA by imposing the constraints satisfied by principal components. The information captured is similar to that of PCA (92.93%).

After solving the linear autoencoder, we incorporate the nonlinear connections ($\mathcal{F}_b$ and $\mathcal{F}_d$) that yield the nonlinear autoencoder. In order to evaluate the enhancement of the nonlinear connections over the linear approach, we fix the weight matrices obtained and train the nonlinear modules only. Figure 2.15 shows the loss functions for the training and validation datasets for both the linear and the nonlinear autoencoder. As with the Beltran bridge, we observe that the linear

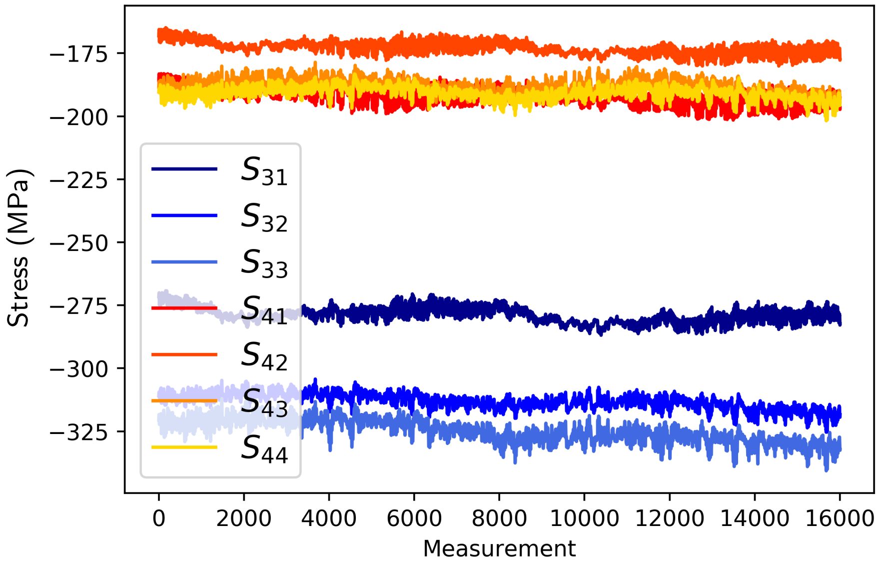

Figure 2.14: Evolution of the seven strain gauges over the monitoring period

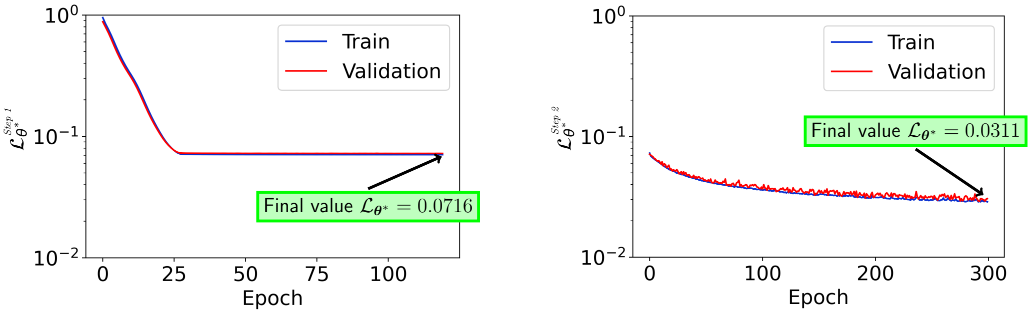

(a) Linear autoencoder (b) Residual autoencoder

Figure 2.15: Loss function evolution for the Infante bridge dasaset

model (see Figure 2.15a) converges with around 50 epochs at a value of 0.0716 for the training dataset. Figure 2.15b shows the effect of adding the nonlinear connections after 300 epochs, with the loss function reaching a value of 0.0311 for the training dataset. For a compression into a two-dimensional vector, the captured information during training raises from 92.93% to 97.05% after adding the nonlinear connections, indicating an enhancement in the reconstruction. A compression into a one-dimensional vector provides a level of captured information below 90% for both architectures, making impractical the outlier detection task.

Table 2.4: r^2 metric for the sensors in Infante bridge.

Sensor ID	**Sensor type**	**Linear Model**	**Residual Model**
S_{11}	Clinometer	0.993	0.992
S_{12}	Clinometer	0.994	0.993
S_{21}	Clinometer	0.995	0.993
S_{22}	Clinometer	0.996	0.994
S_{51}	Clinometer	0.985	0.989
S_{52}	Clinometer	0.990	0.991
S_{62}	Clinometer	0.863	0.954
S_{31}	Strain gauge	0.907	0.959
S_{32}	Strain gauge	0.944	0.978
S_{33}	Strain gauge	0.942	0.974
S_{41}	Strain gauge	0.833	0.929
S_{42}	Strain gauge	0.845	0.944
S_{43}	Strain gauge	0.780	0.929
S_{44}	Strain gauge	0.756	0.932
Average		0.916	0.962

For comparison, we implemented a kernel PCA and tried different kernel functions (radial basis (rbf) and cosine function)[69]. For example, the cosine function provided a 80.10% of information captured.

We analyze the reconstruction ability of the models via the crossplots (ground truth vs predictions) of the sensor signals. Table 2.4 shows the r^2-metric of each sensor for the two models. Figure 2.16 shows the correlation between the ground truth and the predictions for the training set (sensor 9), including the r^2 metric. Again, the deep nonlinear autoencoder exhibits superior performance. We finally obtain the threshold value α for outlier detection as the $p-98$ over the training reconstruction errors. Figure 2.17 shows the corresponding histograms for the two autoencoder architectures, indicating the threshold value.

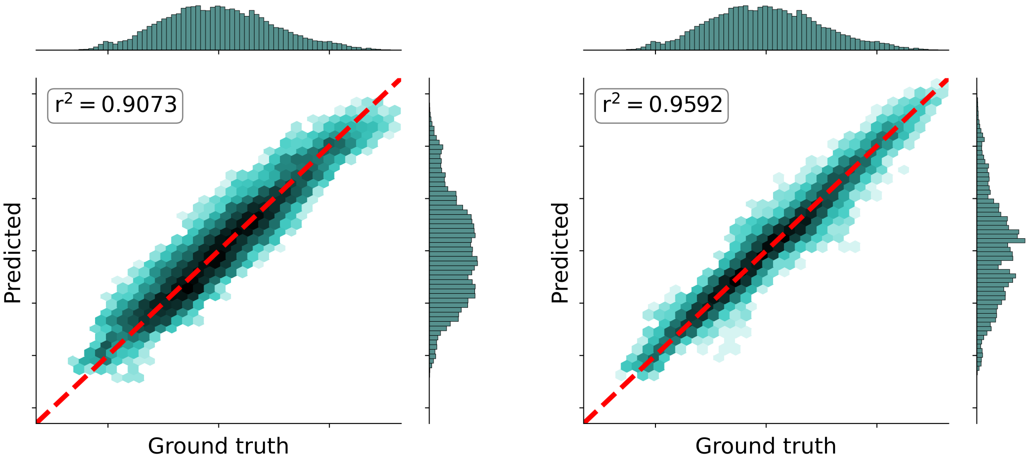

(a) Linear auteoencoder (b) Residual autoencoder

Figure 2.16: Training crossplots for sensor 9 (strain gauge) at Infante bridge

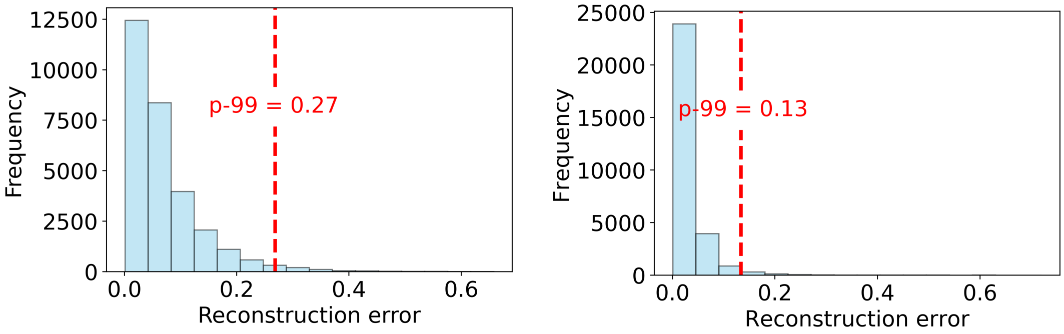

(a) Linear auteoencoder (b) Residual autoencoder

Figure 2.17: Infante bridge reconstruction error training histograms

2.7 Simulation of damage

Given the lack of experimental data in the presence of damage, numerical simulations are employed to represent some damage scenarios and test the detection ability of the proposed methodology. This procedure includes two steps: first, the synthetic responses of the system are obtained using FE model simulations that reproduce various damages with different locations and severity levels. Secondly, damaged testing datasets are constructed by applying the synthetic relative changes (between healthy and damaged responses) to the testing monitoring period to add environmental and operational variability. The following subsections describe the procedure.

2.7.1 Damage scenarios

We employ a FE model built in ANSYS® using 3D elastic beam-type elements. Figure 2.18 shows an extruded view of the FE model (not the real geometry of the cross-sections). This model was built by Magalhães et al. [86] and updated to obtain adequate responses compared to an ambient vibration test. The updating process focused on finding adequate constraints for the connections between the deck and the piers and abutments [86].

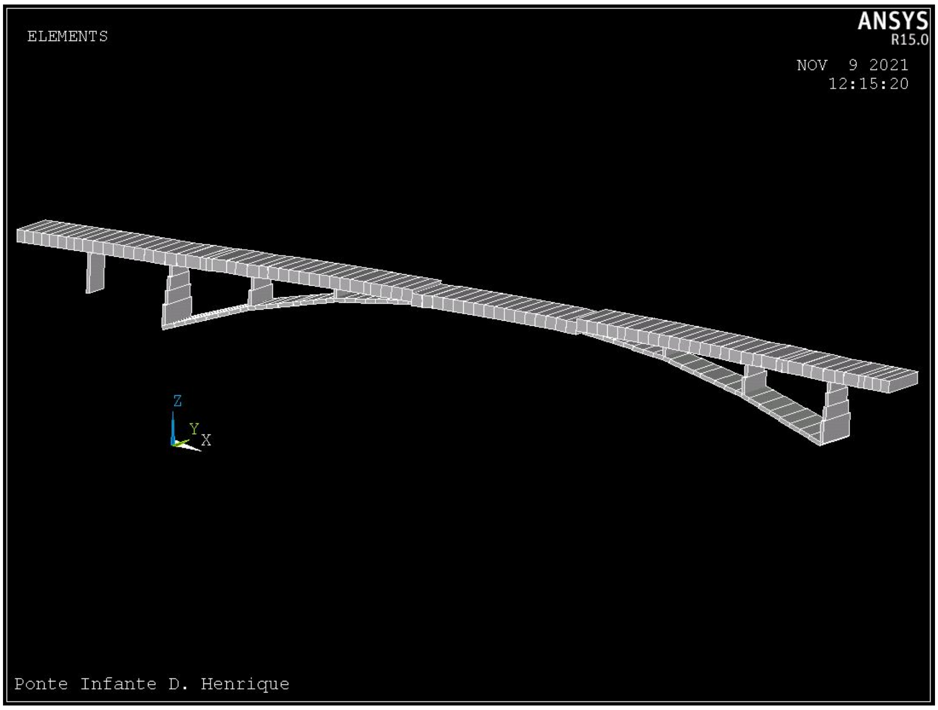

Figure 2.18: Extruded view of the FE model built in ANSYS®

Accurately simulating damage demands a huge computational effort and human expertise. These resources are often unavailable or unprofitable, and simpler approximations are needed. In this work, damage is feasibly simulated by reducing the inertial properties to represent a loss of vertical bending stiffness at small-length segments of the structure. This approach was first proposed and employed by Magalhães et al. [85] to reproduce possible consequences of aging phenomena, corrosion, or extreme events. Here, we investigate damage at section S_1 (see Figure 2.12) with three severity levels, namely 50%, 30%, and 20%, which correspond to the stiffness reduction at the affected section. We obtain the rota-

Table 2.5: Description of the damage scenarios for Infante bridge.

Damage level(%)	**Description**	**Average $\mathbf{d}_{rel}$**
50	Stiffness reduction	0.25
30	Stiffness reduction	0.12
20	Stiffness reduction	0.075

tions directly from static self-weight simulations. With the proposed approach, the differences in the damaged responses from the undamaged one are only due to the introduction of damage. We obtain the relative difference as:

$$\mathbf{d}_{rel} = \frac{\mathbf{m}^s_{dam} - \mathbf{m}^s_{und}}{\mathbf{m}^s_{und}}, \tag{2.12}$$

where $\mathbf{m}^s_{und}$ and $\mathbf{m}^s_{dam}$ correspond to the synthetic responses obtained in an undamaged and a damaged state, respectively. Table 2.5 describes the damage severity and indicates the average relative difference for the measurements of the two affected sensors emplaced in section S_1 according to Figure 2.12.

2.7.2 Damaged datasets

The proposed FE simulations lack consideration of environmental variability. Besides, since the monitoring system provides one observation per hour, running time-domain simulations becomes unfeasible to generate a representative dataset for evaluating the methodology. The experimental testing dataset (healthy) is employed as the target to embed the simulated damage scenarios and overcome the previous limitations. It is assumed that for any damage scenario, the relative differences $\mathbf{d}_{rel}$ hold in both the synthetic and experimental environments. In a simplistic approach, it is assumed that damage appears instantaneously and its effects are constant over time within the short testing period upon consideration. We generate a certain damaged dataset by applying the following transformation to each observation:

$$\mathbf{m}_{dam} = \mathbf{m}(1 + \mathbf{d}_{rel}), \tag{2.13}$$

In this analysis, three damaged datasets (one for each severity level) are built. The healthy testing dataset contains $N_{und} = 1,439$ observations that correspond to 10% of the monitoring data (unseen during training). Accordingly, each damaged dataset contains $N_{dam} = N_{und} = 3,663$ observations. For each damage scenario, the entire testing dataset includes the N_{und} healthy observations and the corresponding N_{dam} samples to evaluate the ability of the autoencoder as an outlier detector.

We finally feed the complete test dataset to the autoencoders and obtain the damage indicator (i.e. the reconstruction error, ρ) for each observation. Figure 2.19 shows the control charts of the damage indicator for outlier detection. The shadowed regions correspond to the part of the testing dataset affected by damage. Table 2.6 gathers the results in terms of false positives and false negatives. We observe that the incidence of false positives is very small for both the linear and

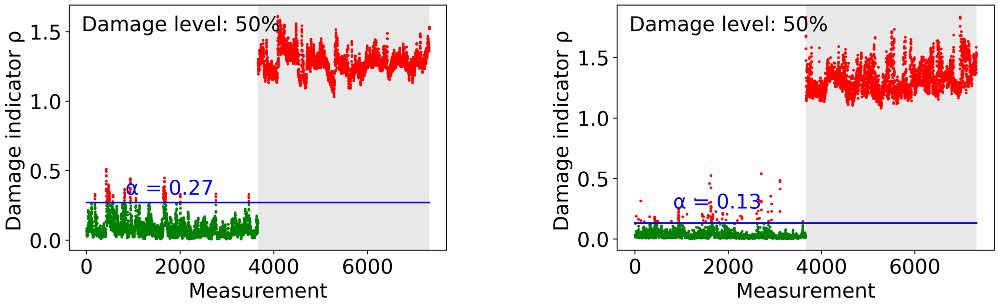

(a) Linear auteoencoder (b) Residual autoencoder

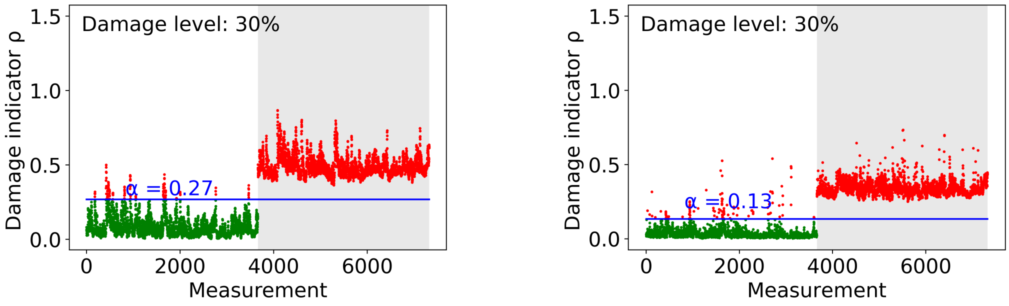

(c) Linear auteoencoder (d) Residual autoencoder

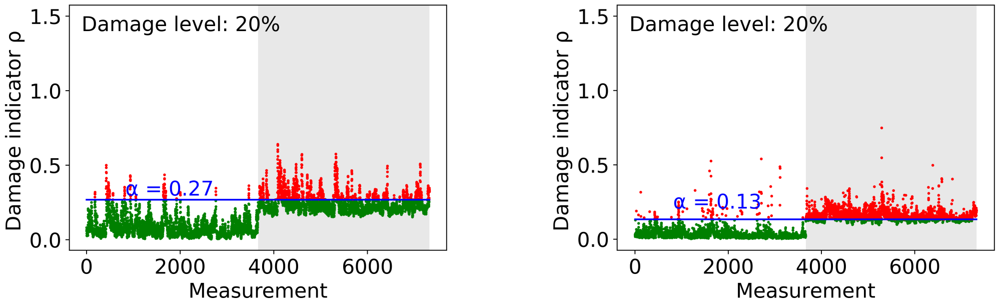

(e) Linear auteoencoder (f) Residual autoencoder

Figure 2.19: Infante bridge testing control charts

Table 2.6: Outlier detection results for Infante bridge.

Architecture type	**Damage level(%)**	**FP (%)**	**FN(%)**
Linear	50	3.03	0.00
Residual	50	0.71	0.00
Linear	30	3.03	0.62
Residual	30	0.71	0.00
Linear	20	3.03	89.08
Residual	20	0.71	10.67

the nonlinear autoencoders. Since the monitoring campaign covers five years, it is possible to train the networks for a wide enough range of environmental and operational variations. In terms of false negatives, the performance of both approaches is still good for a damage severity of 30%, but the linear autoencoder starts to raise some false negatives (below 1%). For a damage severity of 20%, the rate of change in the measurements is very small and thus reconstruction errors slightly increase. The linear autoencoder completely fails in the detection of this damage, while the nonlinear architecture presents close to 11% of false negatives.

2.8 Results combining static and dynamic data

In this section we investigate the potential of different measurable variables in the task of damage detection using the deep nonlinear autoencoder. We employ Infante Dom Henrique bridge as the case study, since a complementary long-term dynamic monitoring system was installed in 2007 [86]. This additional monitoring system measures acceleration signals from 12 uniaxial force balance accelerometers installed inside the deck box girder. Due to existing structural symmetry, only half of the bridge was monitored at four particular sections (see figure 2.20) [86]. There are four instrumented sections with three sensors each. One sensor measures lateral accelerations, and the others measure vertical accelerations upstream and downstream. Additional information can be found in Magalãhes et al. [86]. We employ measurements from the upstream vertical accelerations. Every half an hour, the system creates an ASCII file with 30-min time series sampled at 50 Hz that is subsequently post-processed using DynaMo [84] software to obtain estimates of the first twelve eigenfrequencies of the structure.

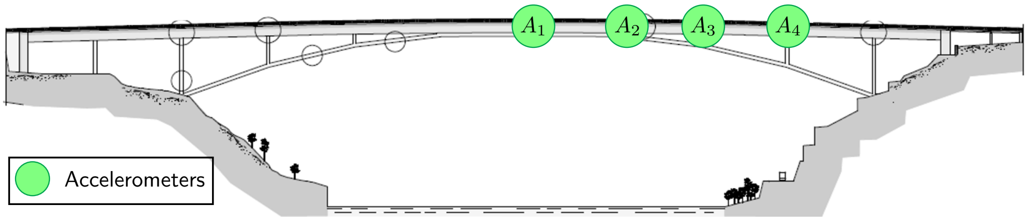

Figure 2.20: Instrumented cross-sections in the dynamic monitoring system

We combine measurements from the two aforementioned monitoring systems. We analyse three years of continuous monitoring data. The monitoring period extends from September 2007 to September 2010. We use measurements from inclinometers and strain gauges as the local variables (see Figure 2.12). We employ the eigenfrequencies produced with DynamMo software [84] as the global variables. Figure 2.21 shows the evolution of the first 12 eigenfrequencies (Hz) of the structure.

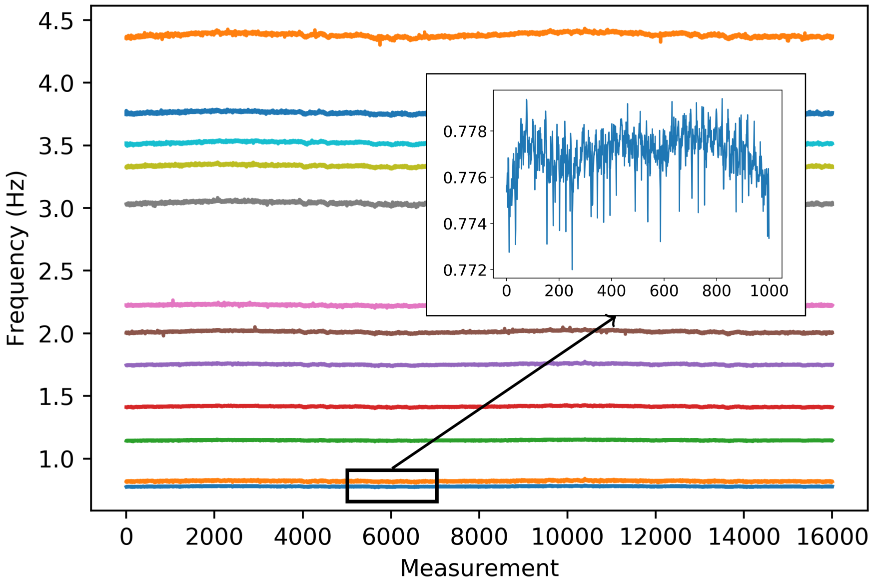

Figure 2.21: Evolution of the first 12 eigenfrequencies over the monitoring period. The squared window represents a subset of 1,000 measurements of the first eigenfrequency to show the variability over time

Since the local variables yield one measurement per hour whereas eigenfrequencies are produced every half an hour, we compute the mean of every two eigenfrequency measurements to use data from both monitoring systems with the same time resolution. After removing null values, we obtain a total of 16,005 measurements for each variable. We employ 72% of the samples for training and 18% for validation. The final monitoring period (remaining 10% of the data) is kept to investigate the method ability for damage detection using different variable combinations.

The final goal of the autoencoder is to detect abnormal responses in the structure from the value of the reconstruction error. If damage alters the structural response, the latent representation $\mathbf{z}$ will differ with respect to that learned for the undamaged observations, yielding a high reconstruction error ρ (outlier). We want to investigate the potential of combining local and global monitoring variables in damage detection. Hence, we design three different DNN architectures to accommodate the input dimension for i) local variables (DNN_{Local}), ii) global variables (DNN_{Global}), and iii) both local and global variables ($DNN_{Combined}$).

The three DNNs follow the scheme sketched in Figure 2.3. All the architectures are fully-connected with only dense layers. The linear encoder $\mathcal{F}_a$ applies the affine transformation using a single dense layer with linear activation to compress the input to the k-dimensional latent vector. The same holds for the linear decoder $\mathcal{F}_c$, which expands the latent vector to the original input space. The nonlinear encoder $\mathcal{F}_b$ contains six hidden layers using ReLu activation function and an output layer linearly activated to reach the latent dimension. The architecture of the nonlinear decoder $\mathcal{F}_d$ is symmetric with respect to that of $\mathcal{F}_b$. The activation function is ReLu for all the hidden layers and linear at the output layer.

The architectures of DNN_{Local} and DNN_{Global} are identical except for their input dimensions that are 14 and 12, respectively. The hidden layers in the nonlinear encoder contain the following number of neurons: $[32, 36, 48, 36, 48, 24]$. The encoding dimension is $k = 3$. In the case of $DNN_{Combined}$, which has a 26-dimensional input, the hidden layers have twice as many units as those in DNN_{Local} or DNN_{Global}, and the encoding dimension is $k = 8$. This expansion broadens the search space (more trainable parameters) when working with the combination of variables. The networks are trained and validated with long-term monitoring data corresponding to the healthy state of the bridge (unsupervised learning). This period covers two years of environmental and operational variability. It is expected that new (unseen) measurements corresponding to the healthy state will produce a feature vector $\mathbf{z}$ similar to those of the training observations and thus yield a small reconstruction error. But if the new measurements correspond to a damaged scenario, it is expected the network will poorly reconstruct them, delivering a high reconstruction error. Table 2.7 summarizes the main characteristics of each architecture and the training specifications. In all cases we employed Adam optimizer [74] with a learning rate of 10^{-3} and a batch size of 1,024 samples. The network architectures and training procedures were implemented using Tensorflow 2.8 [62].

Table 2.7: Summary of architecture and training specifications

ID	**Input dimension**	**k**	**Parameters**	**Epochs**
DNN_{Local}	14	3	16,582	800
DNN_{Global}	12	3	16,438	800
$DNN_{Combined}$	26	8	65,380	1,800

Figure 2.22 shows the evolution of the loss function during training and validation for the three networks. It is observed that local and global variables independently reach convergence before 800 epochs. An epoch represents an iteration over the entire dataset to minimize the loss function. For $DNN_{Combined}$, since the number of trainable parameters is much higher, the minimization process achieves convergence after approximately 1,800 epochs, yielding a better solution.

In this study, we investigate four damage locations with three severity levels of 5%, 10%, and 20%. Figure 2.23 shows the approximate locations of the studied damage cases (D1, D2, D3, and D4). Scenarios D1, D2, and D3 occur nearby instrumented deck sections, while D4 affects one column connecting arch and deck, and it is relatively far from the positions where local variables are recorded.

The synthetic global variables are derived from modal analyses using ANSYS eigensolver. The rotations are directly obtained from static self-weight simulations. To generate the stresses provided by the strain gauges, the vertical bending moments from the self-weight simulation are first obtained, and then the bending stress variations are calculated using the Navier formula for the considered inertia reductions. Tables 2.8and 2.9 gather the relative differences of local and global variables, respectively. In Table 2.8 the sensors with null relative difference ($d_{rel} = 0$) for all the considered damaged scenarios have been ommitted, namely S_{21}, S_{22}, S_{41}, S_{42}, S_{43}, and S_{44}. Similarly, in Table 2.9, we have omitted eigenfrequencies f_1 and f_5.

12 damaged datasets (one for each scenario and severity level) are built. The healthy testing dataset contains $N_{und} = 1,439$ observations that correspond to 10% of the monitoring data (unseen during training). Accordingly, each damaged dataset contains $N_{dam} = N_{und} = 1,439$ observations. For each damage scenario, the entire testing dataset includes the N_{und} healthy observations and the corresponding N_{dam} samples to evaluate the ability of the autoencoder as an outlier detector. Figures 2.24 and 2.25 show the effect of damage D1 with 10% severity

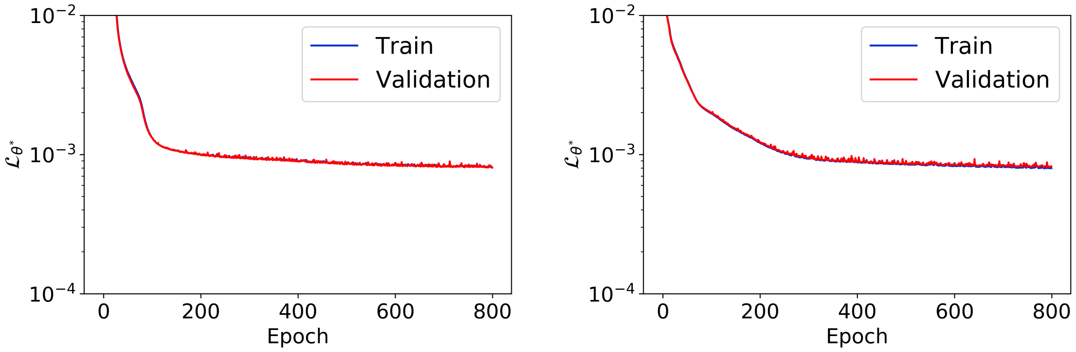

(a) Loss evolution for DNN_{Local} (b) Loss evolution for DNN_{Global}

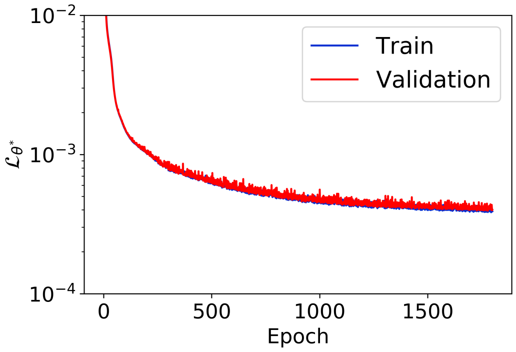

(c) Loss evolution for $DNN_{Combined}$

Figure 2.22: Loss evolution of the designed DNNs

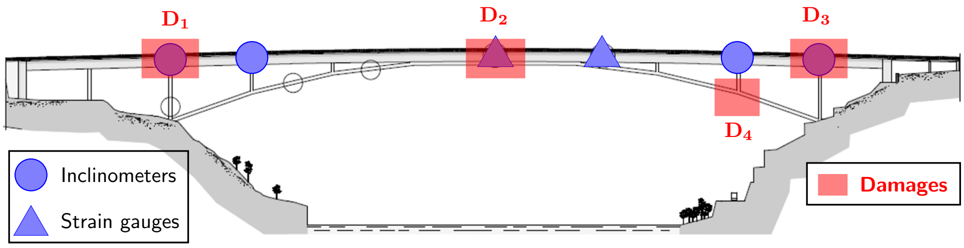

Figure 2.23: Location of the damage scenarios at Infante bridge

on sensor S_{11} and eigenfrequency f_4, respectively.

We employ the reconstruction error ρ (see equation 2.10) as the indicator to detect abnormal structural behavior. If damage alters the structural response, the latent representation $\mathbf{z}$ will differ from that learned for the undamaged observations, yielding a high reconstruction error ρ (outlier). To evaluate the performance in detecting structural damage, the Receiver Operating Characteristic (ROC) curves [18] are calculated. ROC curves are widely employed to measure

Table 2.8: Relative differences $d_{rel}(\%)$ for local variables.

	Severity	$\mathbf{S_{11}}$	$\mathbf{S_{12}}$	$\mathbf{S_{31}}$	$\mathbf{S_{32}}$	$\mathbf{S_{33}}$	$\mathbf{S_{51}}$	$\mathbf{S_{52}}$	$\mathbf{S_{62}}$
D1	5%	-1.61	1.61	0.00	0.00	0.00	0.00	0.00	0.00
	10%	-3.42	3.42	0.00	0.00	0.00	0.00	0.00	0.00
	20%	-7.54	7.54	0.00	0.00	0.00	0.00	0.00	0.00
D2	5%	0.00	0.00	4.94	4.94	4.94	0.00	0.00	0.00
	10%	0.00	0.00	10.43	10.43	10.43	0.00	0.00	0.00
	20%	0.00	0.00	23.47	23.47	23.47	0.00	0.00	0.00
D3	5%	0.00	0.00	0.00	0.00	0.00	0.00	0.00	-1.76
	10%	0.00	0.00	0.00	0.00	0.00	0.00	0.00	-3.61
	20%	0.00	0.00	0.00	0.00	0.00	0.00	0.00	-7.95
D4	5%	0.00	0.00	0.00	0.00	0.00	0.23	0.23	0.00
	10%	0.00	0.00	0.00	0.00	0.00	0.21	0.21	0.00
	20%	0.00	0.00	0.00	0.00	0.00	1.02	1.02	0.00

the performance of classifiers [47]. These curves represent the rate of false-positive predictions (FPR) against the rate of true-positive predictions (TPR).

In the context of SHM, a false positive indicates healthy data misclassified as damage, and a true positive indicates a correctly classified damaged scenario. Unsupervised learning results in a single-class classification, where undamaged data belong to the healthy class and any damaged scenario corresponds to an outlier [73]. The detection ability consists of classifying new unseen healthy observations as undamaged and detecting any departure as an outlier. False-positive and true-positive rates are obtained according to a threshold value α that establishes the maximum ρ value corresponding to the undamaged state. Measurements that produce error values above α are classified as damaged. When building the ROC curves, the value of α is varied to sweep the FPR within the interval [0,1]. A perfect classifier operates along the horizontal line at $TPR = 1$, and a random classifier would follow the diagonal line (45°) that crosses the ROC space [47].

Let $\rho_{t_{und}}$ and $\rho_{t_{dam}}$ denote the reconstruction errors for the undamaged and damaged testing subsets, respectively. The FPR and TPR for a threshold value (α) are obtained as:

$$FPR = \frac{\sum_{j=1}^{N_{und}} (\rho_{t^j_{und}} > \alpha)}{N_u}, \tag{2.14}$$

Table 2.9: Relative differences $d_{rel}(\%)$ for global variables.

	Severity	$\mathbf{f_2}$	$\mathbf{f_3}$	$\mathbf{f_4}$	$\mathbf{f_6}$	$\mathbf{f_7}$	$\mathbf{f_8}$	$\mathbf{f_9}$	$\mathbf{f_{10}}$	$\mathbf{f_{11}}$	$\mathbf{f_{12}}$
	5%	-0.08	-0.02	-0.07	-0.06	-0.03	0.00	-0.01	0.00	0.00	0.00
D1	10%	-0.17	-0.03	-0.14	-0.12	-0.06	0.00	-0.01	0.00	-0.00	-0.01
	20%	-0.38	-0.05	-0.31	-0.26	-0.13	0.00	-0.02	-0.00	-0.01	-0.02
	5%	0.00	-0.03	-0.03	0.00	-0.03	0.00	-0.00	-0.01	0.00	0.00
D2	10%	0.00	-0.06	-0.07	0.00	-0.07	0.00	-0.00	-0.03	0.00	-0.00
.	20%	0.00	-0.13	-0.14	-0.00	-0.16	0.00	-0.00	-0.06	-0.00	-0.00
	5%	-0.09	-0.02	-0.08	-0.07	-0.04	0.00	-0.01	0.00	-0.00	-0.00
D3	10%	-0.19	-0.03	-0.16	-0.14	-0.08	0.00	-0.01	-0.00	-0.00	-0.01
	20%	-0.41	-0.06	-0.35	-0.31	-0.17	0.00	-0.02	-0.01	-0.01	-0.03
	5%	-0.06	-0.01	-0.07	-0.01	-0.01	0.03	-0.12	-0.07	0.01	-0.00
D4	10%	-0.11	-0.01	-0.14	-0.03	-0.03	0.03	-0.25	-0.12	0.01	-0.00
	20%	-0.24	-0.02	-0.29	-0.06	-0.08	0.03	-0.53	-0.23	0.01	-0.01

$$TPR = \frac{\sum_{j=1}^{N_{dam}} \left(\rho_{t^j_{dam}} > \alpha\right)}{N_d}, \tag{2.15}$$

Figures 2.26to 2.28 compare the performance of the three designed DNNs for each type of damage to demonstrate the benefit of combining local and global variables. In the figures, the random classifier is represented with a grey dashed line. The performance increases as the curve moves away from the grey line and approximates the top of the ROC space.

Local variables exhibit good performance for damage scenarios D1 to D3, mainly for severity levels above 10% (see figures 2.27 and 2.28). In the case of damage D2, where three strain gauges are installed in the region affected by the damage, local variables yield a perfect classifier even for a slight severity level (see Figure 2.26). Since D3 occurs close to only one sensor (at S5), the sensitivity is lower than with damage D1 (similar damage at S1), where two inclinometers participate. But when damage occurs far from any instrumented section (D4), local variables turn insensitive and yield a poor classifier even for a high severity level (see Figure 2.28). Hence, the performance of local variables is adequate as long as the damage occurs nearby an instrumented section but strongly worsens for other damage locations.

These results are further analyzed by exploring the latent space for each damage scenario. Figure 2.29 compares the latent space representation of local variables for a 10% severity. Figure 2.29b highlights the sensitivity of strain gauges to damage with a huge difference between the healthy and the damaged latent rep-

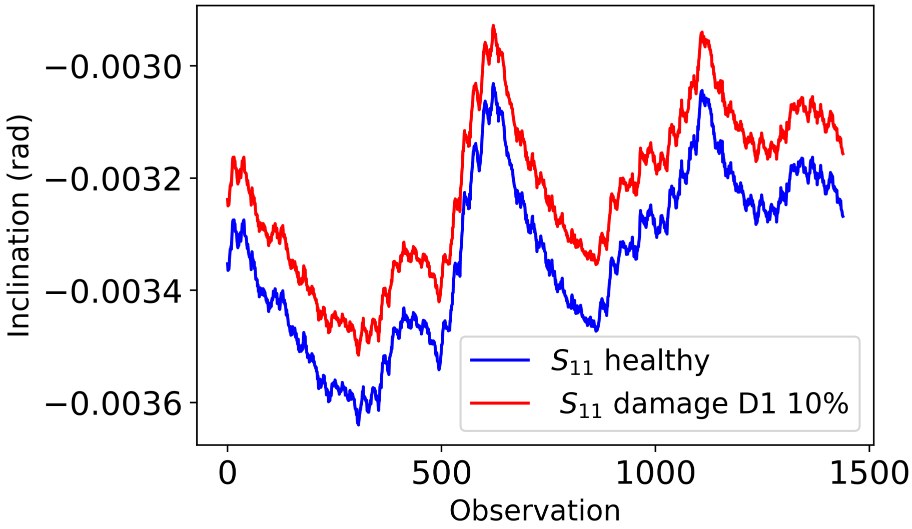

Figure 2.24: Effect of damage D1 with 10% severity on S_{11}

resentation. Figure 2.29d evidences that damage D4 barely affects local variables, making the healthy and the damaged latent representations overlap throughout the testing period.

On the other hand, global variables adequately detect the four damage scenarios when the severity reaches 20% (see figure 2.28). However, the performance decays for lower severity levels, indicating a limited sensitivity to slight damage, as shown in Figures 2.26 and 2.27. Figure 2.30 compares the latent space representation for each damage with 10% severity for global variables. Results are particularly deficient in the case of damage D2 (according to Figure 2.30d, only latent variable z_2 shows some variation with respect to the undamaged state). To explain this, the eigenmodes associated with the eigenfrequencies are analyzed. The shape of an eigenmode represents the vibration amplitude of each structural node when the bridge is excited at the corresponding eigenfrequency [65]. When damage occurs close to a node with reduced curvature for a certain eigenmode, the corresponding eigenfrequency will be poorly affected by changes in the bending stiffness. Thus, eigenfrequencies are more sensitive to damage that occurs close to nodes with higher curvatures.

Since damage was introduced as a vertical stiffness reduction, it mainly affects the vertical bending eigenmodes. In this case, only four out of the 12 global variables represent vertical bending eigenmodes and thus participate in detecting the proposed damage scenarios. The rest of the mode shapes are lateral and torsional. Figure 2.31 shows the four vertical bending mode shapes adopted in this work. Damage D2 occurs in the middle deck (see Figure 2.23) and it slightly

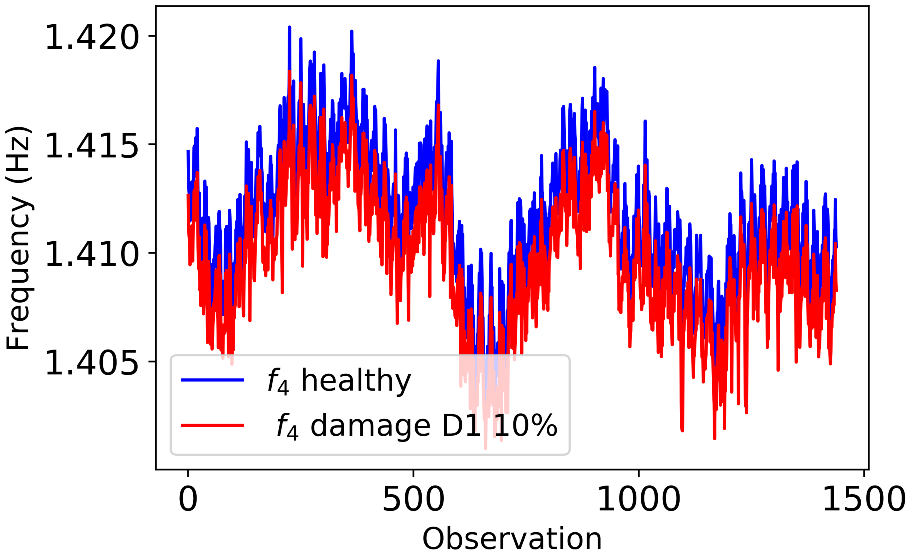

Figure 2.25: Effect of damage D1 with 10% severity on f_4

affects global variables due to the low curvature of the involved eigenmodes at this position (see mainly Figures 2.31a and 2.31d). Hence, although global variables increase the range of detectable damage compared to local variables alone, they still present some limitations, mainly for reduced severity levels. It is worth noting that DNN_{Global} achieves the best performance for damage D4 (see Figure 2.27d), which presented worse results when using local variables only.

In light of the previous observations, it becomes interesting to combine both sources of monitoring data. The red dashed line in Figures 2.26 to 2.28 reveals that combining local and global variables outperforms the classification ability of local or global variables alone. The ROC curves denote a multiplicative enhancement of the results that goes beyond the sum of the individual contributions of local and global variables. This becomes more evident mainly for ligher damages (see, for example 2.26c). In the case of damage D4, since the contribution of local variables is very low (see, e.g., Figure 2.28d), the combined solution practically coincides with the performance of global variables only. Figure 2.32 compares the 8-dimensional latent space representations of the damage scenarios (10% severity) with respect to the undamaged condition produced by $DNN_{Combined}$. Results show the discrepancies between damaged and undamaged latent representations (e.g., damage D1 mainly affects the second, seventh, and eighth dimensions, whereas damage D2 affects all of them).

In general, the obtained ROC curves for the combined approach are very good for severity levels of 10% (see Figure 2.27). The minimum detectable damage

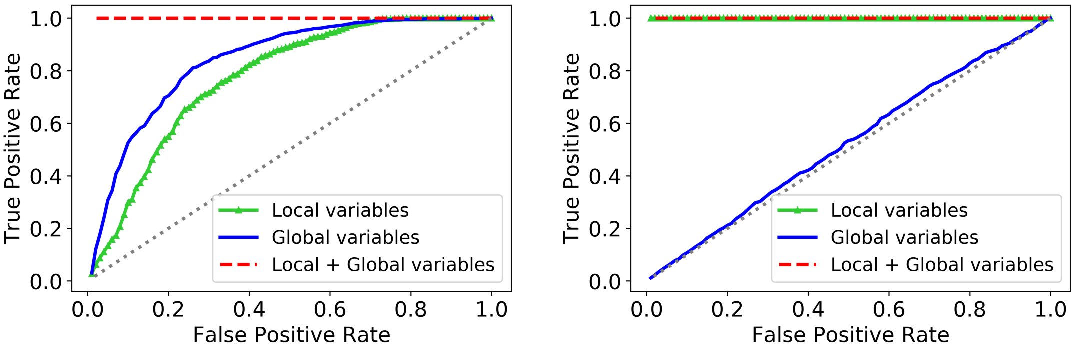

(a) Damage D1 5% severity (b) Damage D2 5% severity

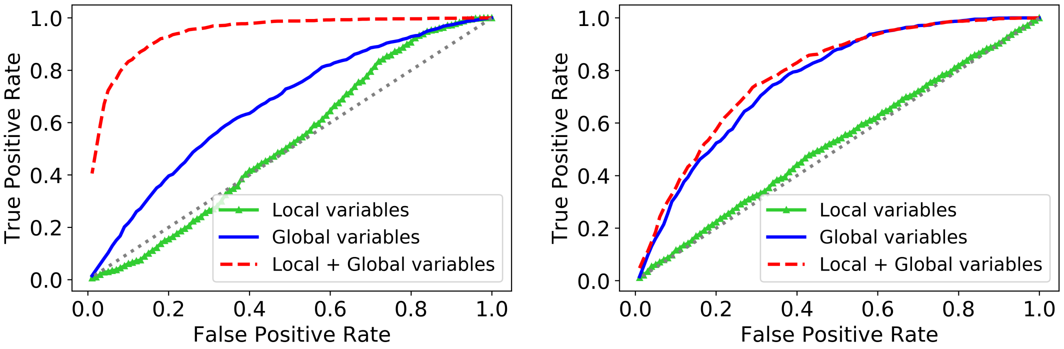

(c) Damage D3 5% severity (d) Damage D4 5% severity

Figure 2.26: ROC curves for damage severity 5%

can thus be established within the interval 5% – 10%, depending mainly on the contribution of local variables.

2.8.1 Damage location

In addition to detecting damage occurring nearby the sensor emplacement, local variables also contribute to determining the damage location. It is expected that the autoencoder yields an outlier ($\rho > \alpha$) when an abnormal behavior that affects the structural response registers through monitoring. It is assumed that this abnormal behavior corresponds to damage at any bridge location. Once the reconstruction error exceeds the threshold value (α) indicating damage, the contribution of local variables to the reconstruction error may be informative of the damage location. Here, the four damage scenarios considered for testing are investigated, whose location is known beforehand, to verify the capability of local variables in damage location.

It is assumed that if damage occurs nearby an instrumented section, it will

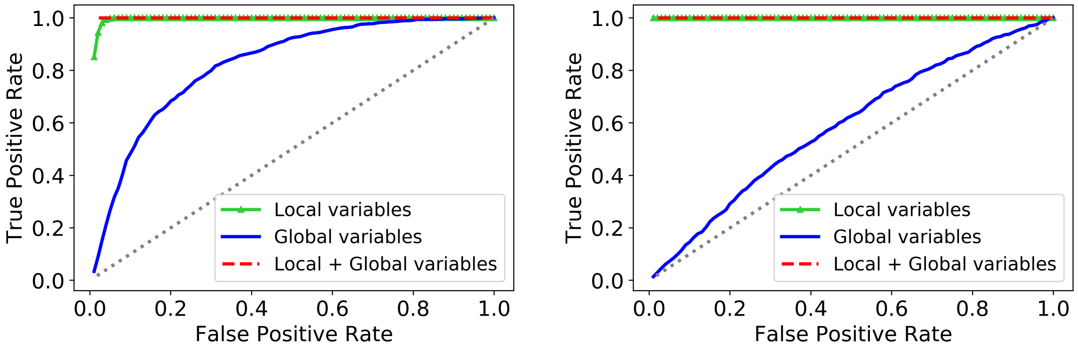

(a) Damage D1 10% severity

(b) Damage D2 10% severity

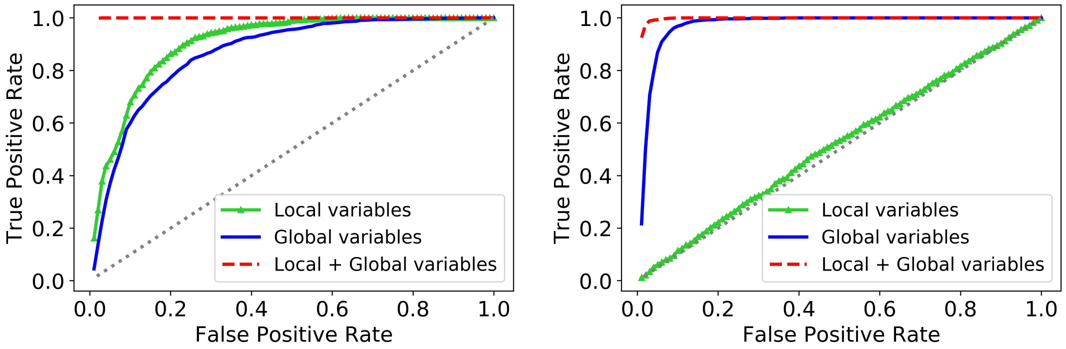

(c) Damage D3 10% severity

(d) Damage D4 10% severity

Figure 2.27: ROC curves for damage severity 10%

mainly affect the corresponding local variables, and the autoencoder will reconstruct these variables more deficiently. Hence, the highest contribution to the reconstruction error would result from variables measured with the sensors located nearby the damaged region. Here, analyze the reconstruction error of local variables is analyzed using the combined autoencoder ($DNN_{Combined}$). For a particular (randomly chosen) observation in the damaged testing datasets, the individual reconstruction error of the local variables is obtained using equation (2.10). The contribution to the reconstruction error (%) is calculated at each instrumented section and results are compared. Tables 2.10 to 2.13 gather the reconstruction error at each section for each of the considered damage scenarios. When the instrumented section contains more than one local variable, the average value of the involved variables is computed. For damage scenarios D1 to D3, the error values corresponding to the instrumented section nearby the damage (see figure 2.23) are highlighted in bold.

Results demonstrate that damage D1 to D3, which occur nearby the positions where local variables are recorded, are adequately located even for reduced sever-

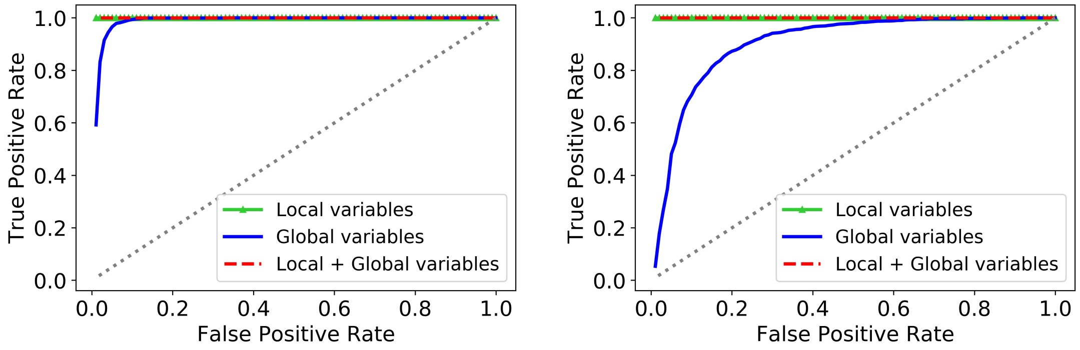

(a) Damage D1 20% severity

(b) Damage D2 20% severity

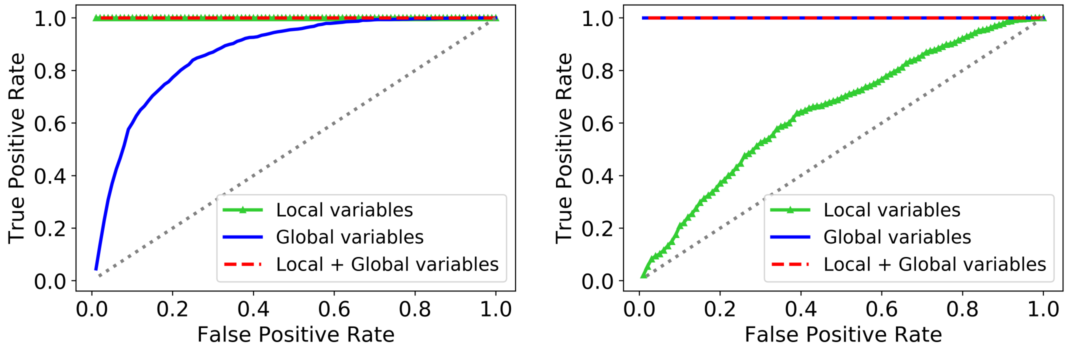

(c) Damage D3 20% severity

(d) Damage D4 20% severity

Figure 2.28: ROC curves for damage severity 20%

Table 2.10: Contributions to reconstruction error for D1

Instrumented section	**Severity level**		
	5%	**10%**	**20%**
S_1	**16.44**	**22.48**	**30.77**
S_2	0.09	0.16	0.32
S_3	1.55	0.96	1.05
S_4	1.38	1.58	1.70
S_5	0.60	0.86	0.99
S_6	3.44	6.78	0.03

ity levels (see Tables 2.10 to 2.12). The contribution of the affected section is considerably higher than those of the rest of the instrumented sections. By contrast, local variables are unable to inform about the location of D4, since no local variables are recorded close to it. This means that local variables only aid to

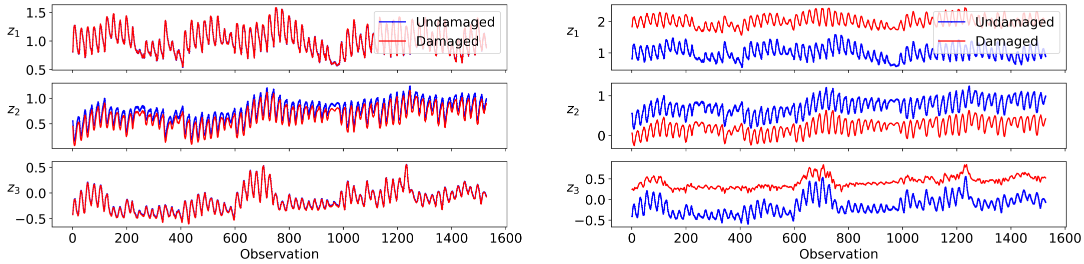

(a) Damage D1 with 10% severity (b) Damage D2 with 10% severity

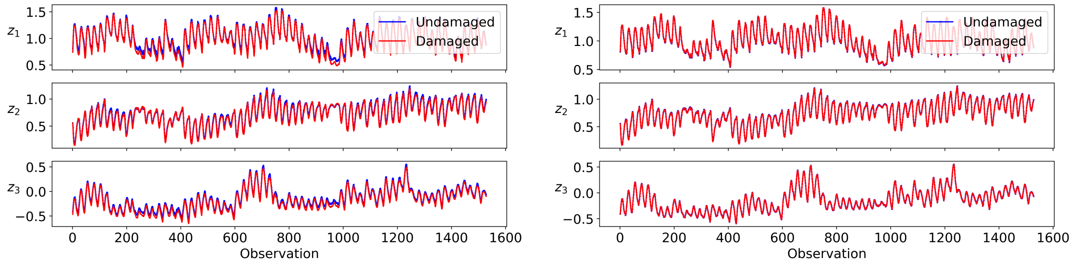

(c) Damage D3 with 10% severity (d) Damage D4 with 10% severity

Figure 2.29: Comparison of the healthy and damaged 3-dimensional latent space for DNN_{Local}

Table 2.11: Contributions to reconstruction error for D2

Instrumented section	**Severity level**		
	5%	**10%**	**20%**
S_1	0.08	0.00	0.09
S_2	0.00	0.10	0.08
S_3	**18.96**	**24.57**	**23.03**
S_4	8.53	2.96	1.75
S_5	0.25	0.40	0.27
S_6	1.07	0.11	1.19

locate damage occurring close to their emplacement.

2.8.2 SHM strategy

The final goal of the methodology is to detect abnormal behavior of Infante Dom Henrique bridge during operation from experimental monitoring data. The combination of local and global variables is employed as the input data and the corresponding DNN ($DNN_{Combined}$) developed and trained in Section 2.8 is considered.

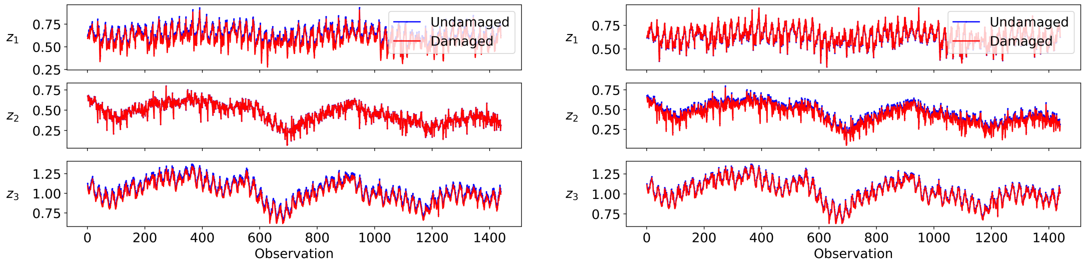

(a) Damage D1 with 10% severity (b) Damage D2 with 10% severity

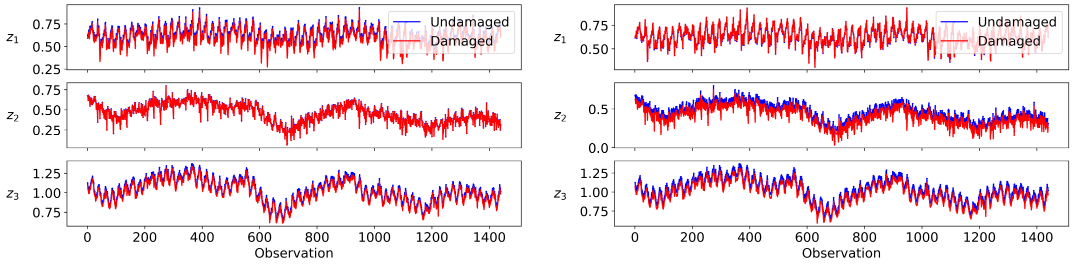

(c) Damage D3 with 10% severity (d) Damage D4 with 10% severity

Figure 2.30: Comparison of the healthy and damaged 3-dimensional latent space for DNN_{Global}

Table 2.12: Contributions to reconstruction error for D3

Instrumented section	**Severity level** **5%**	 **10%**	 **20%**
S_1	0.07	0.33	0.72
S_2	0.24	0.60	0.90
S_3	3.51	2.47	1.74
S_4	2.00	3.06	3.76
S_5	0.68	0.38	0.21
S_6	**33.21**	**43.90**	**51.29**

The damage detection strategy employs control charts of the reconstruction error [76] to produce an alert system that early detects structural damage.

Here, the cumulative error after five measurements is employed to reduce the risk of occurrence of false positives and produce a more robust alert system [87]. This means that the detection time is five hours, since the monitoring system provides one observation per hour including the measurements of the local and global variables. The threshold value α for the reconstruction error is established at the 97-percentile of the training dataset to obtain an adequate trade-off between the

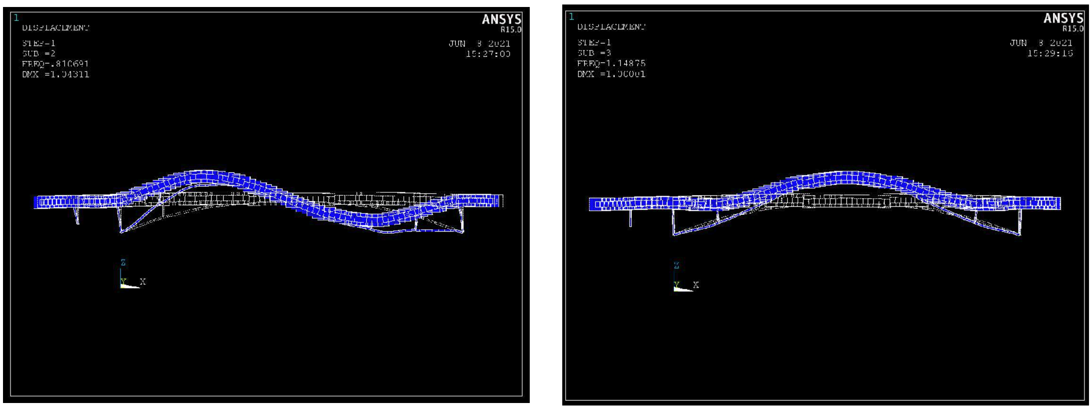

(a) First vertical eigenmode (b) Second vertical eigenmode

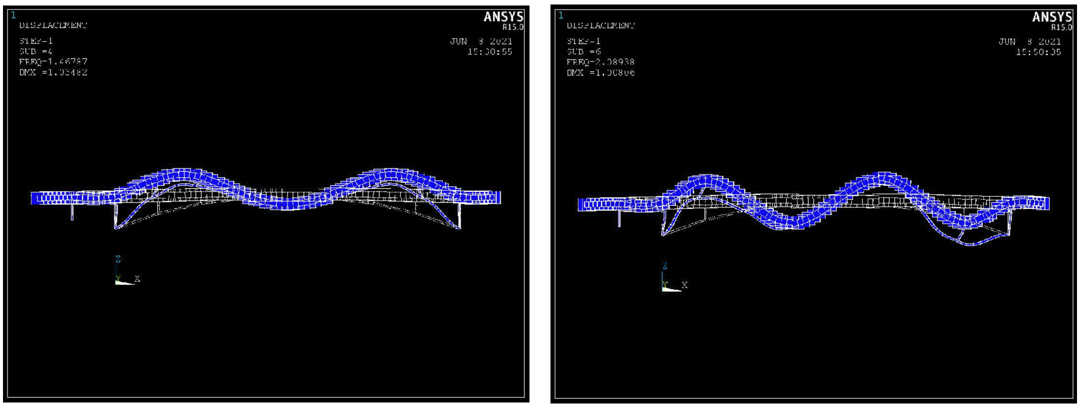

(c) Third vertical eigenmode (d) Fourth vertical eigenmode

Figure 2.31: Vertical bending eigenmodes

number of false positives and false negatives. Five testing subsets are concatenated: healthy, damage D1, damage D2, damage D3, and damage D4. The four damage scenarios are considered with a severity level of 10%. Figure 2.33 shows the control chart of the reconstruction error. The logarithmic scale is applied to the reconstruction errors to better visualize the results. The grey-shadowed region indicates the part of the testing with damage, and the vertical dashed lines delimit the subset associated with each damage. Measurements exceeding the threshold value (blue horizontal line) are red-coloured, and those below the threshold are green-coloured.

The figure shows that the four damage scenarios are adequately detected. In the case of damage D2, since three strain gauges exist at the affected region, the reconstruction error is very sensitive and robustly detects it. This means that lighter damage occurring at that location will be successfully detected. Figure 2.26 and 2.32b already revealed this sensitivity. Damage scenarios D1 and D3,

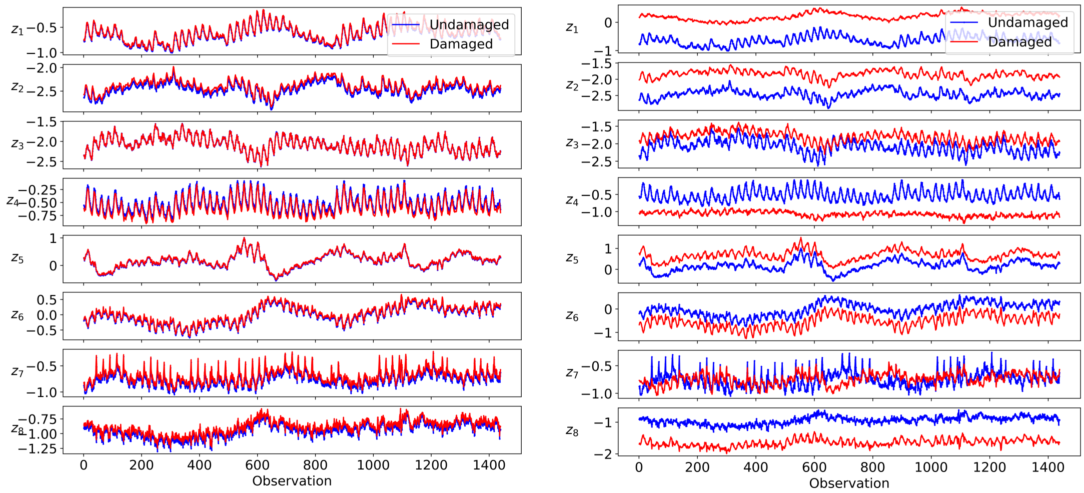

(a) Damage D1 with 10% severity (b) Damage D2 with 10% severity

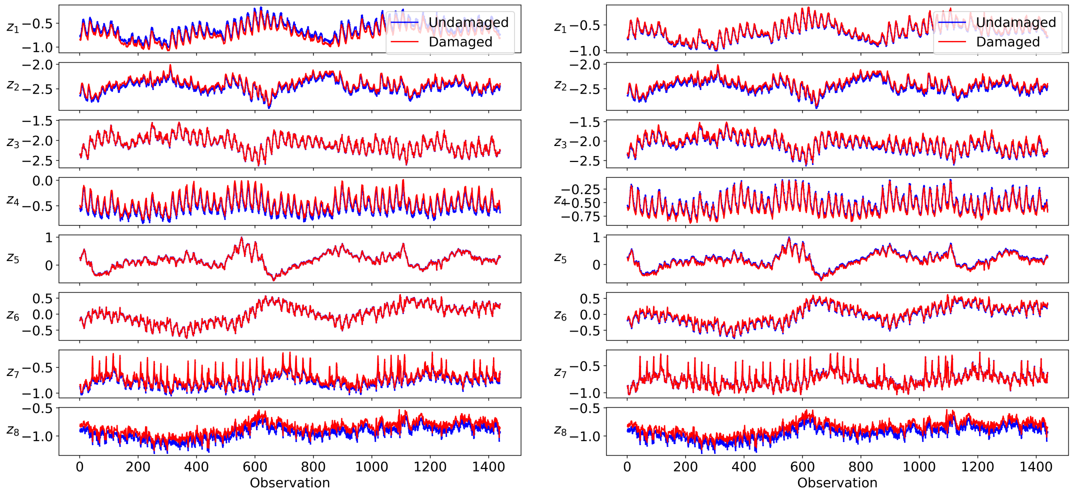

(c) Damage D3 with 10% severity (d) Damage D4 with 10% severity

Figure 2.32: Comparison of the healthy and damaged 8-dimensional latent space for $DNN_{Combined}$

which occur close to inclinometers, are adequately detected with some slack for lighter severity levels, specially damage D1, where two sensors participate. On the other hand, when analyzing damage D4, some false negatives are attained, which indicate that lower severity levels will be more difficult to detect. Hence, when only global variables participate since no local variables exist nearby the damage, the minimum detectable severity is 10%.

Table 2.13: Contributions to reconstruction error for D4

Instrumented section	**Severity level** **5%**	 **10%**	 **20%**
S_1	3.52	1.65	0.16
S_2	0.73	0.36	0.01
S_3	3.44	1.70	0.54
S_4	3.79	1.15	0.20
S_5	4.36	1.58	1.62
S_6	0.21	0.16	0.10

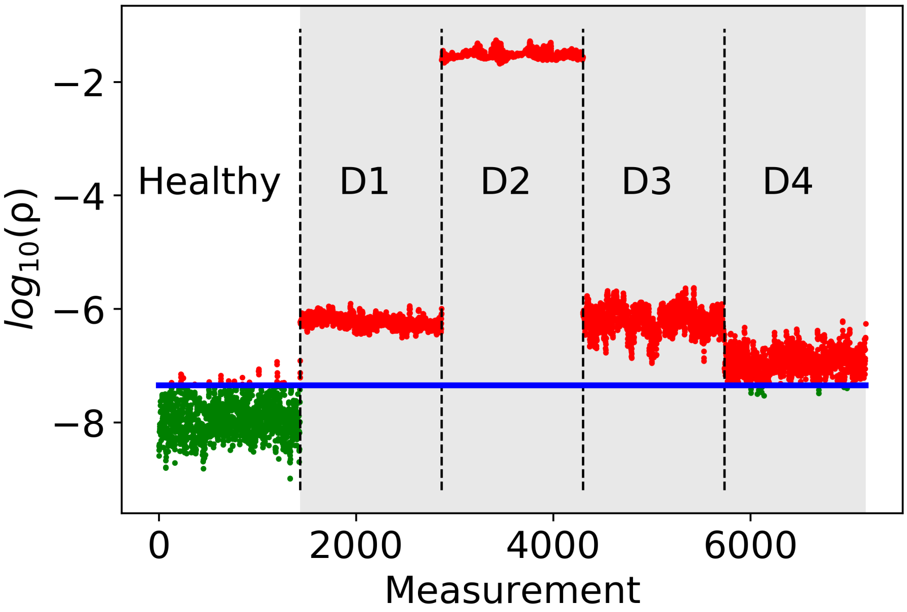

Figure 2.33: Testing control chart with damage severity of 10%

3 Combined model-based and data-driven approach

3.1 Introduction

In this section we address a supervised Deep Learning approach for damage identification in bridge structures. We employ a hybrid methodology that incorporates FE simulations to enrich the training phase of a Deep Neural Network with synthetic damage scenarios. The methodology intends to contribute to the progress towards the applicability of SHM practices in full-scale bridge structures. The goal is to broadly determine the location of the damage and to estimate its severity level. This diagnostic enables performing more exhaustive identification strategies (e.g., ultrasonic waves) in a reduced space, which would be unfeasible otherwise. The damage we seek to detect corresponds to any material degradation that affects wide areas of the structure by reducing its stiffness properties. Our method allows a feasible adaptation to large systems with complex parametrizations and structural particularities.

We investigate the performance of the proposed method on two full-scale instrumented bridges, obtaining adequate results for the testing datasets even in presence of measurement uncertainty. Besides, the method successfully predicts the damage condition for two real damage scenarios of increasing severity available in one of the bridges.

3.2 Problem description

In this work, we propose a supervised learning approach for damage identification in bridge structures. For a certain bridge B, we consider the dynamic response of the structure in the form of eigenfrequencies and eigenmodes:

$$\mathbf{u}_B = \{\mathbf{f}_B, \mathbf{\Phi}_B\}, \tag{3.1}$$

where $\mathbf{f}_B \in \mathbb{R}^{n_m}$ includes n_m eigenfrequencies and $\boldsymbol{\phi}_B \in \mathbb{R}^{n_o} \times \mathbb{R}^{n_m}$ contains the corresponding n_o-dimensional eigenmodes. We define the bridge condition by the location and severity of damage: $D_B = \{L_B, S_B\}$. Here, $L_B \in [1, 2, ..., n_z]$

indicates the location of damage among n_z zones in the bridge. Depending on the bridge type, these zones can be portions of the spans along the deck, or refer to elements with a particular structural function, such as regions near piers or abutments. The damage severity $S_B \in [s_{min}, s_{max}]$ indicates the extent of damage. Damages below s_{min} are considered negligible and damages above s_{max} are unlikely to occur before an action is taken. As described in Section 3.1, the damage identification problem consists of finding the characteristics of damage from measurements of the bridge response:

$$D_B = \mathcal{I}(\mathbf{u}_B), \tag{3.2}$$

where $\mathcal{I}$ is the inverse operator (see Figure 1.1).

We need training data covering the target damage states to approximate the inverse problem via Deep Learning. In full-scale operative bridges, it is unfeasible to recreate damage scenarios. Hence, monitoring data correspond only to the healthy or normal condition. We overcome this lack by employing a computational parametrization of the bridge, $B_{\boldsymbol{\theta}}$. The parametrization $B_{\boldsymbol{\theta}}$ substitutes the bridge B in the generation of damaged data.

We propose a combined methodology that employs Computational Mechanics fos solving damage scenario simulations and Deep Learning for rapidly assessing the health condition. The methodology is structured as follows: (*i*) we build a computational parametrization to approximate B; (*ii*) we update the values of the parametrization to match a measured response during normal operation; (*iii*) we establish a relationship between the parametrization values and the characteristics of damage; (*iv*) we generate a database of damage scenarios with different locations and severity levels; finally, (*v*) we build a DNN to approximate $\mathcal{I}$ with small error and predict damage in B from dynamic monitoring data.

3.3 Bridge parametrization

Let $B_{\boldsymbol{\theta}} = \{\boldsymbol{\theta}_1, ..., \boldsymbol{\theta}_{n_z}\}$ be a parametrization that represents B with n_z different zones. The number of zones to locate damage depends on the density of sensors in the monitoring system of B.

The parametrization includes elastic material properties, cross-section areas, and spring stiffness constants to describe boundary conditions. Each zone in $B_{\boldsymbol{\theta}}$ is described by a subset of properties $\boldsymbol{\theta}_i = \{\theta_1, ..., \theta_{n_{\theta_i}}\}$. We employ a Finite Element solver $\mathcal{F}^{FE}$ to produce the dynamic response of the parametrization:

$$\mathbf{u}_{B_{\boldsymbol{\theta}}} = \mathcal{F}^{FE}(B_{\theta}), \tag{3.3}$$

where $\mathbf{u}_{B_{\boldsymbol{\theta}}} = \{\mathbf{f}_{B_{\boldsymbol{\theta}}}, \boldsymbol{\phi}_{B_{\boldsymbol{\theta}}}\}$ contains the eigenfrequencies and eigenmodes of the parametrization. For simplicity in notation, we refer to $\mathcal{F}^{FE}$ as $\mathcal{F}$ since we consider negligible the difference between both operators.

3.3.1 Update the values of the parametrization for the healthy state

Under normal operating conditions, we assume the bridge is healthy and has a dynamic response $\mathbf{u}^h_B$. In large-scale structures, we often measure $\mathbf{u}^h_B$ through a short-term ambient vibration test with some inherent error: $\mathbf{m}^h_B = \mathbf{u}^h_B + \epsilon$. We subsequently obtain the dynamic properties using OMA techniques, yielding $\mathbf{m}'^h_B = \{\mathbf{f}^h_B, \boldsymbol{\phi}^h_B\}$ [118, 88]. For simplicity in notation, we remove the tilde and refer to the OMA-processed response as $\mathbf{m}^h_B$. Using short-term monitoring data for the updating process is a deterministic method that lacks consideration of environmental and operational variability. This approach poses a limitation to the methodology. When long-term monitoring data are avaialable, it is possible to incorporate EOC variations and achieve better characterization of the healthy state. We might address this problem using bayesian updating techniques [57], or with the methodology described in Chapter 4.

We set the initial parametrization values to $B_{\boldsymbol{\theta}} = B_{\boldsymbol{\theta}_0}$ based on design properties and engineering knowledge. This solution yields the preliminary numerical response as $\mathbf{u}_{B_{\boldsymbol{\theta}_0}} = \mathcal{F}(B_{\boldsymbol{\theta}_0})$. However, the true material properties (e.g., the elastic modulus of concrete or steel) in B are uncertain, and modeling the boundary conditions (such as piers or abutments) requires some simplifying decisions. Due to these assumptions and simplifications, there exist discrepancies between the true and the parametrization responses. We reduce this difference by updating the uncertain parameter values to match the healthy measured response. The resulting parametrization $B^*_{\boldsymbol{\theta}}$ makes $\mathbf{u}_{B^*_{\boldsymbol{\theta}}}$ approximate $\mathbf{m}^h_B$ with small error. We formulate this inverse problem as a minimization in the l_2 norm:

$$B^*_{\boldsymbol{\theta}} := \underset{B_{\boldsymbol{\theta}}}{\arg\min} \, \|\mathcal{F}(B_{\boldsymbol{\theta}}) - \mathbf{m}^h_B\|_2. \tag{3.4}$$

The variation intervals of the parameters contained in $B_{\boldsymbol{\theta}}$ must ensure consistency in the structural sense to represent a healthy condition after the updating. Hence, $B^*_{\boldsymbol{\theta}} = \{\boldsymbol{\theta}^*_1, \boldsymbol{\theta}^*_2, ..., \boldsymbol{\theta}^*_{n_z}\}$ yields the values of material properties and boundary conditions that adequately represent the healthy state of B.

3.4 Damage characterization

In this step, we establish the relationship $\mathcal{G}$ between the structural properties of the bridge B_θ and its damage condition $D_{B_{\boldsymbol{\theta}}} = \{L_{B_{\boldsymbol{\theta}}}, S_{B_{\boldsymbol{\theta}}}\}$. We assume that only one of the n_z zones experiments damage at a given time. Thus, when damage occurs at the i-th zone, the location is given by $L_{B_{\boldsymbol{\theta}}} = i$. We define the damage severity as:

$$S_{B_{\boldsymbol{\theta}}} = \mathcal{G}(\boldsymbol{\theta}_i) = \sqrt{\frac{1}{n_{\theta_i}} \sum_{j=1}^{n_{\theta_i}} {s_{i,j}}^2}, \tag{3.5}$$

where $s_{i,j}$ are the individual severity values for each involved property, described next. We apply a reduction vector $\boldsymbol{\beta}_i \in [\mathbf{lb}_i, 1]^{n_{\theta_i}}$ that affects the structural properties such that $\boldsymbol{\theta}_i^d = \boldsymbol{\beta}_i \boldsymbol{\theta}_i^*$. The lower bounds $\mathbf{lb}_i \in \mathbb{R}^{n_{\theta_i}}$ contain the maximum admissible reduction value for each property in $\boldsymbol{\theta}_i$ based on engineering knowledge to ensure structural sense. The remaining subsets of properties $\boldsymbol{\theta}_j$ $(j \neq i)$ keep their undamaged value in $B^*_{\boldsymbol{\theta}}$. Thus, the parametrization for a certain damage scenario at the i-th zone is $B^d_{\boldsymbol{\theta}} = \{\boldsymbol{\theta}_1^*, ..., \boldsymbol{\theta}_i^d, ..., \boldsymbol{\theta}_{n_z}^*\}$.

The relationship between the severity and the reduction factor depends on the type of structural property, which can be material or section properties (type a), and/or boundary conditions (type b). We establish this distinction because the dynamic response varies differently with changes in properties from each group. For type a, the value of the reduction factor is directly obtained as:

$$s_{i,j} = 1 - \beta i, j \qquad j = 1, .., n^a_{\theta_i}, \tag{3.6}$$

where $n^a_{\theta_i}$ is the number of a type properties at the i-th location. For type b, a different scale is employed to induce effective damage in the structure. In this case, the relationship between the reduction factor and its corresponding severity level is:

$$s_{i,j} = \frac{s_{max}}{\log_{10}(lb_{i,j})} \log_{10}(\beta i, j) \qquad j = 1, ..., n^b_{\theta_i}, \tag{3.7}$$

with $n^b_{\boldsymbol{\theta}_i} = n_{\boldsymbol{\theta}_i} - n^a_{\theta_i}$ and $lb_{i,j}$ being the $j - th$ element in the lower bound vector $\mathbf{lb}_i$.

3.5 Synthetic database generation

A synthetic database is generated that contains damage scenarios of different severity at each location. While location is a discrete variable that takes values between 1 and n_z, severity is a continuous variable. To uniformly sweep the severity interval, we build an iterative process to create different scenarios.

For each sample at the i-th zone, an initial sampling generates the value of S_{B_θ} from a uniform distribution: $S_{B_\theta} \sim U(s_{min}, s_{max})$. This is the target value to achieve with the individual severity values of each property at the damaged location using equation 3.6. We first generate random values for each individual property as: $\bar{s}_{i,j} = rand(U(0, s_{max}))$, with $j = 1, ..., n_{\theta_i}$. We calculate the severity level $\bar{S}$ by replacing $\bar{s}_{i,j}$ in equation (2.13). We then correct the individual severity values to produce S, using the following expression:

$$\mathbf{s}_i = \frac{S}{\bar{S}}\bar{\mathbf{s}}_i \tag{3.8}$$

The reduction vector $\boldsymbol{\beta}_i$ is subsequently obtained from eqs. 3.5 and 3.6. If any element in $\boldsymbol{\beta}_i$ lies out of the admissible interval $[\mathbf{l}_i, 1)$, we generate a new random set of individual severity values $\bar{\mathbf{s}}_i$ and recalculate $\boldsymbol{\beta}_i$. We iteratively repeat this step until we achieve a correct set of reduction factors. We finally obtain the damaged properties as $\boldsymbol{\theta}_i^d = \boldsymbol{\beta}_i \boldsymbol{\theta}_i^*$. The damaged bridge is given by $B_{\boldsymbol{\theta}}^d = \{\boldsymbol{\theta}_1^*, ..., \boldsymbol{\theta}_i^d, ..., \boldsymbol{\theta}_{n_z}^*\}$. Algorithm 2 describes this iterative procedure to obtain valid damage scenarios with uniformly distributed severity ($L_{B_\theta} = i$).

Algorithm 2 is applied to obtain n damage scenarios for each structural region $i = 1, ..., n_z$. This results in $N = n_z \times n$ samples conforming the database. The corresponding dynamic responses are calculated by solving:

$$\mathbf{u}_{B_{\boldsymbol{\theta}}}^{(k)} = \mathcal{F}\left(B_{\boldsymbol{\theta}}^{d_k}\right) \qquad k = 1, ..., N \tag{3.9}$$

The k-th sample in the database contains the dynamic response $\mathbf{u}_{B_{\boldsymbol{\theta}}}^{(k)} = \{\mathbf{f}_{B_{\boldsymbol{\theta}}}^{(k)}, \boldsymbol{\phi}_{B_{\boldsymbol{\theta}}}^{(k)}\}$ and the corresponding damage condition of the bridge $D_{B_{\boldsymbol{\theta}}}^{(k)} = \{L_{B_{\boldsymbol{\theta}}}^{(k)}, S_{B_{\boldsymbol{\theta}}}^{(k)}\}$.

Algorithm 2: Generation of damaged scenarios with uniform severity

```
Input: $\boldsymbol{\theta}^*$, $s_{min}$, $s_{max}$, $\boldsymbol{lb}_i$, $n_{\theta_i}$, $a$, $b$
Output: $B^d_\theta$, $S_{B_{\boldsymbol{\theta}}}$
/*                                                                  */
/* Part I: Initialization                                           */
$S_{B_{\boldsymbol{\theta}}} \leftarrow rand(\mathcal{U}(s_{min}, s_{max}))$ ;    // Obtain posterior severity value
$B^d_{\boldsymbol{\theta}} \leftarrow B^*_{\boldsymbol{\theta}}$ ;                // Initialize the damaged parametrization
$\beta i, j \leftarrow 0, \quad j = 1, ..., n_{\theta_i}$ ;      // Initialize reduction vector $\boldsymbol{\beta}_i$
/*                                                                  */
/* Part II: Obtain a damaged parametrization $\boldsymbol{\theta}^d$              */
while $any\ (\beta i, j < lb_{i,j} \quad or \quad \beta i, j > 1 \quad j = 1, ..., n_{\theta_i})$ do
    for $j \leftarrow 1$ to $n_{\theta_i}$ by 1 do
        $\bar{s}_{i,j} \leftarrow rand(\mathcal{U}(0, s_{max}))$ ;            // Obtain the preliminary
         individual severity values $\bar{\mathrm{s}}_i$
    Obtain $\bar{S}$ from eq. (3.7). ;            // Calculate the preliminary
     severity $\bar{S}$
    Obtain $\mathbf{s}_i$ from eq. (3.8);            // Obtain the severity values
    /* Calculate the reduction vector $\boldsymbol{\beta}_i$                          */
    for $j \leftarrow 1$ to $n_{\theta_i}$ by 1 do
        if $property\ type = a$ then
            Calculate $\beta_{i,j}$ from eq. (3.5)
        if $property\ type = b$ then
            Calculate $\beta_{i,j}$ from eq. (3.6)
/* Part III: Obtain the damaged bridge $B^d_{\boldsymbol{\theta}}$                   */
$\boldsymbol{\theta}^d_i \leftarrow \boldsymbol{\beta}_i \boldsymbol{\theta}^*_i$ ;   // Calculate the subset of damaged properties $\boldsymbol{\theta}^d_i$
$B^d_{\boldsymbol{\theta}} \leftarrow \{\boldsymbol{\theta}^*_1, ..., \boldsymbol{\theta}^d_i, ...., \boldsymbol{\theta}^*_{n_z}\}$;           // Build the damaged bridge
 parametrization
Return $\{B^d_{\boldsymbol{\theta}}, S_{B_{\boldsymbol{\theta}}}\}$
```

3.6 Deep Neural Network

The final goal of the proposed methodology is to identify the damage state of the bridge from measurements of its dynamic response. The operator $\mathcal{I}$ (see Figure 1.1) introduced in Section 3.2 establishes the relationship between the dynamic response $\mathbf{u}_B$ (input) and the damage characteristics D_B (output). The dimension of the input layer v depends on the number of mode shapes (n_m) and available observation points or sensors (n_o) that describe the dynamic response of the bridge, being: $v = n_m(n_o + 1)$. Let $\mathcal{I}_\gamma$ be a DNN that approximates the inverse operation of damage identification $\mathcal{I}$:

$$D_{B_{\boldsymbol{\theta}}} \approx \mathcal{I}_\gamma(\mathbf{u}_{B_{\boldsymbol{\theta}}}; \boldsymbol{\gamma}), \tag{3.10}$$

where $\boldsymbol{\gamma}$ includes the parameters of the DNN.

Step 1: Pre-processing:

Due to the disparity between the two output variables (location and damage severity) in D_B, we apply a linear rescaling into the interval $[0.5, 1.5]$. This interval is selected as it is of unit length and ensures correspondence between relative and absolute errors [123]. For a certain variable $\mathbf{x}$, let $x_{min} := min(\mathbf{x})$ and $x_{max} := max(\mathbf{x})$. The rescaling function $\mathcal{R}$ is defined as:

$$\mathcal{R}(\mathbf{x}) = \frac{\mathbf{x} - x_{min}}{x_{max} - x_{min}} + 0.5 \tag{3.11}$$

Thus, the rescaled damage condition is obtained as $D_B^{resc} = \mathcal{R}(D_B)$. For simplicity in notation, in the following, the rescaled health condition D_B^{resc} is referred to as D_B. The same holds for the parametrization ($D_{B_{\boldsymbol{\theta}}}^{resc}$).

Step 2: Loss function: The discrepancy between the predicted damage condition $\mathcal{I}_\gamma(\mathbf{u}_B)$ and the real state D_B is measured employing the l_2 norm of the following loss function:

$$\mathcal{L}_\gamma = \|\mathcal{I}_\gamma(\mathbf{u}_B) - D_B\|_2 \tag{3.12}$$

Step 3: Network architecture: A particular NN architecture based on autoencoders [17] is proposed in this work. Autoencoders perform an encoding step to compress the input into a lower-dimensional vector and subsequently decompress it (decoding step) to recover most of the original information [68]. Here, we rely on autoencoder approaches but substitute the decoding step by a mapping between the encoded input and the structural damage (location and severity).

The architecture contains two connected modules. The first module solves the encoding task of data compression. The second module finds a relationship between the compressed input and the damage characteristics. As described in Section 2.4, each module is created by adding a linear and a nonlinear term. With this architecture, when the addressed problem is straightforward and nonlinearities have a small contribution, the nonlinear blocks can be deactivated. Figure 3.1 describes our proposed network topology.

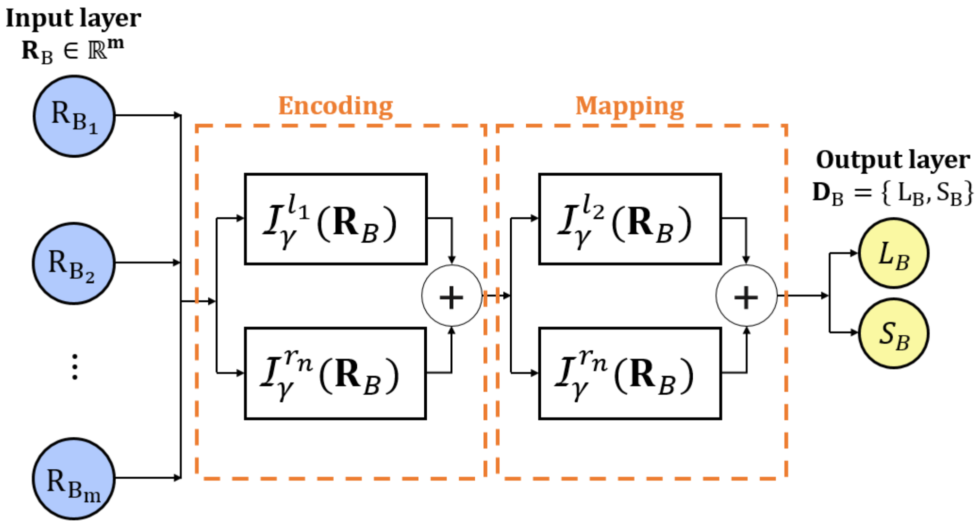

Figure 3.1: Block diagram of our proposed Neural Network

For the first module, we have: $\mathcal{I}_\gamma^1 = \mathcal{I}_\gamma^{l_1} + \mathcal{I}_\gamma^{n_1}$. The linear branch $\mathcal{I}_\gamma^{l_1}(\mathbf{u}_B; \gamma_{l_1})$ applies an affine transformation to the input layer through one single dense layer. γ_{l_1} contains the weights and bias parameters of the operation. The nonlinear branch $\mathcal{I}_\gamma^{n_1}(\mathbf{u}_B; \gamma_{n_1})$ undergoes a feed-forward architecture [59] that applies a linear transformation followed by a nonlinear activation function g through L_{n_1} layers. The parameter vector γ_{n_1} includes the weights and bias of the operation. The output of the first module enters a second module with analogous architecture that performs the feature mapping. The output layer adds the linear and the nonlinear connections of the second module: $\mathcal{I}_\gamma^{l_2}(\mathcal{I}_\gamma^1; \gamma_{l_2}) + \mathcal{I}_\gamma^{n_2}(\mathcal{I}_\gamma^1; \gamma_{n_2})$. This layer is customized to restrict the output variables to the admissible rescaled interval. Let $\mathcal{C}$ be the clipping function into the interval $[0.5, 1.5]$:

$$\mathcal{C}(x; 0.5, 1.5) = \begin{cases} 0.5 & if \quad x < 0.5 \\ x & if \quad 0.5 \leqslant x \leqslant 1.5 \\ 1.5 & if \quad x > 1.5 \end{cases} \tag{3.13}$$

The last step is to undo the rescaling operation in equation (3.11) to obtain the real values of the output variables.

Step 4: Training: We employ the database generated in section 3.5 to train the DNN ($\mathcal{I}_\gamma$) and obtain the set of optimal parameters γ^* that produces an adequate approximation to $\mathcal{I}$:

$$\gamma^* := \arg\min_{\gamma}(\mathcal{L}_\gamma) \tag{3.14}$$

Here, we employ an stochastic gradient descent method to solve the minimization problem [59]. We employ Tensorflow library available in Python environment to carry out the whole process [1].

3.7 SHM strategy: damage location and severity estimation

The final goal is to employ the DNN to evaluate new measured data from the monitoring systems operating in bridge structures. Figure 2 shows a flowchart of the whole procedure. We can divide the different tasks into offline and online. The offline part includes the required steps to build the damage identification system. The online part consists of acquiring new measurements from the bridge to feed the DNN and obtain a health condition diagnostic.

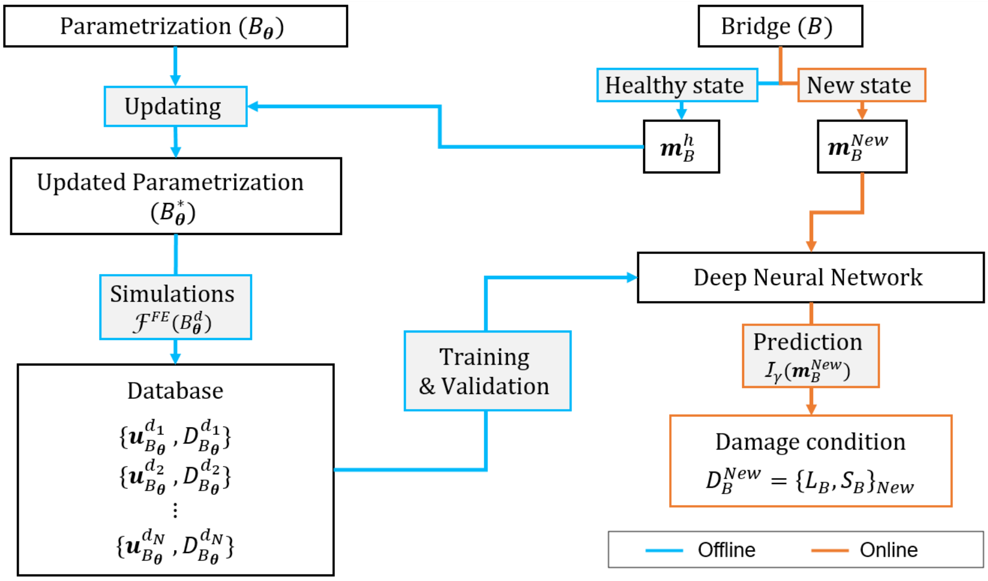

Figure 3.2: Flowchart of the proposed methodology

In this work, we focus on the development of the offline part. The online part incorporates the DNN as a close to real-time assessment tool for SHM. Once new measurements are acquired under an unknown structural condition, the DNN would provide a damage diagnostic. The prediction must be considered an assessment that complements visual inspections and other evaluation methods.

3.8 Numerical Results

In this section, we describe the results obtained for two case studies. The first one is the Infante Dom Henrique bridge in Porto. This bridge is currently under service and is being monitored. However, data regarding real damage scenarios are unavailable. We subsequently apply the proposed method to the Z24 bridge in Switzerland. This brings up the opportunity to perform an experimental test. To solve the different tasks, we employed a computer (Dell Precision 3520) with the following specifications: Intel(R) Core i7-7700HQ, 2.80 GHz CPU.

3.8.1 Case 1: Bridge Infante Dom Henrique

3.8.1.1 The bridge and monitoring system

The bridge Infante Dom Henrique was already described in Chapter 2. The monitoring system employed in this study is the dynamic one, introduced in Section 2.8 and fully described in [86]. In this work, we focus on the vertical accelerations of the bridge to locate and quantify the damage. We have access to four vertical acceleration signals (upstream or downstream) from which we calculate the dynamic properties (eigenfrequencies and eigenmodes) using OMA techniques [86]. Figure 3.3 shows the first four unity-scaled vertical mode shapes. While eigenfrequencies are global features, eigenmodes contribute to locating damage. A mode shape describes the vibration amplitude level for each node of the structure when it is excited with the corresponding eigenfrequency. The presence of damage at certain location will change the mode shape differently. If changes to bending stiffness are under investigation, each eigenmode is more sensitive to those damages occuring close to the regions where the curvature of the mode shape is larger. The number of points describing each eigenmode depends on the number of sensors in the monitoring system. Hence, the monitoring system restricts the zones where damage can be located to those that influence the modal ordinates of the instrumented degrees of freedom. In this work, we restrict the possible damaged regions to the instrumented half of the bridge. Although damages at regions on the left-hand side of the bridge might also be detected, it would be difficult to distinguish their location.

3.8.1.2 Ambient vibration test

An ambient vibration test is one of the most convenient approaches to estimate the modal parameters of a structure under service [86]. It employs the vibration induced by traffic and wind as the excitation to characterize the response of the structure. The amplitude of the accelerations that the bridge suffers under

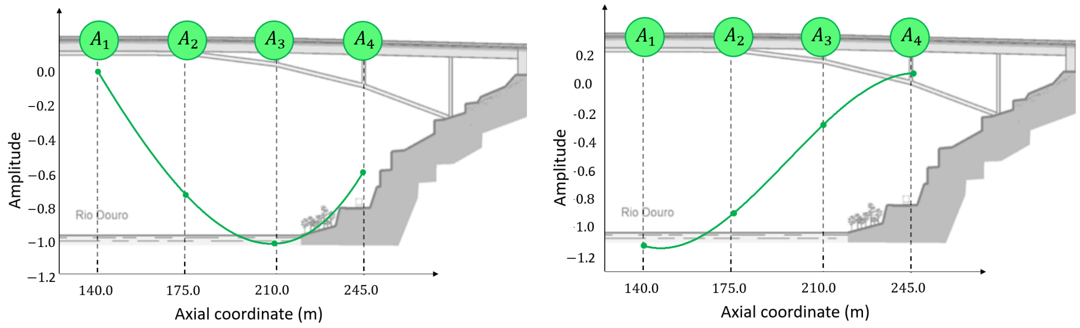

(a) First vertical eigenmode

(b) Second vertical eigenmode

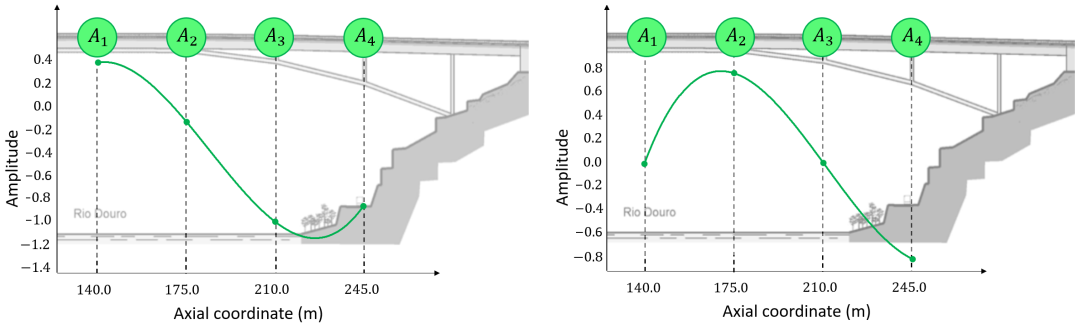

(c) Third vertical eigenmode

(d) Fourth vertical eigenmode

Figure 3.3: Vertical eigenmodes obtained from ambient vibration test

such excitation is very low. For this reason, especially sensitive sensors must be employed.

In the ambient vibration test carried out at Infante bridge in 2002, four triaxial 18-bit strong motion recorders were used [86]. All sensors were synchronized through external GPS sensors. During the test, two of the sensors were fixed in the middle-deck cross-section (upstream and downstream) and acted as a reference. The other two sensors changed position within a total of 15 set-ups to cover the length of the bridge deck. For each set-up, records of 16 minutes were collected with a sampling frequency of 100 Hz. This frequency was reduced to 20 Hz after the application of a low-pass filter. Further details regarding the ambient vibration test can be found in Magalhães et al. [86].

3.8.1.3 Parametrization

We employ a parametrization developed by Magalhães et al. [86]. It includes 3D bar elements in ANSYS® to describe the behavior of the bridge. The structural properties (area, bending and torsion moments of inertia, and shear deflection constants) are included according to design specifications. Since we are investigating the vertical bending response of the structure, 3D bar elements (beam type) have optimal functionality. They also allow introducing damage as a reduction of the corresponding cross-section inertial properties. This type of model was first developed by Magalhães et al.[86] and can be considered an accurate approximation to represent the vertical bending behavior of the bridge. More sophisticated models such as those composed of solid elements could be employed. These provide more precise predictions at the cost of higher computational effort and modeling complexity. But these models can introduce undesired mode shapes (e.g., vibrations of the cantilever eaves of the deck) and hinder the modal identification process. Besides, damage simulation in these models may become very complex since solid elements lack section properties as an accessible parameter. It forces to introduce damage in terms of geometrical variations, which is a non-trivial task that can produce mesh problems and prevents automatically generating scenarios.

Magalhães et al. [86] described the calibration process, focusing on the connections of columns and abutments with the deck. While the highest columns (corresponding to instrumented sections S_1 and S_6 in Figure 2.12) have a monolithic connection, the other columns and abutments contain two unidirectional sliding pot bearings. Three possible connection disposals were considered and analyzed. The authors designed a final parametrization including fixed longitudinal displacement and rotations in the pot bearings at the columns but free at the abutments, and horizontal springs to simulate additional stiffness at the abutments. The value of the stiffness constants in the abutments is fixed manually to approximate the first four vertical bending eigenmodes.

For further steps is this methodology, we employ the higher-order modes (third and fourth) since they are more sensitive to localized damages such as those sought in this work [92]. According to the position of the sensors, we consider eight possible damage locations along the right-hand side of the bridge, according to Figure 3.4. Each location is 17.5 m long along the bridge deck.

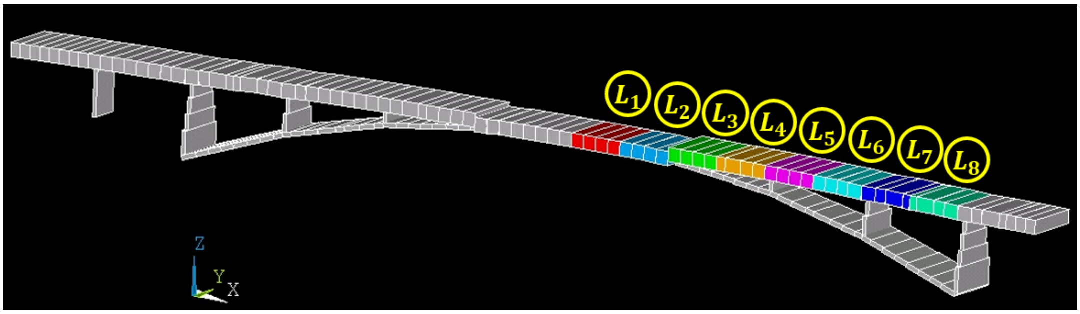

Figure 3.4: Parametrization of Infante bridge with eight locations

3.8.1.4 Database generation

Given the beam-type behavior of the bridge [86] and the location of the sensors in the monitoring system, we focus on the identification of damages in the deck. Specifically, we employ the real values that describe the cross-section inertia along with the beam-type elements that model the deck. All these structural properties are of type a introduced in Section 3.4. Each location contains 4 properties, resulting in a total of 32 structural properties involved in this case of study. We set the minimum severity to $s_{min} = 2.5\%$ and the maximum to $s_{max} = 50\%$ based on sensitivity analysis and engineering criterion. During sensitivity analysis, we observed that damages below 2.5% barely introduced changes in the response of the structure. The multiplication factors in $\boldsymbol{\beta}$ range from 0 (undamaged property) to 0.5 (50% damage at that property).

We solve $n = 5,000$ damage scenarios for each of the $n_z = 8$ locations, yielding a total of $N = 40,000$ samples. The time required to obtain the database was 37.3 hours. We calculate the dynamic response for each sample and match it with the corresponding damage label to form the database. Although only four measurement points (sensors) are available in the monitoring system, we obtain seven-dimensional eigenmodes from the simulations to add extra information. We complete the experimental eigenmodes by fitting an spline and obtaining the intermediate value in between every two sensors.

We choose some representative samples from the database to study the sensitivity of eigenfrequencies to damage. For each location, we select ten samples of constantly increasing severity from 5% to 50%. Figure 3.5 shows the sensitivity of the selected eigenfrequencies.

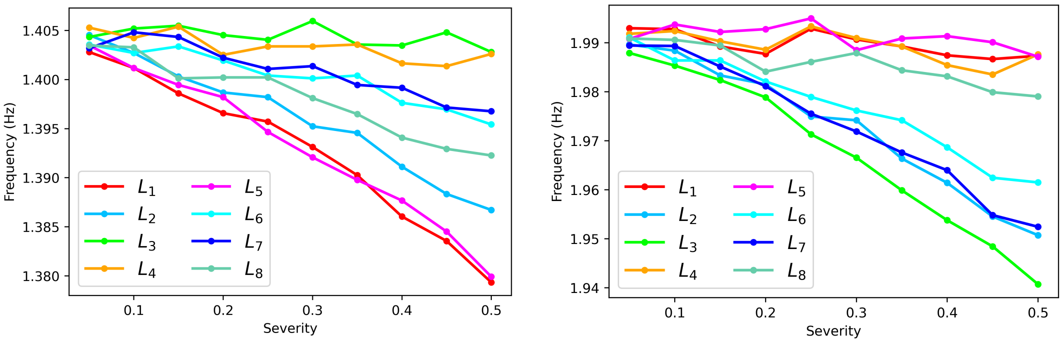

(a) Third vertical eigenfrequency

(b) Fourth vertical eigenfrequency

Figure 3.5: Evolution of eigenfrequencies with increasing damage severity

We observe that the third eigenfrequency is very sensitive to damages at locations L_1 and L_5. This is related to the curvature (change of slope) of the eigenmodes [113]. The higher the curvature of the mode in the affected location, the higher the impact on the corresponding natural frequency [113]. We observe that for location L_3, since it is almost a blind node (small curvature), it barely changes with the increase of severity (see Figure 3.3c). For the same reason, the fourth vertical eigenfrequency is strongly affected by damages at location L_3 (see Figure 3.3d).

3.8.1.5 Deep Neural Network

We employ the network architecture described in Section 3.6. The input layer receives a total of $v = 16$ features or variables. These include higher-order (third and fourth) vertical eigenfrequencies and eigenmodes, as indicated in subsection 3.8.1.3. The encoding phase compresses this input into an eight-dimensional feature vector. The nonlinear connections $\mathcal{I}_{\gamma}^{n_1}$ and $\mathcal{I}_{\gamma}^{n_2}$ are symmetric and contain five layers each. We employ a “ReLu” [59] activation function at the first four hidden layers. The fifth hidden layer applies a linear transformation. The output layer applies the clipping function $\mathcal{C}$ to yield the two-dimensional output in the rescaling interval. This topology provides adequate results.

We randomly split the database as follows: 72% of the samples are employed for training, 18% for validation, and the remaining 10% are kept for testing. We train the neural network through $10,000$ epochs. This number allows for sufficient training and prevents overfitting. Each epoch constitutes a new passage of the entire training dataset through the NN[59]. Figure 3.6 shows the evolution of the loss function for both the training and validation datasets. The required training time was 12 min. We employ a particular gradient descent optimizer that prevents getting trapped in local minima during training [74]. This optimizer produces high loss function values at certain epochs. To select an adequate solution, we retain the best trained model based on a performance indicator. Here, we select the model that achieves the minimum loss value for the validation dataset.

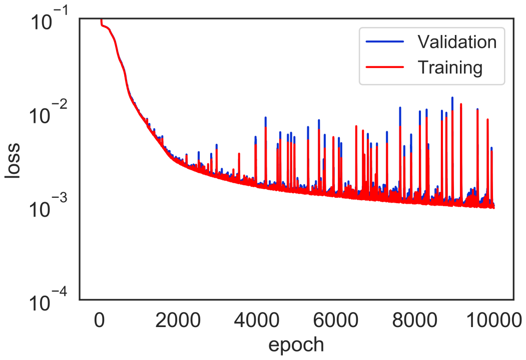

Figure 3.6: Loss evolution for the training and validation datasets (Infante bridge)

We evaluate the performance of the trained network for the testing dataset. Figure 3.7 displays the cross-plot of the output variables. It exhibits a high correlation between the real value (ground truth) and the prediction given by the DNN for both severity and location. We employ the squared correlation coefficient r^2 as the correlation metric [11]. The distribution of the samples in the graph is represented with a color scale, with a darker color meaning more density of samples.

Figure 3.7a shows the cross-plot of location for the testing dataset. Although the ground truth is restricted to the eight possible locations, the prediction of the DNN is continuous (regression). Most of the samples concentrate close to the red line (prediction = ground truth), resulting in a high correlation level (r^2). Figure 3.7b shows the predictions obtained for the severity variable. These results show a good performance of the DNN during the numerical test.

Given the lack of real measurements from damage scenarios, we perform a numerical test. We employ two damage cases described by Magalhães et al. [87]. These are considered minor damages according to [87]. They consist in reducing the vertical bending inertia at a small segment of the bridge deck. They affect locations L_1 and L_8 according to Figure 3.4. We consider two reduction levels -10% and 30%- for the damaged structural property. We estimate the ground truth severity for each scenario according to equations 3.5 and 3.6. Table 3.1 shows the prediction provided by the DNN.

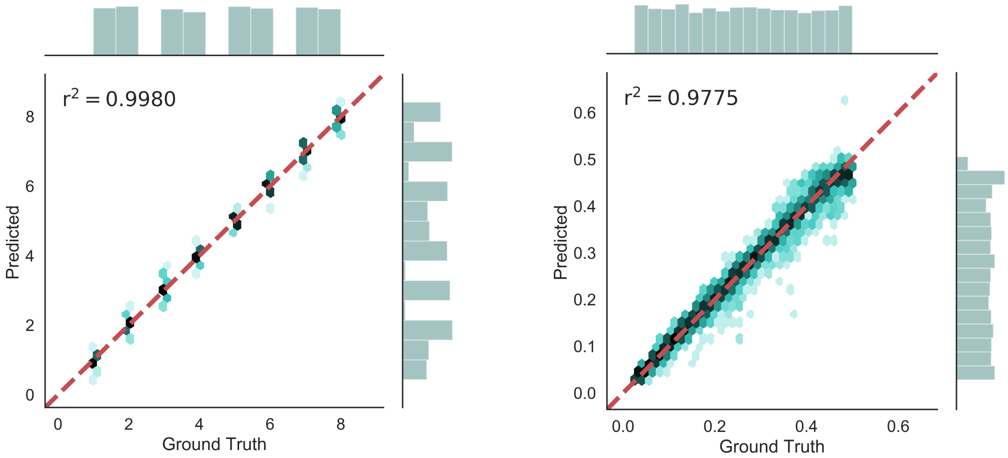

(a) Location cross-plot for the testing dataset (b) Severity cross-plot for the testing dataset

Figure 3.7: Infante bridge cross-plots for the testing dataset

Table 3.1: Numerical testing for Infante bridge.

Scenario	Ground truth		Prediction	
	Location	Severity (%)	Location	Severity (%)
10% stiffness reduction at L_1	1	5.00	1.41	4.21
30% stiffness reduction at L_1	1	15.00	1.05	13.42
10% stiffness reduction at L_8	8	5.00	7.89	5.32
30% stiffness reduction at L_8	8	15.00	8.00	17.85

According to Table 3.1, the DNN is achieving adequate results. However, the lack of experimental damage scenarios prevents a more realistic validation. After training and validation, the algorithm is ready to be implemented in the SHM system. The monitoring sensors will acquire new measurements and produce the current natural frequencies and mode shapes of the structure. To make the experimental eigenmodes (four-dimensional) match the numerical ones (seven-dimensional), we complete them by fitting a spline and obtaining the corresponding value between every two sensors. The completed experimental measurements are fed to the DNN that provides a prediction of the health condition of the structure.

To demonstrate the contribution with respect to other existing techniques, we consider the work developed by Pathirage et al. [100], which also employed an autoencoder trained with numerical simulations to solve the damage identification problem. The main difference lies in the output of the DNN. For Pathirage et al. [100], the output is an N-dimensional vector based on the N parameters (structural properties) that can change in presence of damage. N can be considerably large for large-scale structures with complex parametrizations. Besides, this approach requires to adapt the architecture to fit the number of properties of different structures or different parametrizations of the same structure. Our approach applies a post-processing to the structural parameters to make predictions based on a two-dimensional output that describes damage in terms of location and severity. This allows keeping the same architecture (with reduced output dimension) of the DNN regardless of the parametrization and structural system and enhances the interpretation of predictions. Also, the larger is the output (more variables to predict) the more complex gets the training phase and predictions may lose accuracy.

For the case of study of Infante Dom Henrique bridge, the output dimension increases from two to 32 if we employ the approach of Pathirage et al. [100]. We implement this by adapting our DNN to have a 32-dimensional output, where the output corresponds to the reduction vector $\boldsymbol{\beta}$. Table 3.2 compares the value of the r^2 metric that measures the correlation between ground truth and prediction of the output variables during testing for both methodologies. The predictions provided by our approach are better than those using the 32-dimensional one. Obtaining adequate results using that methodology would require a more complex DNN and a larger training database, which implies more computational effort. In addition, the results provided by our approach are easier to interpret and enhance applicability mainly for complex parametrizations with a large amount of involved structural properties.

Table 3.2: Comparison of metric r^2 value for the output variables during testing using a 2-D approach and a 32-D approach.

Output dimension	Variable						
	Var1	Var2	Var3	...	Var30	Var31	Var32
2-D	0.9980	0.9775	-	...	-	-	-
32-D	0.8591	0.7802	0.7345	...	0.7531	0.7771	0.8375

3.8.1.6 Incorporation of measurement uncertainty

In this section, we evaluate the performance of the methodology in presence of measurement noise and environmental variability. A long-term monitoring campaign started in 2007 at Infante bridge that contained 12 force balance accelerometers installed in four particular cross-sections of the structure [86, 87]. These measurements were subsequently processed to identify the eigenfrequencies and eigenmodes of the bridge.

Some statistical analyses were carried out by Magalhães et al. [86] to explore the variability induced by temperature and other operational phenomena (e.g., concrete hardening) in the eigenfrequencies of the bridge. Table 2 in their work [86] compared the Standard Deviation (SD) of the first twelve eigenfrequencies for the ambient vibration test and the monitoring campaign, observing much higher values during the monitoring phase due to the effect of temperature. According to their study, any eigenfrequency outranging the interval of its value $+/-1.5$SD could be considered an outlier. This information was unavailable for eigenmodes, but it is known that they are less sensitive to environmental variability [105].

Based on this information, we account for measurement noise and environmental variability as follows: for the eigenfrequencies, we consider the same interval as [86]. To be conservative, we employ the highest SD value amongst the four vertical eigenfrequencies analyzed. For the eigenmodes, we employ the variability observed during the ambient vibration test that includes measurement noise. We incorporate measurement error as an additive term [126] such that:

$$m_{B_{\boldsymbol{\theta}}} = u_{B_{\boldsymbol{\theta}}} + \epsilon, \tag{3.15}$$

where $u_{B_{\boldsymbol{\theta}}}$ refers to any response obtained from simulations (eigenfrequencies and eigenmode amplitudes), ϵ stands for the additive error term, and $m_{B_{\boldsymbol{\theta}}}$ is the resulting synthetic measurement.

The new database includes: (i) the original database described in Section 3.8.1.4, (ii) the original database affected by a reduced error level ($\epsilon \in [-0.0001, +0.0001]$), and (iii) the original database affected by the previously described measurement uncertainty according to [86]. The value of ϵ for each scenario is randomly sampled from the corresponding interval.

We repeat the training and validation process of the neural network for the new database. Figure 3.8 shows the loss evolution for the training and validation datasets. The required training time was 28 min.

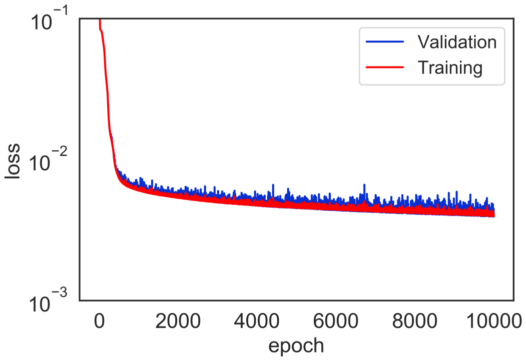

Figure 3.8: Loss evolution for the training and validation datasets with measurement uncertainty

We then evaluate the performance of the trained network for the testing dataset. Figure 3.9 includes the cross-plot of the output variables.

The achieved correlation levels are slightly lower than those obtained in the deterministic approach, but results are still great, demonstrating an adequate performance of the DNN. Table 3.3 shows the prediction provided by the DNN for the considered damage scenarios. We observe that the DNN achieves adequate results in predicting both damage scenarios. This example is a preliminary attempt to include measurement error in the process, but more extensive research is required to demonstrate the full capability of the method to operate under diverse noisy and variable environments. We consider this issue in Chapter 4.

3.8.2 Case study 2: Z24 bridge

The Z24 bridge is a post-tensioned concrete two-cell box girder with three spans crossing the highway that connects Bern and Zurich (see Figure 3.10). This bridge was demolished in 1998 to expand its span due to an enlargement of the highway [108]. Before demolition, some damage scenarios were generated and monitored during short-term campaigns for different research purposes [77, 110, 133, 76]. In this work, we employ two damage scenarios corresponding to a settlement of 40 mm and 80 mm at the Koppigen side pier (see Figure 3.10).

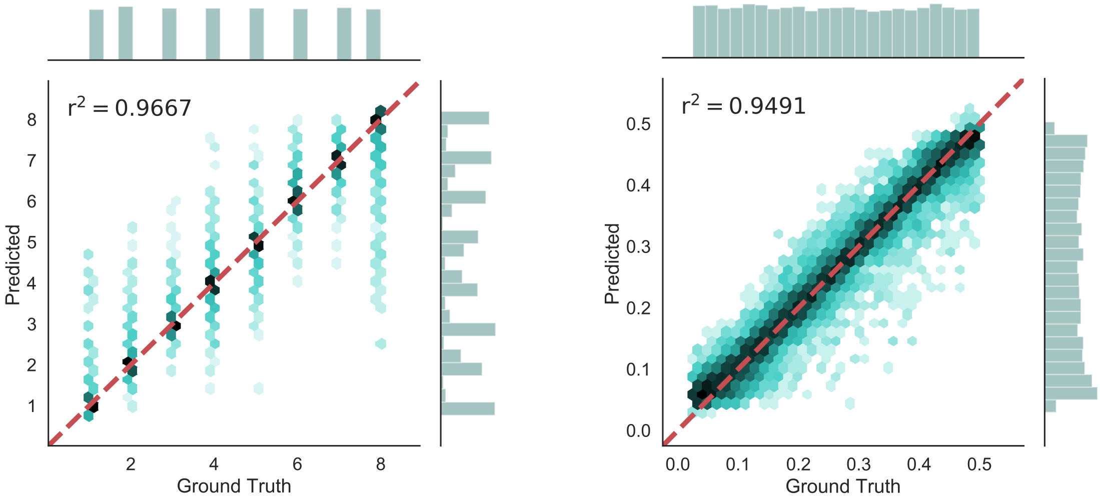

(a) Location cross-plot (b) Severity cross-plot

Figure 3.9: Infante bridge cross-plots for the testing dataset with measurement uncertainty

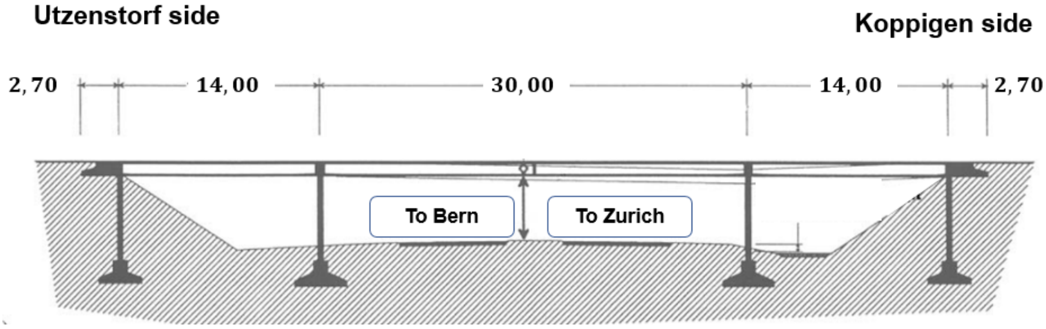

Figure 3.10: Z24 bridge in Switzerland [108]

Table 3.3: Numerical testing for Infante bridge in presence of measurement uncertainty.

Scenario	Ground truth		Prediction	
	Location	Severity (%)	Location	Severity (%)
10% stiffness reduction at L_1	1	5.00	1.06	5.93
30% stiffness reduction at L_1	1	15.00	0.97	15.32
10% stiffness reduction at L_8	8	5.00	7.83	5.32
30% stiffness reduction at L_8	8	15.00	8.00	21.36

3.8.2.1 Ambient vibration test

Previous to bridge demolition, some tests were carried out in the bridge under the SIMCES project, including progressive damage simulations [35]. Forced and ambient vibration tests were performed for the healthy structure and subsequent damage scenarios. In this work, we employ measurements from the ambient operational vibration tests (11-12 min length records of ambient accelerations including fixed and moving sensors in nine different set-ups) to identify the experimental first and second eigenmodes with high resolution. Further information regarding the configuration and measurements can be found in Reynders et al. [108] The available number of points describing each eigenmode allows to characterize the dynamic behavior of the bridge with only the first two eigenmodes. We employ the software MACEC [109] to obtain the natural frequencies and mode shapes from the acceleration signals. The first one is a vertical bending, and the second one corresponds to a torsion.

3.8.2.2 Parametrization

We build a parametrization in ANSYS® using shell elements for the deck and the piers and spring-type elements to model boundary conditions. The use of shell-type elements is justified since one of the selected mode shapes representing the structural behavior corresponds to a torsion. Shell elements provide a better distribution of the structural masses. Other works, such as [52] or [55], propose similar modeling elements, supporting the decision taken and the model validity. We consider five different locations (see Figure 3.11). The parametrization includes material properties (type a) and boundary conditions (type b). Material properties refer to the elastic modulus of the concrete. These properties describe locations one, two, and three. Locations one and three include seven material

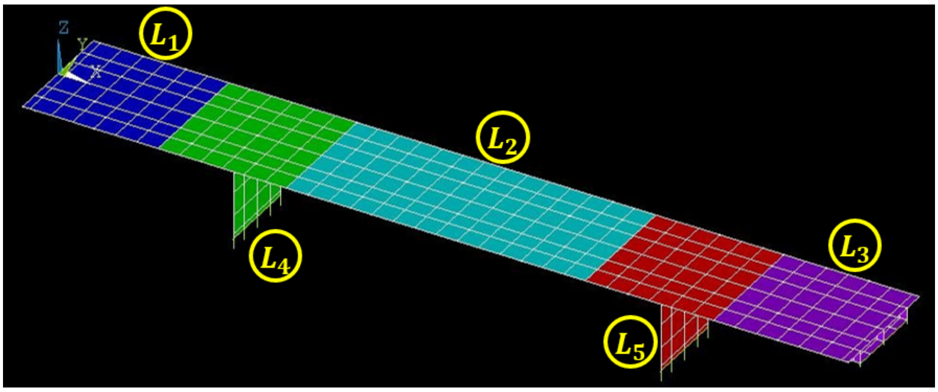

Figure 3.11: Parametrization of Z24 bridge with five locations

properties, and location two contains 14 along its length. We describe locations four and five (boundary conditions at the piers) with spring constants in the vertical direction (five properties describe each of these locations). A total of 38 properties are involved in this case of study.

We employ a Genetic Algorithm [78] to solve equation (3.4) and calibrate the parametrization. This yields a good numerical approximation to the response of the real bridge according to the ambient vibration test. Table 3.4 gathers the error terms in frequencies and eigenmodes before and after the updating process. For the eigenmodes, we employ the Modal Assurance Criterion (MAC) values [98].

Table 3.4: Results of the updating procedure.

Mode	Initial parametrization		Updated parametrization	
	Freq. error (%)	MAC	Freq. error (%)	MAC
1	0.54	0.9774	0.39	0.9886
2	0.02	0.9871	0.01	0.9930

3.8.2.3 Database generation

We set the minimum severity to $s_{min} = 0.05$ and the maximum to $s_{max} = 0.5$ based on sensitivity analysis and engineering criterion. During sensitivity analysis, we observed that damages below 5% barely introduced changes in the structural response. The multiplication factors in $\boldsymbol{\beta}$ range from 0 (undamaged property) to 0.5 (50% damage at that property). We solve $n = 8,000$ damage scenarios for each of the $n_z = 5$ locations, yielding a total of $N = 40,000$ samples. The time required to obtain the database was 30.6 hours. We calculate the dynamic response for each sample and match it with the corresponding damage label.

3.8.2.4 Deep Neural Network

We employ the network architecture described in section 3.6. The architecture of the neural network contains six hidden layers at the nonlinear connections $\mathcal{I}_{\gamma}^{n_1}$ and $\mathcal{I}_{\gamma}^{n_2}$. We employ a “ReLu” [59] activation function at the hidden layers of the nonlinear connection. The input layer receives a total of $m = 46$ input features. These include the first two eigenfrequencies and corresponding eigenmodes. The length of the mode shape vectors is 22 and includes points from both upstream and downstream measurement positions. The encoding phase compresses this input into a 17-dimensional feature vector. This topology provides adequate results.

We randomly split the database as follows: 72% of the samples are employed for training, 18% for validation, and the remaining 10% are kept for testing. We train the neural network through $5,000$ epochs. This number allows for sufficient training while preventing over-fitting. Figure 3.12 shows the evolution of the loss function for the training and validation datasets. The required training time was 10 min. We employ an optimizer that prevents from getting trapped in local minima during training [74]. This optimizer produces high loss function values at certain epochs, but we select the model with minimum validation loss.

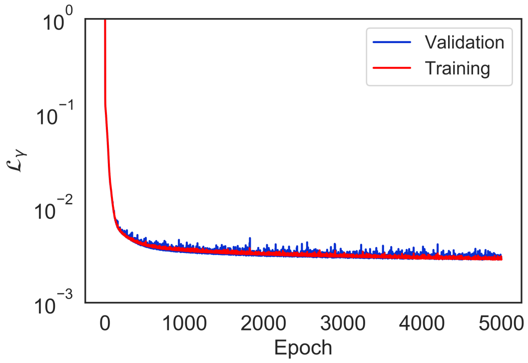

Figure 3.12: Loss evolution for the training and validation datasets (Z24 bridge)

We evaluate the performance of the trained network for the testing dataset. Figure 3.13 includes the cross-plot of the output variables. It shows that a high correlation exists between the real value (ground truth) and the prediction given by the network.

Now, we test the network for the available experimental damages. We employ two damages of increasing severity at the pier in the Koppigen side (see Fig-

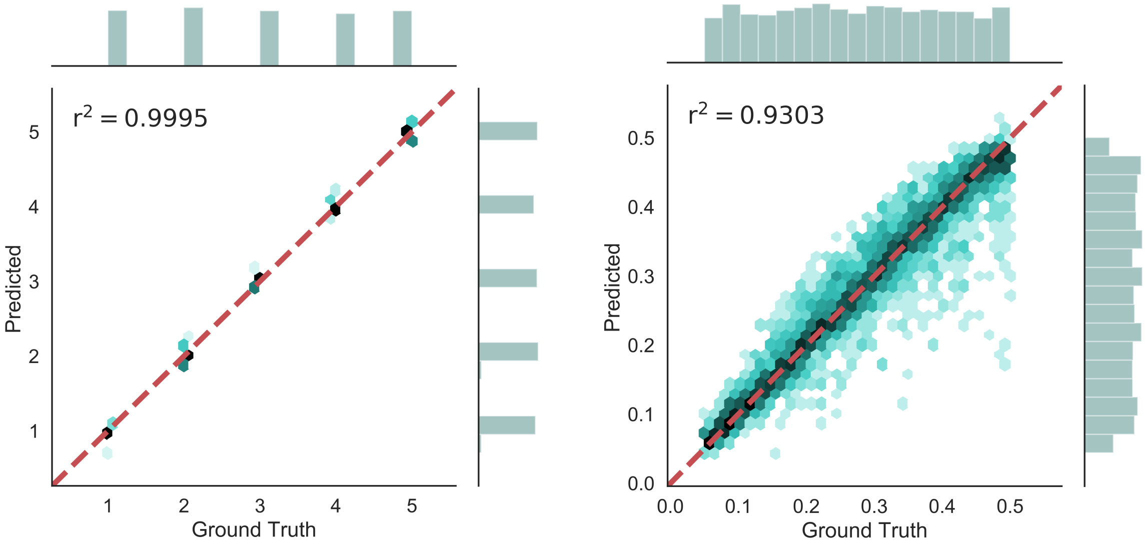

(a) Location cross-plot for the testing dataset. (b) Severity cross-plot for the testing dataset.

Figure 3.13: Z24 bridge testing cross-plots.

ure 3.10), that corresponds to location L_5 according to Figure 3.11. The damage consisted of pier settlements of 40 mm (D_1) and 80 mm (D_2) [19]. Both damages are considered to be of high severity [19]. The monitoring datasets consisted of two 10.9 minutes long time series sampled at 100 Hz. Peeters et al. [101] describe the experiments in more detail. We post-processed the acceleration signals to obtain the responses $\mathbf{m}_B^{D_1}$ and $\mathbf{m}_B^{D_2}$ and evaluated the DNN. Table 3.5 gathers the obtained results.

Table 3.5: Experimental validation with two damage scenarios.

Damage	Location	Severity (%)
D1	4.78	30.64
D2	5.00	43.64

We observe that the DNN correctly predicts the location of the damage. The true severity level is unknown for both scenarios, although we expect to obtain high values that increase from the first scenario to the second one. Accordingly, the obtained results indicate meaningful severity levels (above 30%).

4 Accounting for varying EOCs in the synthetic database

4.1 Introduction

In Chapter 3, we addressed the damage identification problem as a deterministic task. We employed the response $\mathbf{m}_B^h$ acquired during a short-term ambient vibration test as the reference to update a FE parametrization. This measurement corresponds to a particular date time with specific EOCs. We then generated the synthetic database according to the procedure described in sections 3.3 to 3.5. All the synthetic damage scenarios generated from the updated parametrization were assumed to occur under the same EOCs.

Figure 4.1 schematically represents the synthetic database for one zone in the bridge, where we generate n_s synthetic scenarios with varying damage severity within the interval $[0, 0.5]$. The same holds for the other zones. This approach disregards the effect of varying EOCs, which poses its main limitation. In prac-

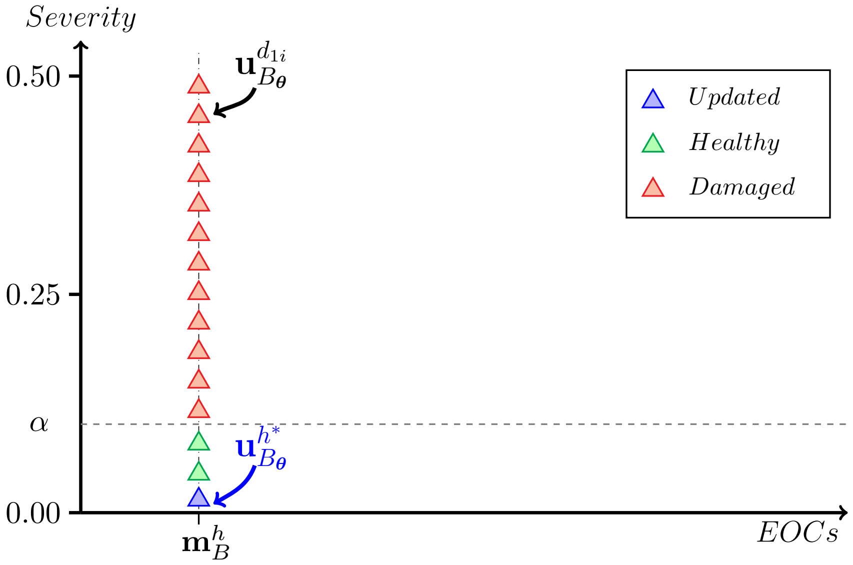

Figure 4.1: Original synthetic database representation

tice, neglecting these phenomena may hinder the damage detection task and yield a wrong assessment of the bridge behavior. In this chapter, we aim to enhance the methodology by incorporating the effect of varying EOCs in the training database of DNNs for damage assessment.

4.2 Gaussian Mixture Model clustering approach

Given an instrumented structure where long-term monitoring data are available (one year or more), we have access to a set of measurements M_B that corresponds to its healthy or reference behavior. These measurements include many healthy states with different EOCs, such that $M_B = \{\mathbf{m}_B^i\}_{i=1}^{N_m}$, where N_m is the total number of healthy samples measured during the monitoring period. Each measurement contains the eigenfrequencies and eigenmodes of the structure, $\mathbf{m}_B^i = \{\mathbf{f}_B^i, \mathbf{\Phi}_B^i\}$.

Environmental and operational conditions mainly include temperature, humidity, and traffic [141]. During long-term periods, these phenomena progressively change over time with certain seasonality. Ideally, we would like to generate a synthetic database that contains scenarios occurring at any possible combination of EOCs (see Figure 4.2). However, achieving this database is impractical and unfeasible. It requires solving an updating problem for each of the N_m available measurements to obtain the corresponding calibrated parametrizations.

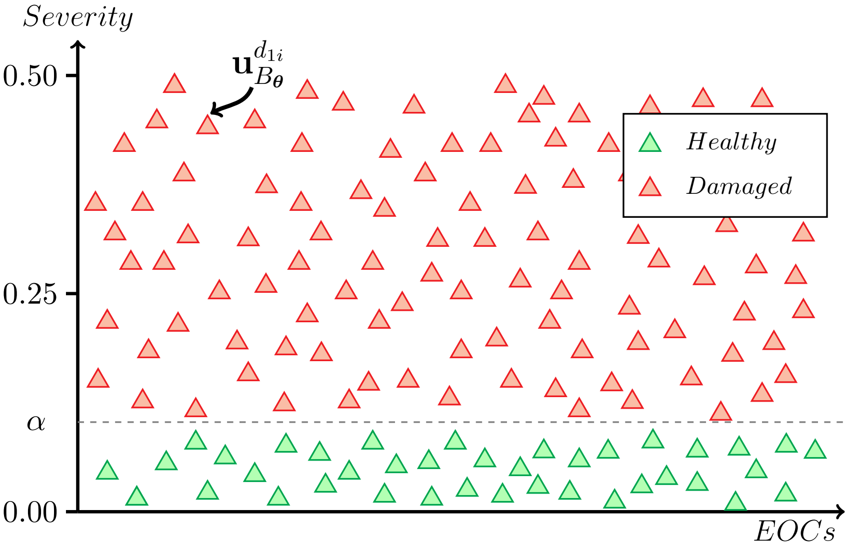

Figure 4.2: Ideal synthetic database representation

Alternatively, here we obtain some representative measurements that describe the entire dataset and include most EOC variation. By applying a clustering technique, we classify the long-term monitoring data into Q groups that characterize the existing variability. We employ a Gaussian Mixture Model (GMM) to address this issue [99]. A GMM is an unsupervised clustering method that classifies a dataset X according to probability density estimations on a mixture of Gaussians [99]. We define the GMM as a linear combination of multivariate Gaussian distributions such that the probability $P(X)$ is computed by:

$$P(X) = \sum_{q=1}^{Q} \pi_q \mathcal{N}(X|\mu_q, \Sigma_q), \tag{4.1a}$$

$$0 \leqslant \pi_q \leqslant 1, \quad \sum_{q=1}^{Q} \pi_q = 1, \tag{4.1b}$$

where π_q indicates the mixing coefficient or weight for the q-th Gaussian represented by its mean μ_q and covariance matrix Σ_q [99].

The GMM determines the linear combination of Gaussian functions that best separates the measurements into Q clusters using the Expectation Maximization algorithm [99, 36]. Each of these groups represents a set of EOCs sharing some common characteristics (e.g., high temperatures). The number of clusters is often decided based on metrics such as the Maximum log-likelihood [36]. Figure 4.3 shows an example of a GMM classification for two-dimensional measurements in X with $Q = 3$ clusters.

Here, we apply a Q-dimensional GMM to the available monitoring data M_B. Each measurement belongs to a cluster based on the highest probability among the Q Gaussians. We obtain a representative point for each cluster as that with minimal distance to the corresponding gaussian mean:

$$\mathbf{m}_B^{h_q} := \arg\min_{\mathbf{m}_B}(\rho^q_{\mathbf{m}_B}), \qquad q = 1, 2, ..., Q \tag{4.2}$$

where we calculate the distance as $\rho^q_{\mathbf{m}} = \sqrt{\sum_{j=1}^{v}(m_{B_j} - \mu_j^q)^2}$, with v indicating the dimension of the vectors. We select these representative meausurements, $\{\mathbf{m}_B^{h_1}, \mathbf{m}_B^{h_2}, ..., \mathbf{m}_B^{h_Q}\}$ and solve the updating task (see section 3.3.1) to produce the Q optimal FE parametrizations with responses $U_{B_{\boldsymbol{\theta}}}^{GMM} = \{\mathbf{u}_{B_{\boldsymbol{\theta}}}^{h_1^*}, \mathbf{u}_{B_{\boldsymbol{\theta}}}^{h_2^*}, ..., \mathbf{u}_{B_{\boldsymbol{\theta}}}^{h_Q^*}\}$. Finally, we generate synthetic scenarios following the steps in section 3.5. This approach sets a trade-off between the number of clusters and the computational cost of building the database. Figure 4.4 schematically represents the proposed database for one zone in the bridge (see Figure 3.4). The same holds for the other zones. The selected measurements are representative according to the GMM clustering. We thus expect that they cover most EOC variability.

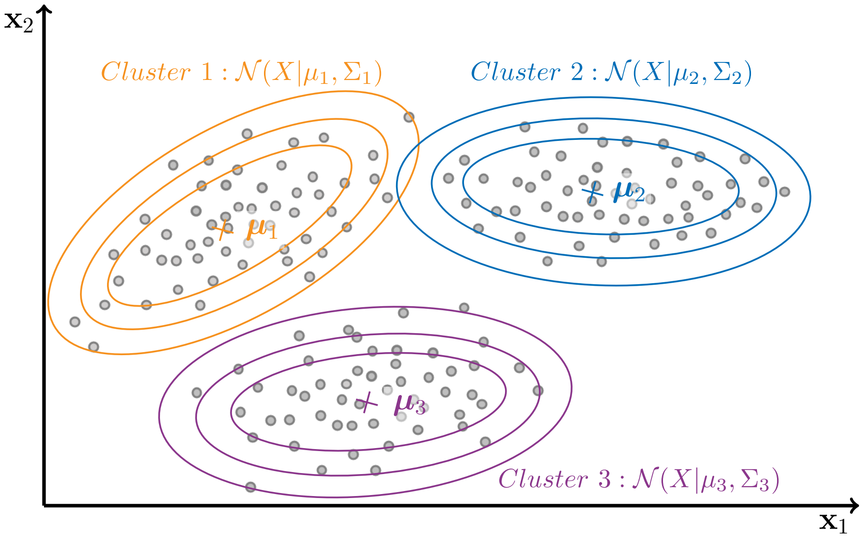

Figure 4.3: Example of GMM clustering with two-dimensional data

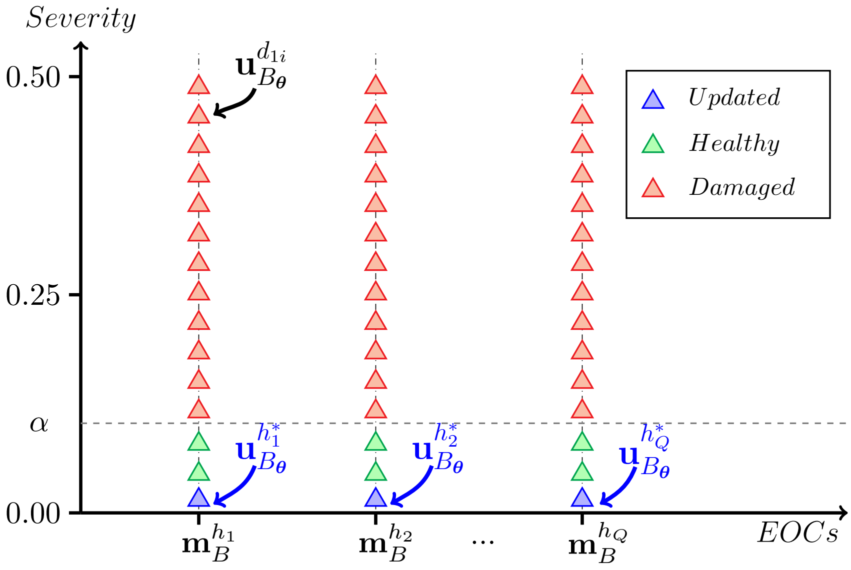

Figure 4.4: GMM-based synthetic database representation

4.3 Two-step damage assessment

The final goal of this methodology is to assess the structural condition and estimate the damage severity S and location L. Here, we propose a two-step approach to assess the bridge condition.

4.3.1 Severity estimation

We employ a DNN to estimate the damage severity, denoted by DNN_S. To train DNN_S, we include the available long-term monitoring data, M_B, which belong to the healthy state of the bridge. We assume that all the scenarios in M_B correspond to a severity value of $S = 0$, whereas the location label is unknown. These measurements contribute to learning different healthy states and preventing false positives. We then enrich M_B with the synthetic database previously generated in section 4.2. Once trained, DNN_S receives new measured data from the monitoring system and provides a severity diagnostic. If the estimated severity for a certain measurement exceeds the predefined threshold α, we assume that damage exists and raise an alert.

4.3.2 Location estimation

After detecting and quantifying the damage, a subsequent DNN (DNN_L) receives the measurement to indicate its location. We only train DNN_L with damaged samples from the database, i.e., those with a severity level $S \geqslant \alpha$. This methodology prevents healthy scenarios from contributing to the damage location, since they could mislead the diagnostic. Figure 4.5 shows a flowchart of the proposed approach.

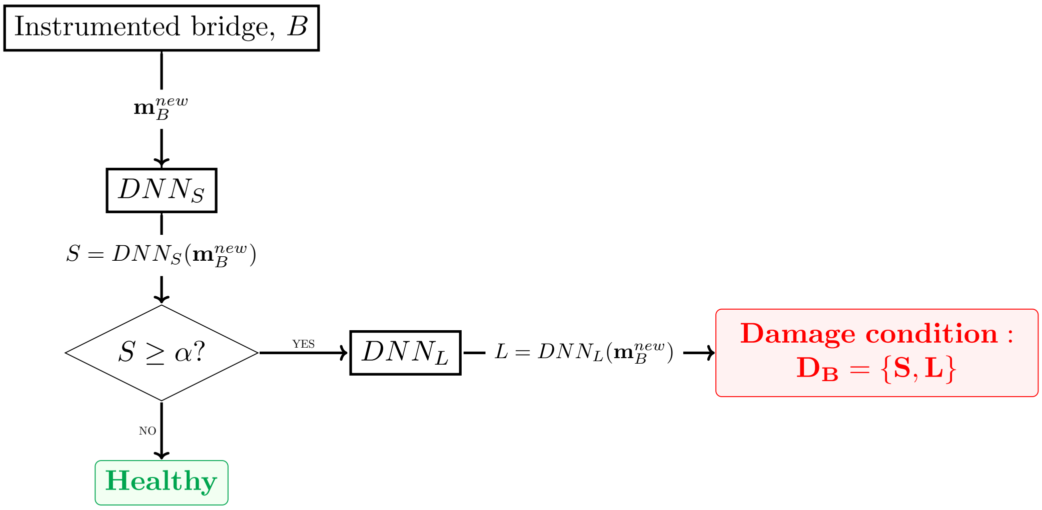

Figure 4.5: two-step assessment flowchart

For the training stage, we employ the same loss function introduced in equation 3.6 to measure the discrepancy between the predicted condition and the real state. We define two loss functions, one for each estimator. In $loss_S$, the inverse operator $\mathcal{I}_\gamma$ refers to DNN_S ($\boldsymbol{\gamma}$ contains the network parameters), and the damage condition is the severity level: $D_B = S$. Analogously, in $loss_L$, $\mathcal{I}_\gamma$ refers to the inverse operator DNN_L with damage condition $D_B = L$.

4.4 Numerical Results

We apply the proposed methodology to the case study of the Infante Dom Henrique bridge. We employ three years of long-term dynamic monitoring data. We introduce the monitoring system in section 2.8, and it is fully described in [86]. We employ four vertical acceleration signals from which we calculate the dynamic properties (eigenfrequencies and eigenmodes) every 30 minutes through an automatic OMA technique [85]. Any measurement in M_B includes $v = 32$ variables: $n_m = 4$ eigenfrequencies and corresponding eigenmodes acquired every thirty minutes. We obtain seven-dimensional eigenmodes by fitting a spline to the four measurements and obtaining the intermediate value between every two sensors. After removing null values, M_B contains a total of $N_m = 17,141$ samples.

4.4.1 GMM-based database

Given the high dimensionality of the dataset, we first apply PCA to compress the data and obtain relevant features for the clustering. Table 4.1 analyzes the explained variance for the first four principal components. The table reveals that the first PC explains most of the variance in the data, whereas the rest explains a residual part (< 5%). We compress the original measurements into one-dimensional features by transforming them as:

Table 4.1: Principal Component Analysis results

	$\mathbf{PC}_1$	$\mathbf{PC}_2$	$\mathbf{PC}_3$	$\mathbf{PC}_4$
Explained Variance (%)	95.55	1.80	0.92	0.72
Cumulated (%)	95.55	97.35	98.27	98.99

$$\hat{M}_B = TM_B, \tag{4.3}$$

where the transformation matrix T contains PC_1 coordinates.

We apply the GMM clustering technqiue to the transformed dataset $\hat{M}_B$. We would ideally cluster the data into thousands of groups to include the entire EOC variability, but using a large number of clusters conflicts with the computational cost of obtaining the synthetic scenarios. Particularly, each cluster adds approximately 17 hours of computational time, including the parametrization updating step and generating the synthetic scenarios for the database. Given that we aim to include most of the variability present in the data but with the computational restriction, we decide to employ five clusters ($Q = 5$). Table 4.2 presents the five mean values of the gaussians. Figure 4.6b displays the transformed dataset $\hat{M}_B$ colored by cluster label. Figure 4.6a shows the distribution of the samples in the Q clusters. According to Figure 4.6b, we appreciate that the data dispersion increases with the value of the PCA transformation feature. Cluster four contains only 54 samples very widely spread, indicating that they could be outliers. However, the analysis of these data is out of the scope of this work.

Table 4.2: Mean vector coordinates for the five clusters

	$\boldsymbol{\mu}_0$	$\boldsymbol{\mu}_1$	$\boldsymbol{\mu}_2$	$\boldsymbol{\mu}_3$	$\boldsymbol{\mu}_4$
Value	-1.3867	-1.3112	-1.1325	-0.8167	0.0024

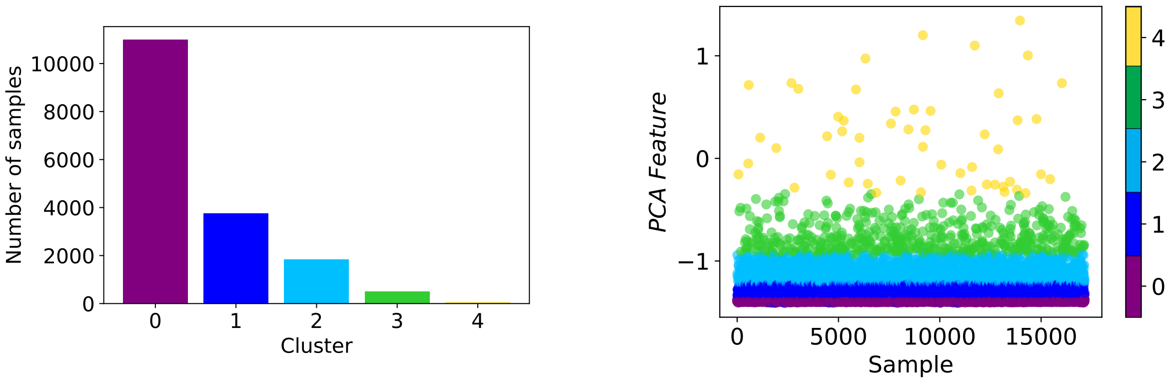

(a) Samples distribution.

(b) Dataset clustering.

Figure 4.6: Dataset clustering results for $Q = 5$.

After performing the clustering, we obtain the five points in the transformed space that lie closer to the means according to equation 4.2. Finally, we extract the corresponding 32-dimensional measurements: $M_B^{GMM} = \{\mathbf{m}_B^{h_0}, \mathbf{m}_B^{h_1}, \mathbf{m}_B^{h_2}, \mathbf{m}_B^{h_3}, \mathbf{m}_B^{h_4}\}$. For each of these five measurements, we solve the updating process to obtain the calibrated parametrizations, yielding the responses $U_{B_{\boldsymbol{\theta}}}^{GMM} = \{\mathbf{u}_{B_{\boldsymbol{\theta}}}^{h_0^*}, \mathbf{u}_{B_{\boldsymbol{\theta}}}^{h_1^*}, \mathbf{u}_{B_{\boldsymbol{\theta}}}^{h_2^*}, \mathbf{u}_{B_{\boldsymbol{\theta}}}^{h_3^*}, \mathbf{u}_{B_{\boldsymbol{\theta}}}^{h_4^*}\}$.

We generate the synthetic scenarios and conform the new database following the steps in section 3.5. We generate a total of $N_s = 80,000$ synthetic samples:

$n_s = 2,000$ samples for each of the $n_z = 8$ zones in the bridge and for each response in $U_{B_{\boldsymbol{\theta}}}^{GMM}$. The computational time of generating this database is of approximately 50 hours. The entire database contains $N = N_m + N_s = 97,141$ samples, including the experimental and the synthetic scenarios.

4.4.2 Deep Neural Networks for a two-step assessment

Here, we employ fully-connected feedforward DNNs with ReLU activation functions in the hidden layers. The architectures provide adequate performance. Optimizing the architectures is out of the scope of this research. We employ the complete response as the input (the four eigenfrequencies and eigenmodes). Thus, each sample contains $v = 32$ dimensions. Table 4.3 summarizes the properties of the DNNs. We first train the severity estimator DNN_S. We randomly split the available data (N samples) into 70% for training, 20% for validation, and 10% for testing.

Table 4.3: Summary of architecture and training specifications

ID	**Hidden Layers**	**Parameters**	**Optimizer**	**Batch size**	**LR**
DNN_S	9	36,597	Adam	8,196	10^{-4}
DNN_L	6	7,879	Adam	8,196	10^{-4}

We evaluate the performance of the network with the validation dataset. Figure 4.7a shows the severity cross-plot that compares the ground truth against the estimated severity values. The figure shows a high prediction performance with the r^2 metric reaching 0.96. We follow the same procedure for the location estimator, DNN_L. In this case, we restrict the training data to those scenarios where $S > \alpha$, with $\alpha = 0.05$ indicating the lowest detectable damage. Figure 4.7b shows the corresponding cross-plot that compares the ground truth against the estimated location values. The figure shows an adequate approximation of DNN_L given the high correlation factor during validation.

4.4.3 Synthetic testing

Here, we analyze the methodology in the task of damage identification. Since real damage scenarios are unavailable in full-scale operative bridge applications, we employ synthetic damage cases for testing.

We aim to analyze the enhancement of the proposed methodology with respect to the original approach described in Chapter 3in the task of damage identification. For the comparison, we generate a database according to Figure 4.1

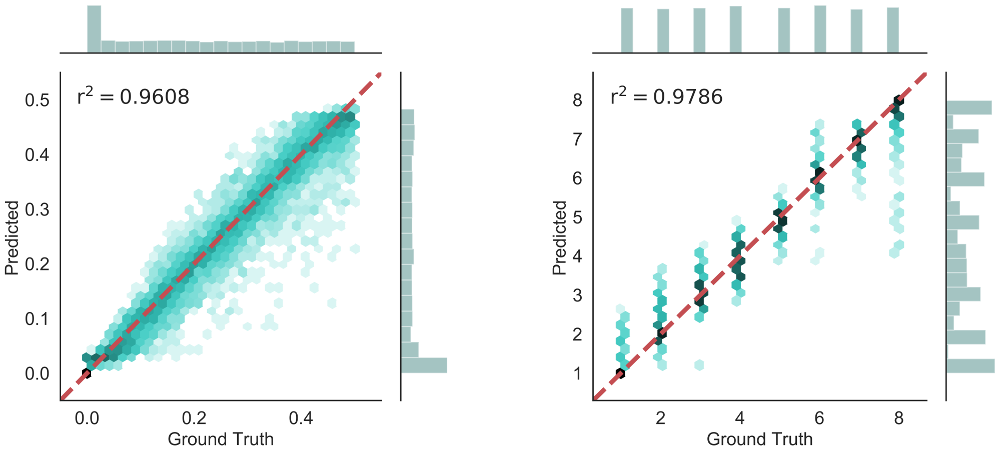

(a) Severity cross-plot

(b) Location cross-plot

Figure 4.7: DNN_S and DNN_L cross-plots during validation

that disregards the effect of changing EOCs. Given that cluster zero is the most significative in M_B according to Figure 4.6a, we employ $\mathbf{m}_B^{h_0}$ as the baseline healthy measurement to build the database. Hence, the original database contains the synthetic scenarios generated from $\mathbf{u}_{B_{\boldsymbol{\theta}}}^{h_0^*}$. We denote $DNN_S^{original}$ and $DNN_L^{original}$ to the neural networks described in section 4.4.2 trained with the original database.

4.4.3.1 Synthetic testing under seen EOCs

We first evaluate the damage detection performance for scenarios occurring under the same EOCs considered during training. This testing dataset corresponds to 10% of the available samples according to the database splitting (70% training, 20% validation, and 10% testing).

(A) Performance of the original approach: Here, we test the damage identification ability of the original database created from $\mathbf{u}_{B_{\boldsymbol{\theta}}}^{h_0^*}$. In this case, the testing subset contains damage scenarios occurring only under the particular EOCs of $\mathbf{m}_B^{h_0}$.

We first evaluate $DNN_S^{original}$ to estimate the severity of the damage. Figure 4.8a shows the corresponding cross-plot that displays the ground truth (real severity label) against the prediction provided by DNN_S. The squared correlation coefficient indicates a high performance. We subsequently estimate the location of the damage. Figure 4.8b displays the location cross-plot. $DNN_L^{original}$ also reveals an extraordinary performance during this test.

(B) Performance of the GMM-based method: We now test the damage identification ability of the new proposed database. This database contains synthetic scenarios generated from the updated parametrizations with responses stored in $U_{B_{\boldsymbol{\theta}}}^{GMM}$. Hence, the testing damage scenarios are assumed to occur under the same EOCs of the five corresponding measurements in M_B^{GMM}.

We evaluate DNN_S to estimate the severity of the damage. Figure 4.9a shows the resulting cross-plot. The squared correlation coefficient indicates a good performance with $r^2 \approx 0.94$. We subsequently estimate the damage location for those scenarios exceeding the threshold α. Figure 4.9b displays the cross-plot, revealing a very high performance of DNN_L. These results demonstrate that the proposed 2-step DNN assessment adequately performs when damage occurs under the same EOCs employed during training.

4.4.3.2 Synthetic testing under unseen EOCs

We now investigate the performance of the methodology for damage scenarios occurring under different EOCs unseen during the training phase. This test evaluates if applying GMM to select representative measurements for the training database contributes to generalizing the damage assessment task under different (unseen) EOCs.

We first select three test measurements from the monitoring data M_B that belong to three different clusters, denoted by $\{\mathbf{m}_B^{t_1}, \mathbf{m}_B^{t_2}, \mathbf{m}_B^{t_3}\}$. We employ only three measurements to restrict the computational cost required by the entire methodology. According to the clustering results in Figure 4.6a, we extract the measurements from the most relevant (highest occurrence frequency) clusters, namely, zero, one, and two. Table 4.4 summarizes the main properties of these measurements, including the value of the four eigenfrequencies, the PCA compressed feature, and the cluster label.

Table 4.4: Summary of selected testing points

Case	$\mathbf{f_1}$	$\mathbf{f_2}$	$\mathbf{f_3}$	$\mathbf{f_4}$	**PCA feature**	**Cluster**
$\mathbf{m}_B^{t_1}$	0.8121	1.1426	1.4123	2.0049	-1.3825	0
$\mathbf{m}_B^{t_2}$	0.8165	1.1491	1.4189	2.0184	-1.2678	1
$\mathbf{m}_B^{t_3}$	0.8172	1.1429	1.4064	1.9998	-1.1644	2

We solve the FE model updating process to obtain the calibrated parametrizations, yielding the responses $U_{B_{\boldsymbol{\theta}}}^{Test} = \{\mathbf{u}_{B_{\boldsymbol{\theta}}}^{t_1^*}, \mathbf{u}_{B_{\boldsymbol{\theta}}}^{t_2^*}, \mathbf{u}_{B_{\boldsymbol{\theta}}}^{t_3^*}\}$. We then generate $n_t = 50$ synthetic scenarios with random severity within the interval $[0, 0.5]$ for each of the $n_z = 8$ zones in the bridge according to section 3.5. The testing dataset contains a total of $1,200$ samples (400 for each parametrization in $U_{B_{\boldsymbol{\theta}}}^{Test}$). Figure 4.10 shows a representative example of the testing samples for one of the bridge zones with $n_t = 8$ synthetic scenarios. The figure makes clear that the testing EOCs are different from those considered during training.

(A) Performance of the original approach: We evaluate the performance of the original database generated from $\mathbf{m}_B^{h_0}$. Figure 4.12 shows the cross-plots for severity and location.

Figure 4.11a reveals that this approach fails to detect damage, with an overall score $r^2 \approx 0.37$. We observe that points from cluster zero present better estimations than those points belonging to clusters one and two. This result demonstrates that neglecting changes in EOCs during training misleads the assessment under different conditions. In the case of location, we also observe poor predictions from $DNN_L^{original}$, evidencing the unreliability of neglecting EOCs.

(B) Performance of the proposed GMM-based method: We finally evaluate the performance of the GMM-based methodology under changing EOCs. Figure 4.12a shows the severity cross-plot. The squared correlation coefficient indicates an adequate performance with $r^2 \approx 0.85$. We subsequently estimate the damage location for the scenarios with $S \geqslant \alpha$. Figure 4.12b displays the corresponding cross-plot. We also observe an adequate performance of DNN_L, with $r^2 \approx 0.85$. These results reveal that the proposed methodology gains robustness against the effect of varying EOCs during assessment. If more computational resources were available, we would consider a higher number of clusters to produce a more representative database that enhances the performance.

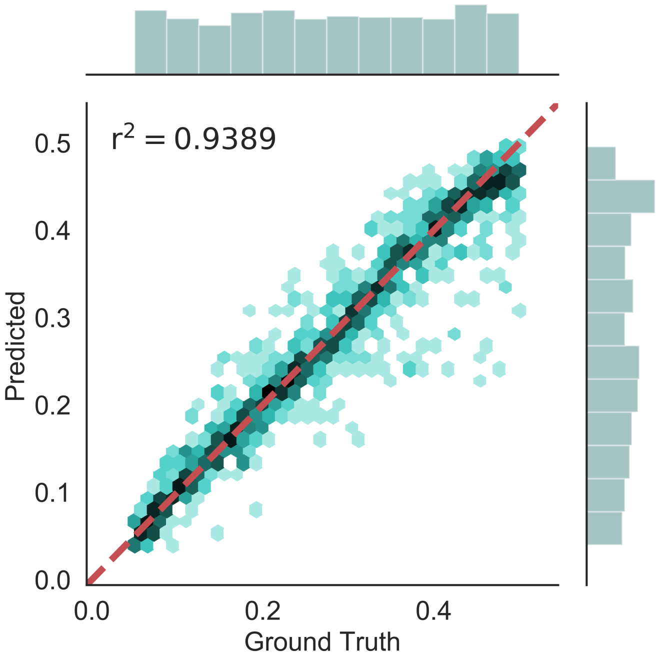

(a) Severity cross-plot under seen EOCs

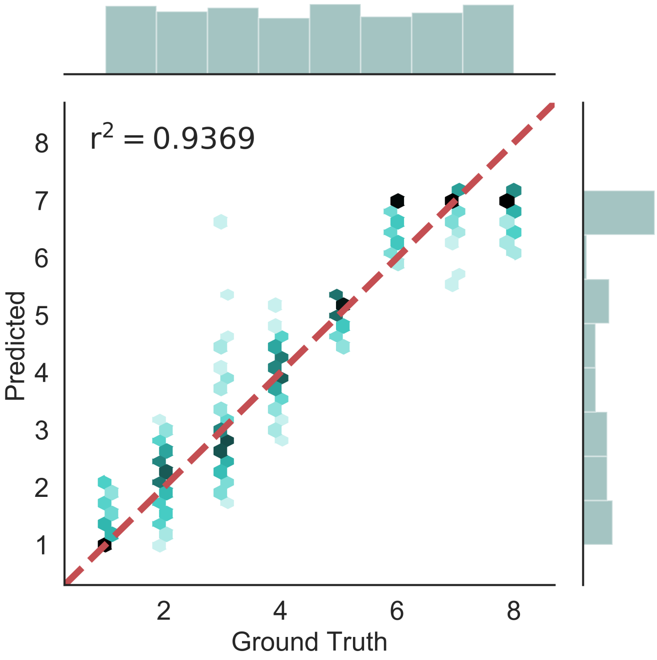

(b) Location cross-plot under seen EOCs

Figure 4.8: Testing cross-plots for the original approach under seen EOCs

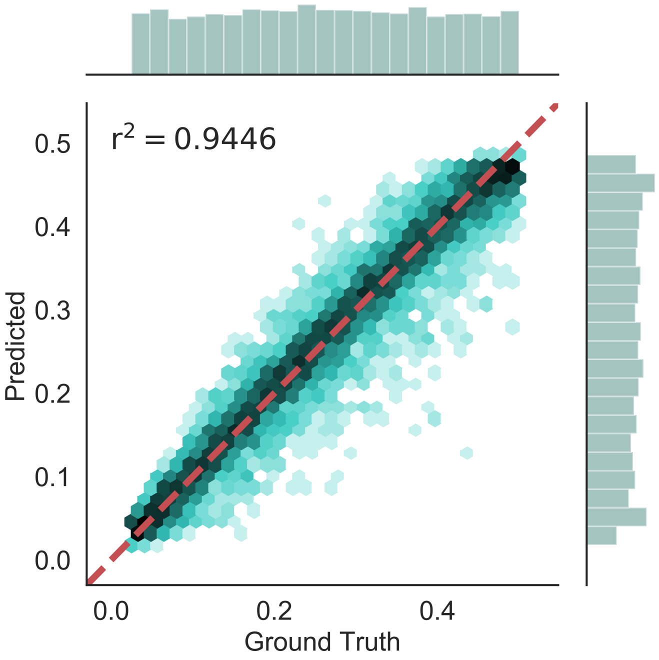

(a) Severity cross-plot under seen EOCs.

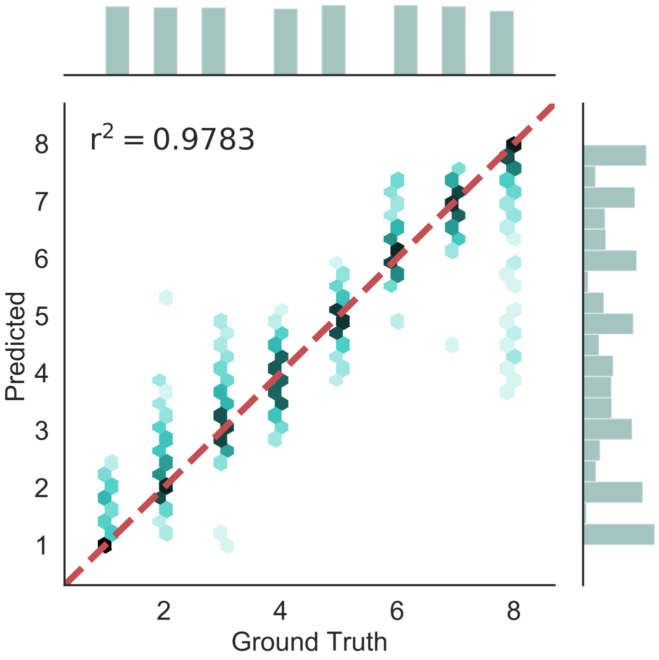

(b) Location cross-plot under seen EOCs.

Figure 4.9: Cross-plots during testing under seen EOCs for the new database

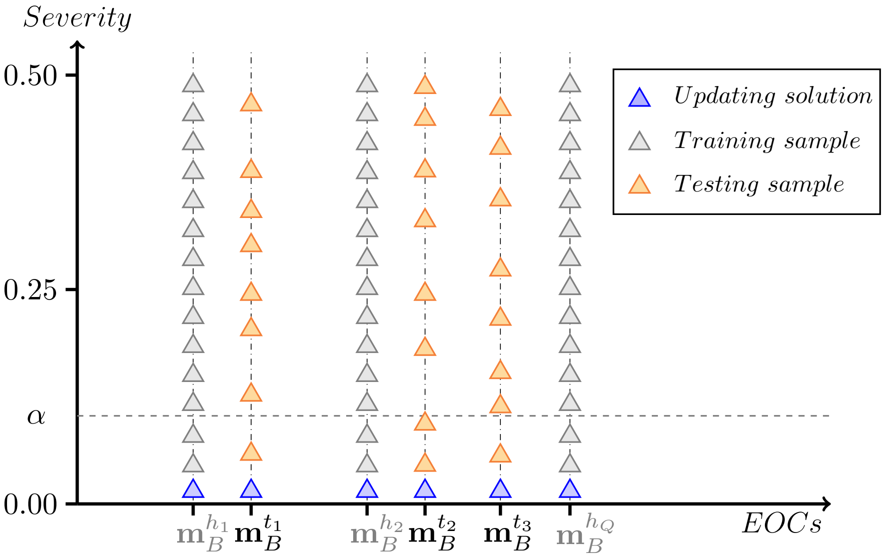

Figure 4.10: Example of synthetic testing samples under unseen EOCs

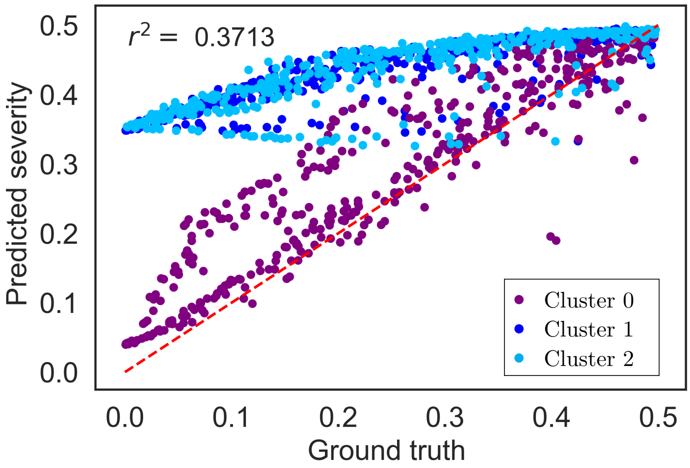

(a) Severity cross-plot under unseen EOCs

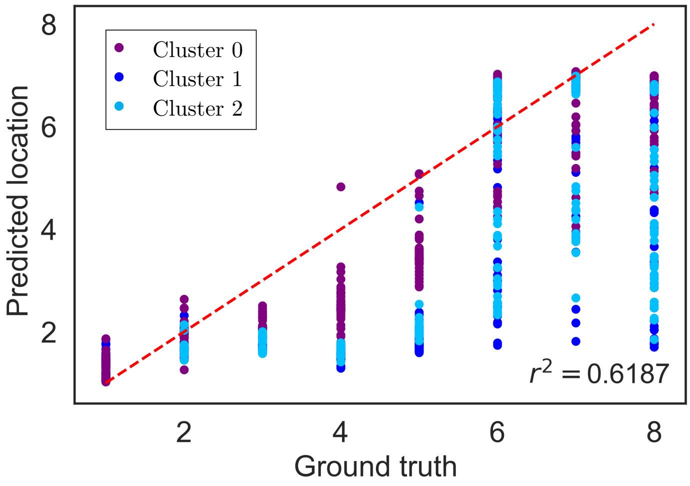

(b) Location cross-plot under unseen EOCs

Figure 4.11: Testing cross-plots for the original database under unseen EOCs

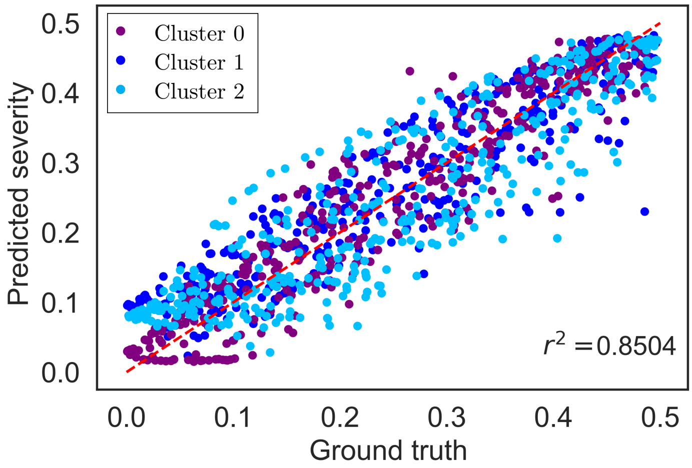

(a) Severity cross-plot under unseen EOCs

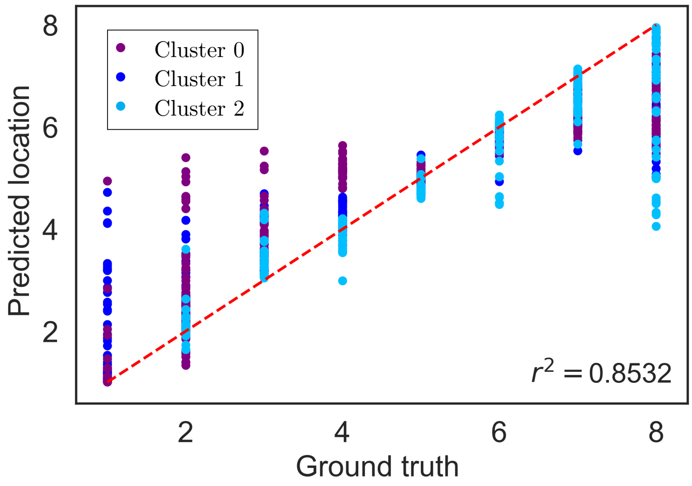

(b) Location cross-plot under unseen EOCs

Figure 4.12: Testing cross-plots for the proposed approach under unseen EOCs

5 Conclusions

5.1 Conclusions

In this dissertation, we investigate and develop various Structural Health Monitoring (SHM) techniques to solve the damage identification problem in bridge structures at different levels. We focus on the use of Deep Learning (DL) as the means to provide structural health diagnostics. We first explore the field of pure data-driven methods that produce alert systems able to detect the presence of damage. We develop an alert system that employs a particular Deep Neural Network (DNN) known as a deep residual autoencoder to rapidly detect structural damage. Subsequently, intending to achieve a more detailed assessment of the structural condition, we develop a hybrid approach that combines model and data-based techniques. We create a computational Finite Element (FE) parametrization to represent the real structure and generate synthetic damage scenarios that are experimentally unavailable. We employ these scenarios to train the data-driven method (DNNs) and provide assessment close to real-time, indicating the damage location and severity. We apply and validate the proposed methodologies with data from three real structures: the Beltran bridge in Mexico, the Infante Dom Henrique bridge in Porto, and the Z24 bridge in Switzerland.

In Chapter 2, we investigate the transition from a traditional data compression technique (Principal Component Analysis, PCA) to an enhanced DL approach in solving the damage detection problem based on a reconstruction error. We first describe the foundations of PCA and provide the step-by-step development of a deep residual autoencoder that replicates and enhances PCA in data reconstruction by including nonlinearities. We demonstrate that an autoencoder that applies linear transformations to compress and reconstruct the data captures the same level of information as PCA after an adequate training phase. By adding nonlinear transformations into the architecture as residual (parallel) blocks, we ensure that the worse possible solution is at least as good as that of PCA, under the assumption that the optimizer finds the global minima. We conclude that this novel architecture outperforms PCA detection ability mainly when working with highly complex multivariate datasets. Besides, it allows employing the linear architecture in simpler data spaces.

We validate the methodology using data from bridges Beltran (Mexico) and

Infante dom Henrique (Porto). Improving the reconstruction task with the residual autoencoder reduces the false positive rates during testing. It also reduces the false negative rates and allows us to detect lighter severity levels, indicating that we can discover damage at earlier stages.

We devote the last part of Chapter 2 to analyzing the contribution of different types of measurable variables, grouped into local and global. We employ the Receiver Operating Curves (ROC) curves to compare the effectiveness of using (a) local variables only, (b) global variables only, and (c) the combination of both. Local variables are strongly sensitive to damage occurring nearby their emplacement but fail for other damage locations. Global variables such as eigenfrequencies broaden the detectable locations to the entire structure but lose sensitivity to slight damage. In summary, combining both sources of data provides a more complete and robust assessment.

An essential point in locating damage lies in the adequate disposal of the long-term monitoring sensors. Deploying a large number of sensors helps to improve the diagnostics, but it results in inadmissible costs. An intelligent positioning strategy might yield a more efficient solution. Particularly important locations are: (a) those more susceptible to suffering damage (e.g. joints, pier foundations, etc.), and (b) those where eigenmodes present reduced curvature since global variables lose sensitivity at these positions. Since eigenmodes can be obtained beforehand (through an ambient vibration test or numerical simulations), those nodes that are more “blind” to global variables can be identified and supported with local variable sensors.

In Chapter 3, we implement and test a novel SHM methodology to identify damage that induces a stiffness reduction at a specific part of the structure. We employ experimental measurements from ambient vibration tests to adjust the properties of a FE parametrization of the bridge and approximate the measured dynamic response (natural frequencies and mode shapes). By grouping the structural properties of the parametrization into various regions where damage may occur, we design a database that includes different scenarios labeled by damage location and severity. The proposed DNN captures the relationship between the dynamic response of the structure and the presence of damage with reduced error after adequate training. The methodology demonstrates to be easily adaptable to different types of bridges. The use of labeled synthetic samples corresponding to specific damage location and severity levels during the DNN training enables reaching a higher level in the diagnostic scale according to Rytter [114].

We validate the methodology with two full-scale cases of study: Infante Dom Henrique and Z24. For the Infante bridge, we achieve adequate results, including successful prediction of two synthetic damage scenarios evaluated as testing. We also explore the robustness of the method in presence of measurement error by introducing noise and environmental variability by adding a term to the responses of the synthetic scenarios in the database. The availability of two experimental damage scenarios of increasing severity in the Z24 case study allows us to evaluate the performance beyond the numerical frame. The DNN correctly estimates the location of the pier settlements applied before the bridge demolition. The exact severity level of these damage scenarios is unknown, but high values are expected and achieved, demonstrating the ability of the methodology.

One of the most important challenges in assessing the health condition of operative bridge structures is tackling the effect of varying Environmental and Operational Conditions (EOCs). Pure data-driven methods often require long-term monitoring data for training that cover most of this variability. However, when employing computational simulations to enlarge the identification space beyond the undamaged condition, we need to somehow incorporate EOCs in the synthetic damage scenarios. The ideal training database would contain infinite damage scenarios occurring at any possible combination of EOCs, but such approach is inefficient and unfeasible.

In Chapter 4, we propose a novel approach to efficiently create a synthetic database that accounts for varying EOCs. We employ a Gaussian Mixture Model (GMM) to cluster the experimental data and select some significant points from which we build the synthetic database. We compare the performance of the original methodology (one single measurement as the baseline) with the new approach (five measurements representaive of the different clusters as the baseline) in the task of damage identification with data from the Infante bridge. The original approach fails when damage occurs under EOCs different from those of the measurement employed to generate the training scenarios. We conclude that neglecting the effect of EOCs during the training phase of DNNs has detrimental consequences in diagnostics. Including various measurements with different EOCs in the database generation enhances the performance of the method and allows generalizing the assessment to a wide range of EOCs. The main limitation of the proposed method is the restrictive trade-off between the number of employed measurements and the computational cost of generating the database.

5.2 Future work

The proposed pure data-driven SHM method based on a deep residual autoencoder yields very robust alert systems able to early detect damage with no need for complex computational models. Despite their low diagnostic level [114], alert systems constitute the preliminary assessment tool to detect the presence of any abnormal behavior or malfunction in the structure and activate more detailed inspections. Given the successful results obtained when applied to very different bridges, we consider future work transferring the methodology to other areas, such as wind energy (onshore and offshore) or gas transport. These industries are in continuous development, and SHM practices are of huge interest to provide enhanced assessment and maintenance.

On the other hand, when attempting to provide a more insightful diagnostic, we need to rely on computational mechanics to enrich the training phase of DNNs. In this multidisciplinary domain, there exist multiple sources of uncertainty and error, including measurements, material and structural properties, and computation. Also, we know that varying EOCs constitute a highly relevant aspect of diagnostics. Although the approach we propose in Chapter 4 gains robustness against varying EOCs in comparison with using only one measurement, it lacks a quantification of the uncertainty. We consider as future work exploring the implementation of bayesian DNNs, which deliver confidence estimates that provide more robustness and reliability to the diagnostics.

6 Main achievements

6.1 Scientific Achievements

This dissertation intends to contribute to the transition from research to the real practice of SHM damage detection methods for full-scale operating bridge structures. We address the implementation of Deep Learning techniques from a mathematical understanding found in traditional data compression techniques such as PCA to provide comprehensible solutions. We contribute to this applicability through various developments, some of them already included in recent publications [53, 43, 44].

In work [53], we provide an unsupervised SHM approach based on PCA to monitor the global behavior of the sliding bearings in the Beltran viaduct, in Mexico. We first demonstrate the existence of strong linear correlations in the relative displacements measured at the deck-pier connections of the bridge during nine months of monitoring. We then employ linear PCA to compress the measurements and design a robust performance indicator for outlier detection that is only weakly affected by temperature variations. This work delivers a fully applicable SHM practice for operating bridges that satisfy the assumption of linearly correlated measurements.

Work [43] proposes a DL-based enhancement of PCA for outlier detection to assess the structural condition of two operating bridges. We investigate the limitations of linear PCA by first replicating its compression and reconstruction ability with an autoencoder NN architecture. We then incorporate deep residual connections to account for nonlinear relationships in a partialy explainable way. By fixing the weights obtained after training the linear autoencoder, we realize the enhancement provided by including nonlinear relationships. The blockwise configuration of the autoencoder enables the activation or deactivation of the residual connections. This work provides an enhanced outlier detection methodology for full-scale bridges that adapts to both linear and nonlinear variability environments.

We also provide a comparative study regarding the use of global and local monitoring variables, as well as their combination. We apply the deep residual autoencoder architecture developed in [43] to long-term monitoring data including (a) global variables (eigenfrequencies), (b) local variables (inclinations and strains), and (c) the combination of both. We first investigate the contribution of each variable type in the detection of damage, demonstrating that combining both sources of data contributes to extend the detectable damage locations and reduce the minimium sensitivity level. We subsequently analyze the potential of local variables to determine the location of damage when it occurs nearby a particular sensor emplacement. This work reveals the benefits of deploying complementary monitoring systems to achieve robust and insightful damage detection assessment for large bridge structures under service. We have written a paper that is currently under review, entitled: ***Deep Neural Network for damage detection in Infante Dom Henrique bridge using multi-sensor data***.

Work [44] addresses the inverse problem of damage identification throughout a supervised learning approach. We overcome the lack of real damage scenarios using FE simulations that recreate stiffness reductions at different bridge parts and obtain the dynamic response in the form of eigenfrequencies and eigenmodes. Computational mechanics provide the basis to understand and simulate the behavior of the bridge structures. We define the relationship between the FE parametrized damage and two identification labels: location and severity. We then train a DNN that maps the dynamic response of the bridge to its health condition according to the damage description labels. This work provides a higher level diagnostic compared to the unsupervised approaches addresed in [53, 43] since it estimates the location and severity level of the damage.

Finally, we also explore the challenging task of including the effect of varying environmental and operational conditions in the combined methodology proposed in [44]. This last research provides a novel methodology based on Gaussian Mixture models to classify experimental data and select significant points to build the synthetic database for training. We are currently finishing a new publication regarding this work, entitled ***Damage identification under varying ambient conditions combining Deep Learning and Computaional simulations. Application to a real bridge.***

6.2 Peer-reviewed publications

2020 D. Garcia-Sanchez, A. Fernandez-Navamuel, D. Zamora-Sánchez, D. Alvear, and D. Pardo. ***Bearing assessment tool for longitudinal bridge performance.*** Journal of Civil Structural Health Monitoring 10, 1023–1036 (2020).

2022 A. Fernandez-Navamuel, F. Magalhães, D. Zamora-Sánchez, Á.J. Omella, D. Garcia-Sanchez, and D. Pardo. ***Deep learning enhanced principal***

component analysis for structural health monitoring. Structural Health Monitoring. 2022;21(4):1710-1722. doi:10.1177/14759217211041684.

2022 A. Fernandez-Navamuel, D. Zamora-Sánchez, Á.J. Omella, D. Pardo, D. Garcia-Sanchez, and F. Magalhães. ***Supervised Deep Learning with Finite Element simulations for damage identification in bridges.***Engineering Structures. 257. 114016. 10.1016/j.engstruct.2022.114016.

2022 A. Fernandez-Navamuel, D. Pardo, F. Magalhães, D. Zamora-Sánchez, Á.J. Omella, and D. Garcia-Sanchez. ***Deep Neural Network for damage detection in Infante Dom Henrique bridge using multi-sensor data.*** Structural Control and Health Monitoring (under review).

2022 A. Fernandez-Navamuel, D. Pardo, F. Magalhães, D. Zamora-Sánchez, Á.J. Omella, and D. Garcia-Sanchez. ***Damage identification under varying ambient conditions combining Deep Learning and Computaional simulations. Application to a real bridge.***

6.3 Conferences and Workshops

2019 A. Fernandez-Navamuel and D. Garcia-Sanchez, ***Damage detection tool development for decision making in bridge management.*** 2nd SAFE-FLY International Conference. May 08-10 2019, Vitoria-Gasteiz

2021 D. Zamora-Sánchez and A. Fernandez-Navamuel, ***Structural Health Monitoring Fundamentals: Surfacing in an ocean of SHM Algorithms.*** 3rd Online workshop of the Stakeholders Reference Group on Monitoring-based Decision Support for Resilient Transport Infrastructures. FORESEE Project. March 18 2021

2022 A. Fernandez-Navamuel, D. Zamora-Sánchez, T. Varona Poncela, C. Jiménez-Fernández, J. Díez-Hernández, D. Garcia-Sanchez, and D. Pardo. ***Vibration-based SHM strategy for a real time alert system with damage location and quantification.*** 10th European Workshop on Structural Health Monitoring (10th EWSHM). July 04-07 2022 Palermo, Italy (Held online).

2022 A. Fernandez-Navamuel, D. Zamora-Sánchez, D. Garcia-Sanchez, F. Magalhães, and D. Pardo. ***Damage detection in bridge structures using an unsupervised Deep Autoencoder*** 8th European Congress on Computational Methods in Applied Sciences and Engineering. June 05-09 2022 Oslo, Norway.

2022 A. Fernandez-Navamuel, D. Zamora-Sánchez, D. Garcia-Sanchez, F. Magalhães, and D. Pardo. ***Bridge damage detection using Deep Autoencoder Networks*** Congress on Numerical Methods in Engineering. September 12-14 2022, Gran Canaria, Spain.

Bibliography

[1] M. Abadi, P. Barham, J. Chen, Z. Chen, A. Davis, J. Dean, M. Devin, S. Ghemawat, G. Irving, M. Isard, M. Kudlur, J. Levenberg, R. Monga, S. Moore, D. G. Murray, B. Steiner, P. Tucker, V. Vasudevan, P. Warden, M. Wicke, Y. Yu, and X. Zheng. Tensorflow: A system for large-scale machine learning, 2016.

[2] O. Abdeljaber, O. Avci, S. Kiranyaz, M. Gabbouj, and D. J. Inman. Real-time vibration-based structural damage detection using one-dimensional convolutional neural networks. *Journal of Sound and Vibration*, 388(February):154–170, 2017.

[3] A. Adão da Fonseca and R. O. Bastos. Monitorização em fase de serviço do comportamento estrutural da Ponte Infante D. Henrique. *Encontro Nacional de Betão Estrutural*, (Ø13 mm):24–26, 2004.

[4] K. Alten, M. Ralbovsky, A. Vorwagner, H. Toplitzer, and S. Wittmann. Evaluation of Different Monitoring Techniques during Damage Infliction on Structures. In *Procedia Engineering*, volume 199, pages 1840–1845. Elsevier Ltd, 2017.

[5] V. Alves and A. Cury. A fast and efficient feature extraction methodology for structural damage localization based on raw acceleration measurements. *Structural Control and Health Monitoring*, 28(7):e2748, 2021.

[6] V. N. Alves, M. M. de Oliveira, D. Ribeiro, R. Calçada, and A. Cury. Model-based damage identification of railway bridges using genetic algorithms. *Engineering Failure Analysis*, 118:104845, 2020.

[7] T. Amarbayasgalan, B. Jargalsaikhan, and K. H. Ryu. Unsupervised novelty detection using deep autoencoders with density based clustering. *Applied Sciences (Switzerland)*, 8(9), 2018.

[8] Y. An, E. Chatzi, S. H. Sim, S. Laflamme, B. Blachowski, and J. Ou. Recent progress and future trends on damage identification methods for bridge structures, oct 2019.

[9] Y. An, E. Chatzi, S.-H. Sim, S. Laflamme, B. Blachowski, and J. Ou. Recent progress and future trends on damage identification methods for bridge structures. *Structural Control and Health Monitoring*, 26(10):e2416, 2019. e2416 STC-18-0435.R3.

[10] P. Angelov and E. Soares. Towards explainable deep neural networks (xDNN). *Neural Networks*, 130:185–194, 2020.

[11] A. G. Asuero, A. Sayago, and A. G. González. The correlation coefficient: An overview. *Critical Reviews in Analytical Chemistry*, 36(1):41–59, 2006.

[12] O. Avci, O. Abdeljaber, S. Kiranyaz, M. Hussein, M. Gabbouj, and D. J. Inman. A review of vibration-based damage detection in civil structures: From traditional methods to machine learning and deep learning applications. *Mechanical Systems and Signal Processing*, 147:107077, 2021.

[13] M. R. Azim and M. Gül. Data-driven damage identification technique for steel truss railroad bridges utilizing principal component analysis of strain response. *Structure and Infrastructure Engineering*, 17(8):1019–1035, 2021.

[14] M. Azimi, A. D. Eslamlou, and G. Pekcan. Data-driven structural health monitoring and damage detection through deep learning: State-of-the-art review. *Sensors*, 20(10), 2020.

[15] M. Azimi and G. Pekcan. Structural health monitoring using extremely compressed data through deep learning. *Computer-Aided Civil and Infrastructure Engineering*, 35(6):597–614, 2020.

[16] A. Bellino, A. Fasana, L. Garibaldi, and S. Marchesiello. PCA-based detection of damage in time-varying systems. *Mechanical Systems and Signal Processing*, 24(7):2250–2260, 2010.

[17] H. Bourlard and Y. Kamp. Auto-association by multilayer perceptrons and singular value decomposition. *Biological cybernetics*, 59:291–4, 02 1988.

[18] A. P. Bradley. The use of the area under the roc curve in the evaluation of machine learning algorithms. *Pattern Recognition*, 30(7):1145–1159, 1997.

[19] R. Brincker, P. Andersen, and L. Zhang. Modal Identification and Damage Detection on a Concrete Highway Bridge by Frequency Domain Decomposition. *Structural Engineers World Congress*, pages 1–8, 2002.

[20] R. Brincker and C. E. Ventura. *Time Domain Identification*, chapter 9, pages 239–260. John Wiley and Sons, Ltd, 2015.

[21] R. Brincker, L. Zhang, and P. Andersen. Modal identification of output-only systems using frequency domain decomposition. *Smart Materials and Structures*, 10(3):441, 2001.

[22] J. M. Brownjohn. Structural health monitoring of civil infrastructure. *Philosophical Transactions of the Royal Society A: Mathematical, Physical and Engineering Sciences*, 365(1851):589–622, 2007.

[23] J. M. Brownjohn, F. Magalhaes, E. Caetano, and A. Cunha. Ambient vibration re-testing and operational modal analysis of the Humber Bridge. *Engineering Structures*, 32(8):2003–2018, 2010.

[24] A. Cancelli, S. Laflamme, A. Alipour, S. Sritharan, and F. Ubertini. Vibration-based damage localization and quantification in a pretensioned concrete girder using stochastic subspace identification and particle swarm model updating. *Structural Health Monitoring*, 19:147592171882001, 02 2019.

[25] A. L. Caterini and D. E. Chang. *Deep Neural Networks in a Mathematical Framework*. 2018.

[26] R. Chalapathy, A. K. Menon, and S. Chawla. Anomaly detection using one-class neural networks. *Computer Science, Mathematics*, abs/1802.06360, 2018.

[27] H.-P. Chen and Y.-Q. Ni. *Structural Damage Identification Techniques*, chapter 4, pages 69–90. John Wiley and Sons, Ltd, 2018.

[28] J. Chen, S. Sathe, C. Aggarwal, and D. Turaga. Outlier detection with autoencoder ensembles. *Proceedings of the 17th SIAM International Conference on Data Mining, SDM 2017*, pages 90–98, 2017.

[29] Z. Chen, X. Zhou, X. Wang, L. Dong, and Y. Qian. Deployment of a smart structural health monitoring system for long-span arch bridges: A review and a case study. *Sensors*, 17(9), 2017.

[30] F. Choi, K. Crews, B. Samali, and J. Li. Calibration of a laboratory timber bridge finite element model using the experimental modal data. *9th World Conference on Timber Engineering 2006, WCTE 2006*, 1, 2006.

[31] G. Comanducci, F. Magalhães, F. Ubertini, and Álvaro Cunha. On vibration-based damage detection by multivariate statistical techniques: Application to a long-span arch bridge. *Structural Health Monitoring*, 15(5):505–524, 2016.

[32] E. J. Cross, G. Manson, K. Worden, and S. G. Pierce. Features for damage detection with insensitivity to environmental and operational variations. *Proceedings of the Royal Society A: Mathematical, Physical and Engineering Sciences*, 468:4098 – 4122, 2012.

[33] A. A. da Fonseca. The Infant Henrique Bridge over the River Douro , in Porto , Portugal. *International Conference on Arch Bridges*, pages 931–960, 2007.

[34] J. Dan, W. Feng, X. Huang, and Y. Wang. Global bridge damage detection using multi-sensor data based on optimized functional echo state networks. *Structural Health Monitoring*, 20:1924–1937, 2021.

[35] G. De Roeck. The state-of-the-art of damage detection by vibration monitoring: The SIMCES experience. *Journal of Structural Control*, 10(2):127–134, 2003.

[36] M. P. Deisenroth, A. A. Faisal, and C. S. Ong. *Mathematics for Machine Learning.* Cambridge University Press, 2020.

[37] N. Dervilis, I. Antoniadou, R. J. Barthorpe, E. J. Cross, and K. Worden. Robust methods for outlier detection and regression for SHM applications. *International Journal of Sustainable Materials and Structural Systems*, 2(1/2):3, 2015.

[38] C.-Z. Dong and F. N. Catbas. A review of computer vision-based structural health monitoring at local and global levels. *Structural Health Monitoring*, 20(2):692–743, 2021.

[39] D. Farhey. Instrumentation system performance for long-term bridge health monitoring. *Structural Health Monitoring-an International Journal - STRUCT HEALTH MONIT*, 5:143–153, 06 2006.

[40] C. Farrar and K. Worden. *Structural Health Monitoring A Machine Learning Perspective.* Wiley, 01 2013.

[41] C. R. Farrar, S. W. Doebling, and D. A. Nix. Vibration-based structural damage identification. 359(1778):131–149, jan 2001.

[42] A. Fathi and M. P. Limongelli. Statistical vibration-based damage localization for the s101 bridge, flyover reibersdorf, austria. *Structure and Infrastructure Engineering*, 0(0):1–15, 2020.

[43] A. Fernandez-Navamuel, F. Magalhães, D. Zamora-Sánchez, Ángel J Omella, D. Garcia-Sanchez, and D. Pardo. Deep learning enhanced principal component analysis for structural health monitoring. *Structural Health Monitoring*, 0(0):14759217211041684, 0.

[44] A. Fernandez-Navamuel, D. Zamora-Sánchez, Ángel J. Omella, D. Pardo, D. Garcia-Sanchez, and F. Magalhães. Supervised deep learning with finite element simulations for damage identification in bridges. *Engineering Structures*, 257:114016, 2022.

[45] E. Figueiredo, I. Moldovan, A. Santos, P. Campos, and J. C. Costa. Finite Element-Based Machine-Learning Approach to Detect Damage in Bridges under Operational and Environmental Variations. *Journal of Bridge Engineering*, 24(7):1–13, 2019.

[46] E. Figueiredo, G. Park, C. R. Farrar, K. Worden, and J. Figueiras. Machine learning algorithms to damage detection under operational and environmental variability. In T. Kundu, editor, *Health Monitoring of Structural and Biological Systems 2010*, volume 7650, page 76502E. SPIE, mar 2010.

[47] E. Figueiredo, G. Park, C. R. Farrar, K. Worden, and J. Figueiras. Machine learning algorithms to damage detection under operational and environmental variability. *Health Monitoring of Structural and Biological Systems 2010*, 7650(Di):76502E, 2010.

[48] D. Frangopol and S. Kim. *Bridge Safety, Maintenance and Management in a Life-Cycle Context*. CRC Press, 2021.

[49] M. Frank, D. Drikakis, and V. Charissis. Machine-learning methods for computational science and engineering. *Computation*, 8(1):1–35, 2020.

[50] M. I. Friswell. Damage identification using inverse methods. *Philosophical Transactions of the Royal Society A: Mathematical, Physical and Engineering Sciences*, 365(1851):393–410, 2007.

[51] M. I. Friswell and J. E. Mottershead. *Finite Element Model Updating in Structural Dynamics*, volume 38 of *Solid Mechanics and its Applications*. Springer Netherlands, Dordrecht, 1995.

[52] C.-P. Fritzen. Vibration-based structural health monitoring – concepts and applications. *Key Engineering Materials - KEY ENG MAT*, 293, 09 2005.

[53] D. Garcia-Sanchez, A. Fernandez-Navamuel, D. Z. Sánchez, D. Alvear, and D. Pardo. Bearing assessment tool for longitudinal bridge performance. *Journal of Civil Structural Health Monitoring*, pages 1–25, 2020.

[54] E. García-Macías and F. Ubertini. Mova/moss: Two integrated software solutions for comprehensive structural health monitoring of structures. *Mechanical Systems and Signal Processing*, 143:106830, 2020.

[55] L. Garibaldi, S. Marchesiello, and E. Bonisoli. Identification and updating over the z24 benchmark. *Mechanical Systems and Signal Processing*, 17(1):153–161, 2003.

[56] K. Ghoulem, T. Kormi, and N. B. H. Ali. Damage detection in nonlinear civil structures using kernel principal component analysis. *Advances in Structural Engineering*, 23(11):2414–2430, 2020.

[57] D. Giagopoulos, A. Arailopoulos, V. Dertimanis, C. Papadimitriou, E. Chatzi, and K. Grompanopoulos. Structural health monitoring and fatigue damage estimation using vibration measurements and finite element model updating. *Structural Health Monitoring*, 18(4):1189–1206, 2019.

[58] P. F. Giordano, M. P. Limongelli, and L. Prendergast. Impact of climate change on the value of information for bridges at risk of scour. 10 2020.

[59] I. Goodfellow, Y. Bengio, and A. Courville. *Deep Learning.* The MIT Press, 2016.

[60] M. Gordan, H. A. Razak, Z. Ismail, and K. Ghaedi. Recent developments in damage identification of structures using data mining. *Latin American Journal of Solids and Structures*, 14(13):2373–2401, 2017.

[61] H. Guan and V. M. Karbhari. Vibration-Based Structural Health Monitoring of Highway Bridges. Technical Report December, Department of Structural Engineering, University of California, San Diego, 2008.

[62] A. Guili, A. Kapoor, and S. Pal. *Deep Learning with TensorFlow 2 and Keras: Regression, ConvNets, GANs, RNNs, NLP, and More with TensorFlow 2 and the Keras API.* 2019.

[63] M. Gul and F. Necati Catbas. Statistical pattern recognition for Structural Health Monitoring using time series modeling: Theory and experimental verifications. *Mechanical Systems and Signal Processing*, 23(7):2192–2204, 2009.

[64] E. Haber and L. Ruthotto. Stable architectures for deep neural networks. *Inverse Problems*, 34(1), 2018.

[65] J. He and Z.-F. Fu. *Modal Analysis.* 2001.

[66] K. He, X. Zhang, S. Ren, and J. Sun. Identity mappings in deep residual networks. In *Lecture Notes in Computer Science (including subseries Lecture Notes in Artificial Intelligence and Lecture Notes in Bioinformatics)*, volume 9908 LNCS, pages 630–645, 2016.

[67] M. He, P. Liang, J. Li, Y. Zhang, and Y. Liu. Fully automated precise operational modal identification. *Engineering Structures*, 234, may 2021.

[68] G. E. Hinton and R. R. Salakhutdinov. Reducing the dimensionality of data with neural networks. *Science*, 313:504 – 507, 2006.

[69] H. Hoffmann. Kernel PCA for novelty detection. *Pattern Recognition*, 40(3):863–874, 2007.

[70] K. Hornik. Approximation capabilities of multilayer feedforward networks. *Neural Networks*, 4(2):251–257, 1991.

[71] F. Huseynov, C. Kim, E. J. OBrien, J. M. Brownjohn, D. Hester, and K. C. Chang. Bridge damage detection using rotation measurements – Experimental validation. *Mechanical Systems and Signal Processing*, 135:106380, 2020.

[72] I. Jolliffe. *Principal Component Analysis*, pages 1094–1096. Springer Berlin Heidelberg, Berlin, Heidelberg, 2011.

[73] N. L. Khoa, B. Zhang, Y. Wang, F. Chen, and S. Mustapha. Robust dimensionality reduction and damage detection approaches in structural health monitoring. *Structural Health Monitoring*, 13(4):406–417, 2014.

[74] D. P. Kingma and J. L. Ba. Adam: A method for stochastic optimization. *3rd International Conference on Learning Representations, ICLR 2015 - Conference Track Proceedings*, pages 1–15, 2015.

[75] P. Kot, M. Muradov, M. Gkantou, G. S. Kamaris, K. Hashim, and D. Yeboah. Recent advancements in non-destructive testing techniques for structural health monitoring. *Applied Sciences (Switzerland)*, 11(6), 2021.

[76] J. Kullaa. Damage detection of the Z24 bridge using control charts. *Mechanical Systems and Signal Processing*, 17(1):163–170, 2003.

[77] R. Langone, E. Reynders, S. Mehrkanoon, and J. A. Suykens. Automated structural health monitoring based on adaptive kernel spectral clustering. *Mechanical Systems and Signal Processing*, 90:64–78, 2017.

[78] R. I. Levin and N. A. Lieven. Dynamic finite element model updating using simulated annealing and genetic algorithms. *Mechanical Systems and Signal Processing*, 12(1):91–120, 1998.

[79] L. Li, Y. Fang, J. Wu, and J. Wang. Autoencoder based residual deep networks for robust regression prediction and spatiotemporal estimation. *CoRR*, 2018.

[80] M. P. Limongelli, E. Chatzi, M. Döhler, G. Lombaert, and E. Reynders. Towards extraction of vibration-based damage indicators. *8th European Workshop on Structural Health Monitoring, EWSHM 2016*, 1:546–555, 2016.

[81] M. P. Limongelli and P. F. Giordano. Vibration-based damage indicators: a comparison based on information entropy. *Journal of Civil Structural Health Monitoring*, 10, 04 2020.

[82] T. Liu, Q. Zhang, T. Zordan, and B. Briseghella. Finite Element Model Updating of Canonica Bridge Using Experimental Modal Data and Genetic Algorithm. *Structural Engineering International*, 26(1):27–36, 2016.

[83] M. Lollesgaard and R. Brøndum. Great belt bridge – structural monitoring. pages 401–408, 01 2018.

[84] F. Magalhães. *Operational Modal Analysis for Testing and Monitoring of Bridges and Special Structures.* PhD thesis, 2010.

[85] F. Magalhães and Á. Cunha. Explaining operational modal analysis with data from an arch bridge. *Mechanical Systems and Signal Processing*, 25(5):1431–1450, 2011.

[86] F. Magalhães, Á. Cunha, and E. Caetano. Dynamic monitoring of a long span arch bridge. *Engineering Structures*, 30(11):3034–3044, 2008.

[87] F. Magalhães, A. Cunha, and E. Caetano. Vibration based structural health monitoring of an arch bridge: From automated OMA to damage detection. *Mechanical Systems and Signal Processing*, 28:212–228, 2012.

[88] F. Magalhães and Álvaro Cunha. Explaining operational modal analysis with data from an arch bridge. *Mechanical Systems and Signal Processing*, 25(5):1431–1450, 2011.

[89] T. Marwala. *Finite Element Model Updating Using Computational Intelligence Techniques: Applications to Structural Dynamics.* Springer, 01 2010.

[90] M. Mehrjoo, N. Khaji, H. Moharrami, and A. Bahreininejad. Damage detection of truss bridge joints using Artificial Neural Networks. *Expert Systems with Applications*, 35(3):1122–1131, 2008.

[91] A. Mosavi, H. Sedarat, S. M. O'connor, A. Emami-Naeini, and J. P. Lynch. Calibrating a high-fidelity finite element model of a highway bridge using a multi-variable sensitivity-based optimisation approach. *Structure and Infrastructure Engineering*, 10:627 – 642, 2014.

[92] J. J. Moughty and J. R. Casas. A state of the art review of modal-based damage detection in bridges: Development, challenges, and solutions. *Applied Sciences (Switzerland)*, 7(5), 2017.

[93] Z. Mousavi, M. M. Ettefagh, M. H. Sadeghi, and S. N. Razavi. Developing deep neural network for damage detection of beam-like structures using dynamic response based on fe model and real healthy state. *Applied Acoustics*, 168:107402, 2020.

[94] L. Mujica, J. Rodellar, A. Guemes, and J. López-Diez. Pca based measures: Q-statistic and t2-statistic for assessing damages in structures. *Proceedings of the 4th European Workshop on Structural Health Monitoring*, pages 1088–1095, 2008.

[95] V. H. Nguyen, J. Mahowald, J. C. Golinval, and S. Maas. Damage detection in civil engineering structure considering temperature effect. *Conference Proceedings of the Society for Experimental Mechanics Series*, 4:187–196, 2014.

[96] F. Ni, J. Zhang, and M. Noori. Deep learning for data anomaly detection and data compression of a long-span suspension bridge. *Computer-Aided Civil and Infrastructure Engineering*, 35, 12 2019.

[97] D. Y. Oh and I. D. Yun. Residual error based anomaly detection using auto-encoder in SMD machine sound. *Sensors (Switzerland)*, 18(5):1–14, 2018.

[98] M. Pastor, M. Binda, and T. Harčarik. Modal assurance criterion. *Procedia Engineering*, 48:543–548, 2012.

[99] E. Patel and D. S. Kushwaha. Clustering cloud workloads: K-means vs gaussian mixture model. *Procedia Computer Science*, 171:158–167, 2020. Third International Conference on Computing and Network Communications (CoCoNet'19).

[100] C. S. N. Pathirage, J. Li, L. Li, H. Hao, W. Liu, and P. Ni. Structural damage identification based on autoencoder neural networks and deep learning. *Engineering Structures*, 172(January):13–28, 2018.

[101] B. Peeters and G. De Roeck. One-year monitoring of the z24-bridge: Environmental effects versus damage events. *Earthquake Engineering and Structural Dynamics*, 30(2):149–171, 2001.

[102] B. Peeters, J. Maeck, and G. De Roeck. Vibration-based damage detection in civil engineering: Excitation sources and temperature effects. *Smart Materials and Structures*, 10:518, 06 2001.

[103] D. Pines and A. Aktan. Status of structural health monitoring of long-span bridges in the united states. *Progress in Structural Engineering and Materials*, 4:372 – 380, 10 2002.

[104] F. Pozo, I. Arruga, L. E. Mujica, M. Ruiz, and E. Podivilova. Detection of structural changes through principal component analysis and multivariate statistical inference. *Structural Health Monitoring*, 15(2):127–142, 2016.

[105] C. Rainieri and G. Fabbrocino. *Operational Modal Analysis of Civil Engineering Structures, An introduction and a guide for applications.* 06 2014.

[106] C. Rainieri, D. Gargaro, G. Fabbrocino, G. Maddaloni, L. Di Sarno, A. Prota, and G. Manfredi. Shaking table tests for the experimental verification of the effectiveness of an automated modal parameter monitoring system for existing bridges in seismic areas. *Structural Control and Health Monitoring*, 25(7):e2165, 2018.

[107] C. Rainieri and F. Magalhaes. Challenging aspects in removing the influence of environmental factors on modal parameter estimates. *Procedia Engineering*, 199:2244 – 2249, 2017. X International Conference on Structural Dynamics, EURODYN 2017.

[108] E. Reynders, J. Houbrechts, and G. De Roeck. Fully automated (operational) modal analysis. *Mechanical Systems and Signal Processing*, 29:228–250, 2012.

[109] E. Reynders, M. Schevenels, and G. De roeck. Macec 3.3. Technical Report July, KLEUVEN, 2014.

[110] E. Reynders, A. Teughels, and G. D. Roeck. Finite element model updating and structural damage identification using OMAX data. *Mechanical Systems & Signal Processing*, 24(5):1306–1323, 2010.

[111] E. Reynders, G. Wursten, and G. de Roeck. Output-only structural health monitoring in changing environmental conditions by means of nonlinear system identification. *Structural Health Monitoring*, 13(1):82–93, 2014.

[112] D. Ribeiro, R. Calçada, R. Delgado, M. Brehm, and V. Zabel. Finite element model updating of a bowstring-arch railway bridge based on experimental modal parameters. *Engineering Structures*, 40:413–435, 2012.

[113] K. Roy and S. Ray-Chaudhuri. Fundamental mode shape and its derivatives in structural damage localization. *Journal of Sound and Vibration*, 332(21):5584–5593, 2013.

[114] A. Rytter. *Vibrational Based Inspection of Civil Engineering Structures.* PhD thesis, University of Aalborg, Denmark, 1993. Ph.D.-Thesis defended publicly at the University of Aalborg, April 20, 1993 PDF for print: 206 pp.

[115] M. Sakurada and T. Yairi. Anomaly detection using autoencoders with nonlinear dimensionality reduction. *ACM International Conference Proceeding Series*, 02-Decembe:4–11, 2014.

[116] H. Salehi and R. Burgueño. Emerging artificial intelligence methods in structural engineering. *Engineering Structures*, 171(April):170–189, 2018.

[117] M. Sanayei, A. Khaloo, M. Gul, and F. Necati Catbas. Automated finite element model updating of a scale bridge model using measured static and modal test data. *Engineering Structures*, 102:66–79, 2015.

[118] J. Santos, C. Crémona, and P. Silveira. Automatic operational modal analysis of complex civil infrastructures. *Structural Engineering International*, 30(3):365–380, 2020.

[119] J. P. Santos, A. D. Orcesi, C. Crémona, and P. Silveira. Baseline-free real-time assessment of structural changes. *Structure and Infrastructure Engineering*, 11(2):145–161, 2015.

[120] P. Seventekidis and D. Giagopoulos. A combined finite element and hierarchical deep learning approach for structural health monitoring: Test on a pin-joint composite truss structure. *Mechanical Systems and Signal Processing*, 157:107735, 2021.

[121] P. Seventekidis, D. Giagopoulos, A. Arailopoulos, and O. Markogiannaki. Damage identification of structures through machine learning techniques with updated finite element models and experimental validations. In

Model Validation and Uncertainty Quantification, Volume 3, pages 143–154, Cham, 2020. Springer International Publishing.

[122] P. Seventekidis, D. Giagopoulos, A. Arailopoulos, and O. Markogiannaki. Structural health monitoring using deep learning with optimal finite element model generated data. *Mechanical Systems and Signal Processing*, 145:106972, 2020.

[123] M. Shahriari, D. Pardo, J. A. Rivera, C. Torres-Verdín, A. Picon, J. Del Ser, S. Ossandón, and V. M. Calo. Error control and loss functions for the deep learning inversion of borehole resistivity measurements. *International Journal for Numerical Methods in Engineering*, 122(6):1629–1657, 2021.

[124] Z. Shang, L. Sun, Y. Xia, and W. Zhang. Vibration-based damage detection for bridges by deep convolutional denoising autoencoder. *Structural Health Monitoring*, 20:1880–1903, 2021.

[125] Y. Shokrani, V. K. Dertimanis, E. N. Chatzi, and M. N. Savoia. On the use of mode shape curvatures for damage localization under varying environmental conditions. *Structural Control and Health Monitoring*, 25(4), 2018.

[126] E. Simoen, G. De Roeck, and G. Lombaert. Dealing with uncertainty in model updating for damage assessment: A review. *Mechanical Systems and Signal Processing*, 56:123–149, 2015.

[127] K. Smarsly, K. Dragos, and J. Wiggenbrock. Machine learning techniques for structural health monitoring. *8th European Workshop on Structural Health Monitoring, EWSHM 2016*, 2:1522–1531, 2016.

[128] H. Sohn. Effects of environmental and operational variability on structural health monitoring. *Philosophical Transactions of the Royal Society A: Mathematical, Physical and Engineering Sciences*, 365(1851):539–560, feb 2007.

[129] W. Soo Lon Wah, Y.-T. Chen, A. Elamin, and G. Roberts. Damage detection under temperature conditions using pca – an application to the z24 bridge. *Proceedings of the Institution of Civil Engineers - Structures and Buildings*, pages 1–13, 07 2020.

[130] V. Steffen and D. A. Rade. *Model-Based Inverse Problems in Structural Dynamics*. Wiley, 2005.

[131] L. Sun, Z. Shang, Y. Xia, S. Bhowmick, and S. Nagarajaiah. Review of bridge structural health monitoring aided by big data and artificial intelligence: From condition assessment to damage detection. *Journal of Structural Engineering*, 146:04020073, 05 2020.

[132] S. Teng, G. Chen, Z. Liu, L. Cheng, and X. Sun. Multi-sensor and decision-level fusion-based structural damage detection using a one-dimensional convolutional neural network. *Sensors*, 21, 2021.

[133] A. Teughels and G. De Roeck. Structural damage identification of the highway bridge Z24 by FE model updating. *Journal of Sound and Vibration*, 278(3):589–610, 2004.

[134] D. A. Tibaduiza, L. E. Mujica, J. Rodellar, and A. Güemes. Structural damage detection using principal component analysis and damage indices. *Journal of Intelligent Material Systems and Structures*, 27(2):233–248, 2016.

[135] L. R. Ticona Melo, R. S. Y. R. C. Silva, T. N. Bittencourt, and L. M. Bezerra. Identification of Modal Parameters in a Scale Model for a Railway Bridge. *International Journal of Structural Stability and Dynamics*, 16(09):1550059, 2016.

[136] H. Tran-Ngoc, S. Khatir, G. De Roeck, T. Bui-Tien, L. Nguyen-Ngoc, and M. Abdel Wahab. Model Updating for Nam O Bridge Using Particle Swarm Optimization Algorithm and Genetic Algorithm. *Sensors*, 18(12):4131, 2018.

[137] R. Vidal, Y. Ma, and S. Sastry. Generalized principal component analysis (gpca). *IEEE transactions on pattern analysis and machine intelligence*, 27:1945–59, 01 2006.

[138] M. E. Wall, A. Rechtsteiner, and L. M. Rocha. Singular value decomposition and principal component analysis. In *A practical approach to microarray data analysis*, pages 91–109. Springer, 2003.

[139] C. Xiong, H. Lu, and J. Zhu. Operational modal analysis of bridge structures with data from GNSS/accelerometer measurements. *Sensors (Switzerland)*, 17(3):1–20, 2017.

[140] H. Xu, X. Su, Y. Wang, H. Cai, K. Cui, and X. Chen. Automatic bridge crack detection using a convolutional neural network. *Applied Sciences (Switzerland)*, 9(14):2867, jul 2019.

[141] A.-M. Yan, G. Kerschen, P. De Boe, and J.-C. Golinval. Structural damage diagnosis under varying environmental conditions—part i: A linear analysis. *Mechanical Systems and Signal Processing*, 19(4):847–864, 2005.

[142] H. Zhang, M. Gül, and B. Kostić. Eliminating temperature effects in damage detection for civil infrastructure using time series analysis and autoassociative neural networks. *Journal of Aerospace Engineering*, 32:04019001, 2019.

[143] L. Zhang, F. Yang, Y. Daniel Zhang, and Y. J. Zhu. Road crack detection using deep convolutional neural network. *Proceedings - International Conference on Image Processing, ICIP*, 2016-Augus(October 2017):3708–3712, 2016.

[144] Z. Zhang and C. Sun. Structural damage identification via physics-guided machine learning: a methodology integrating pattern recognition with finite element model updating. *Structural Health Monitoring*, 20(4):1675–1688, 2021.